2010

Analysis and Design of a Wideband Dual-Polarized Antenna Based on the Principle of Huygens' Source

Hyukjun Seo

ANALYSIS AND DESIGN OF A WIDEBAND DUAL-POLARIZED ANTENNA BASED ON THE PRINCIPLE OF HUYGENS' SOURCE

A Thesis
presented in partial fulfillment of requirements
for the degree of Master of Science
in the Department of Electrical Engineering
The University of Mississippi

by

HYUKJUN SEO

December 2010

ABSTRACT

Analysis and designs of wideband dual-polarized antennas for mobile wireless communication systems are presented. The concept for Huygens' sources, which are combinations of electric and magnetic dipoles, is used. As a result a wideband unidirectional antenna, which consists of a planar dipole and a slot, is selected for the antenna element. This study aims at designing a dually polarized antenna with wideband performance. The first part of the study discusses the performance of the linearly polarized antenna element at 2.5 GHz. Several design parameters associated with the antenna element are addressed. To improve the performance and increase the bandwidth, a twin-fed hook-shaped probe feeding technique is applied. Prototype antennas are fabricated and tested, and good agreement between the simulated and measured results is obtained. The second part of this study is extended to design the wideband dual-polarized patch antenna. Problems associated with the practical implementation of the dual-polarized antenna in printed form are discussed. The wideband performance of the present antenna is examined by shielding the dielectric substrate from the radiating region. The proposed antenna is fabricated and tested. In addition, a metallic side wall is adopted for suppressing the back radiation. The study for designing a possible candidate for a novel dual-polarized antenna by embedding an electromagnetic bandgap (EBG) structure is investigated. Analysis for unit-cells of mushroom-like and wideband uniplanar EBG structures is performed, and simple monopoles are used for exciting the EBG embedded antenna. The presented antennas find many possible applications in many recent wireless communication systems like 3G, 3GPP Long Term Evolution (LTE), 4G, Wi-MAX, and Wi-Bro.

DEDICATION

To my beloved parents

Mr. Jung-Hwan Seo and Mrs. Soon-Tae Park

ACKNOWLEDGMENTS

I would like to express my deepest gratitude to my advisor Dr. Ahmed A. Kishk for his continuous support, guidance and caring throughout the course of this work. I would like to thank my committee members: Dr. Allen W. Glisson and Dr. Elliott Hutchcraft for their contribution and review of this thesis. I am especially grateful to Dr. Kenny Seungwoo Ryu for all the help and support he provided and for the numerous hours of time in which he generously shared his expertise with me. I am also thankful to Dr. Shing-Lung Steven Yang for helpful discussions and suggestions and to Dr. Darko Kajfez for providing suggestions and comments. I would like to thank the Department of Electrical Engineering for the continuous support during my work and the Graduate School for the summer scholarship. I am also grateful to Mr. Martye Hickman for helping with the fabrication of prototype antennas. I thank Inter-Library Loan department staff of the J.D. Williams Library for dependably and courteously providing most of my research material. Rogers Corporation provided the fabrication materials. To my friend and colleague, Karimkashi Shaya, I owe my gratitude for his helping with my measurement, Saritha Muguti for her helpful discussion during the work. I am also grateful to Dr. Younghoon Kim and Dr. Jinki Kim, Advisors of the Korean Student Association, for their mentoring and encouragement. My brother Bongkyo Seo and sister Youngji Seo extended encouragement and support throughout my career. Finally, my parents, Junghwan Seo and Soontae Park who have provided the inspiration and motivation without which I would have never completed this work. Lastly, I owe my gratitude to my beloved Master, Pomnyun Sunim for guiding and supporting me in all my endeavors.

TABLE OF CONTENTS

LIST OF TABLES

TABLE PAGE

LIST OF FIGURES

FIGURE PAGE

CHAPTER I

INTRODUCTION

1.1 Introduction

High demand for wideband and low-profile unidirectional antennas in many recent wireless communication systems, such as the fourth generation (4G) mobile smart phone, 3GPP-Long Term Evolution (LTE), Wi-MAX and Wi-Bro, has led us to investigate the development of wideband unidirectional antennas with excellent electrical characteristics of wide impedance bandwidth, low cross-polarization, low back radiation, symmetric radiation pattern, and stable gain over the operating frequency.

Several studies on the development of wideband unidirectional antenna elements can be found in the literature [1-3]. A unidirectional antenna can be implemented by placing an electric dipole one quarter wavelength above a finite ground plane [1]. Due to the frequency dependence of the height of this antenna [1] in terms of electrical wavelength, a large variation of the antenna characteristics in terms of gain and beamwidth is observed over the operating bandwidth. Another approach to realize the unidirectional antenna is the microstrip / patch antenna. There are many studies on the design of wideband patch antennas using an L-probe feed [4-8], an aperture coupled feed [9-11], stacked patches [12-16], or a U-slot patch [17-22], etc., that have been reported in the past few decades. These designs can achieve impedance bandwidths of 20% to 40%, which are sufficient for many wireless communication systems, but the radiation pattern varies substantially across the bandwidth and high cross-polarization is observed on these antennas [4-22].

Techniques for suppressing the cross-polarization, such as anti-phased cancellation [23], twin-L probes coupled feed [24], and the M-probe feed [25-29], were suggested, but these antennas still have the drawback of large variation in gain and beamwidth over the operating bandwidth as well as an asymmetric pattern in the E- and H-planes.

In order to achieve equal E- and H-plane radiation patterns and stable gain, the concept of the complementary antenna, which consists of an electric dipole and a magnetic dipole, was suggested in 1954 by Clavin [30]. With appropriate amplitude and phase for excitation of both the electric and magnetic dipoles simultaneously, equal E- and H-plane radiation patterns can be achieved. This idea was realized by Clavin again in 1974 [31]. Similar designs using a slot and dipole combination [32-35] are suggested, however, all of these designs [30-35] are either narrow bandwidth or bulky in structure. Recently, a wideband complementary antenna was proposed by Wong and Luk [36,37]. The wideband antenna element consists of a planar dipole and a shorted patch antenna. Good electrical characteristics, such as low back radiation, stable antenna gain over the operating band, and symmetric E- and H-plane radiation patterns, were achieved.

Due to the enhanced channel capacity by reducing the side effects of multipath fading, the dual polarized antenna is more desired than the linearly polarized antenna in modern wireless communication systems. Many efforts on development of the dual-polarized operation techniques using different feeding techniques have been reported in the literature [38-44]. The coaxial probe is a simple feed [23,38], but narrow bandwidth, high cross-polarization, and poor isolation are the main drawbacks of this technique. Better

isolation can be achieved by using microstrip line feed [39,40] rather than the coaxial probe; however, the bandwidth is still narrow. Low cross-polarization and high isolation can be obtained using aperture-coupled feed [41-43], but high back-lobe radiation is the main problem with this approach. Using the anti-phased cancellation technique, wide bandwidth performance with high isolation over 40dB is reported in [44].

In this thesis, a dual-polarized wideband complementary antenna is studied and proposed. The wideband complementary antenna element in [36] is adopted and extended to dual-polarized operation. A similar approach for dual-polarization is reported in [45], but the bandwidth is reduced due to the dielectric materials between two vertical shorting walls. Here, the proposed antenna with shielded dielectric substrate can effectively improve the impedance bandwidth and retain other excellent characteristics, such as low cross-polarization, low back radiation, and symmetric E- and H-plane radiation patterns, of the wideband complementary antenna element. In order to verify the performance of the proposed antenna, simulation analyses are compared with experimental measurements.

1.2 Survey of previous research

In order to understand more details of a complementary antenna, which consists of an electric dipole and a magnetic dipole, for having unidirectional symmetric radiation patterns, it is meaningful to illustrate the basic principle of the antenna briefly. Several previous researches in the literature and choosing wideband elements for the electric dipole and magnetic dipole are discussed in this section.

1.2.1 Complementary antenna consisted of an electric dipole and a magnetic dipole

The concept of a complementary antenna, which is based on Huygen's source principal, is implemented by exciting an electric dipole and a magnetic dipole simultaneously, so as to have equal E- and H-planes radiation patterns as proposed by Clavin in 1954 [30]. Fig. 1.1 shows his idea for the principle of the complementary antenna with two orthogonal sources. Using an electric dipole and the open end of a waveguide, these sources can be realized as in [30]. The two sources are located at origin in order to have a symmetric E- and H-plane radiation pattern, and the distance between the two sources can control the amplitude and phase of the sources. Field patterns of an electric dipole and a magnetic dipole are illustrated in Fig. 1.1. It is well known that the electric dipole has a figure-8 radiation pattern in the E-plane and a figure-O pattern in the H-plane, while the magnetic dipole has a figure-O pattern in the E-plane and a figure-8 pattern in the H-plane.

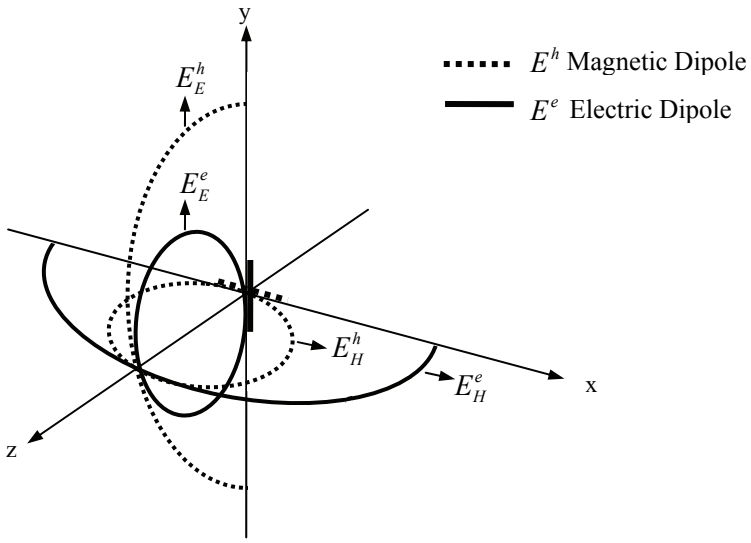

Fig. 1.1 Basic principle of a complementary antenna consisting of an electric dipole and a magnetic dipole

1.2.2 Complementary antenna consisted of slot antenna and parasitic wires

Using the principle of the Huygens' source as in [30], some studies [31-35] have been conducted to implement the complementary antenna by combining of a slot antenna and a dipole. King [32] demonstrated the modification of a slot antenna by arranging a dipole in front of the slot. Then Gabriel [34] and Wilkinson [35] used a slot-dipole antenna. Fig. 1.2 shows a complementary antenna consisting of a rectangular slot and two inverted L-wires proposed by Clavin in 1974 [31]. Such an arrangement is equivalent to implementing a magnetic dipole from the slot and an electric dipole from the inverted L-wires, and a simple structure for the complementary antenna is formed.

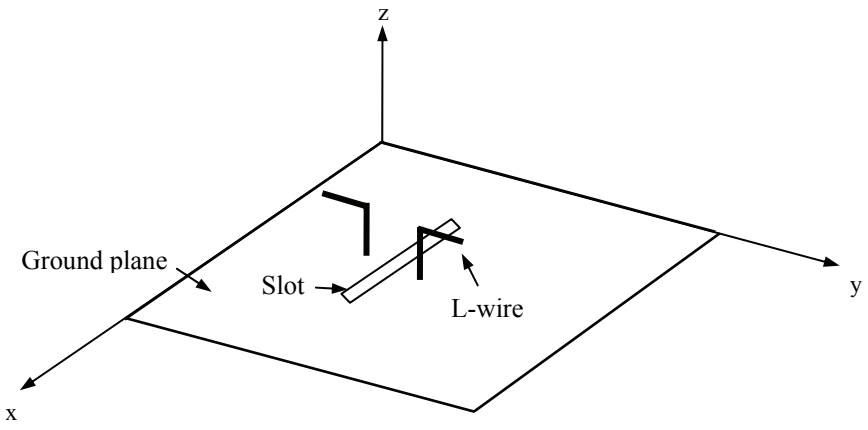

Fig. 1.2 A complementary antenna consisted of a slot and inverted L-wires

1.2.3 Wideband complementary antenna consisted of a planar dipole and a shorted patch antenna

Recently, a wideband complementary antenna was proposed by Luk and Wong [36,37] as shown in Fig. 1.3. In order to achieve wideband performance for the

complementary antenna, a planar dipole and a shorted patch antenna with an L-shaped probe feed are selected. The planar dipole and a shorted patch antenna are equivalent to an electric dipole and a magnetic dipole, respectively. This configuration can provide not only the unidirectional symmetric radiation pattern, but also wide impedance bandwidth.

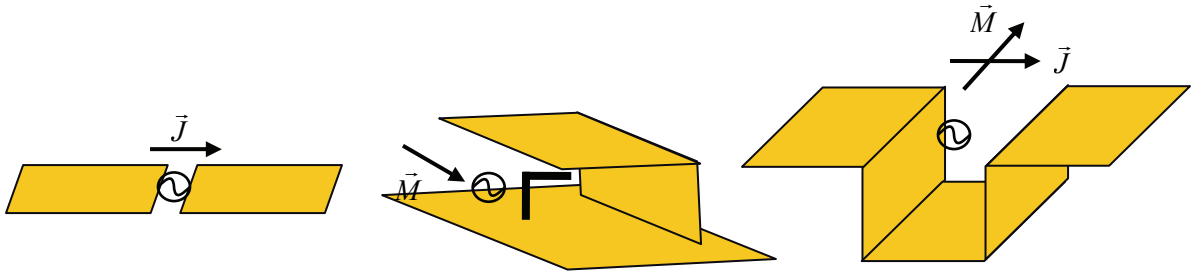

(a) Conventional half-wavelength electric dipole antenna

(b) Quarter-wave shorted patch antenna fed by L-probe

(c) Wideband complementary antenna consisting of an electric dipole and a quarter-wave patch

Fig. 1.3 A wideband complementary antenna consisted of a planar dipole and a shorted patch antenna

1.3 Organization of the thesis

Chapter I of this thesis introduces the concept of the unidirectional complementary antenna and some previous studies including the wideband unidirectional antenna. Dual polarized operation with different feeding method is reviewed briefly.

Chapter II discusses a linearly polarized wideband patch antenna with shielded dielectric loading. The effect of loading and shielding the dielectric substrate of the proposed antenna is described. Intensive parametric studies for the radiating element and hook-shaped probe feed are performed using a simulation tool. In order to enhance the

bandwidth and gain, twin hook-shaped probes are adopted, and comparison between single-feed and twin-feed is illustrated.

Chapter III presents a dual-polarized wideband patch antenna as an extension from the linearly polarized antenna in chapter II. The proposed antenna is built and tested. Results for reflection coefficients and isolation levels of the antenna are obtained using an HP-8510C Network Analyzer, while the far-field radiation patterns for both co- and cross-polarization are measured in a compact antenna test range with an HP-8530A Antenna Measurement System. Problems associated with isolation between the two input ports are discussed. The conventional back-lobe suppression technique, i.e., the addition of the side walls, is employed for the proposed antenna.

Chapter IV examines a novel dual-polarized patch antenna with embedded electromagnetic bandgap (EBG) structures. The presence of an ideal perfect magnetic conductor (PMC) wall is discussed first, and then two different EBG structures are examined for realizing the PMC wall. Dispersion diagram for a unit-cell of the EBG structure is analyzed with two different simulation setups: one for the conventional method and the other for the two-layer method under the configuration of our proposed antenna.

Finally, concluding remarks on this study are presented in Chapter V.

CHAPTER II

A LINEARLY POLARIZED WIDEBAND PATCH ANTENNA WITH SHIELDED DIELECTRIC LOADING

2.1 Introduction

A linearly polarized wideband patch antenna with shielded dielectric loading is presented in this chapter. As studied in the previous chapter, the concept of a complementary antenna, which is composed of an electric dipole and a magnetic dipole, was introduced in 1954 by Calvin [30]. It is well known that the radiation pattern for the electric dipole has a figure-8 shaped pattern in the E-plane and a figure-O shaped pattern in the H-plane; whereas the radiation pattern for the magnetic dipole has a figure-O shape in the E-plane and a figure-8 shape in the H-plane. With appropriate excitation of both the electric and magnetic dipoles, the complementary antenna can have a unidirectional radiation pattern with symmetric E- and H-planes. This concept was extended for a wideband patch antenna, which was consists of a planar dipole and a shorted patch antenna, in 2006 by Wong and Luk [36,37]. The planar dipole is adopted as an electric dipole and the wideband shorted patch antenna is chosen as an equivalent to a magnetic dipole, respectively.

In this chapter, we propose a wideband patch antenna with shielded dielectric material loading using the same approach as in [36]. In [36] they used an air microstrip transmission line, which acts as 50 ohm characteristic impedance by placing a metallic strip above the vertical plate of the shorted patch wall in the air, for exciting the antenna as

shown in Fig. 2.1(a). Instead of using the metallic strip, we employed a dielectric material, which can be fabricated with a milling machine more accurately than the metallic strip with air substrate which is difficult to make and maintain the uniform spacing between the strip and the ground plane by hand, as illustrated in Fig. 2.1(c). When the spacing between them is not uniform through the air microstrip line, mismatch from the transmission line is significant. Recently, a similarly designed antenna with dielectric loading [45] was proposed, but dielectric materials were used to fill the entire radiating slot region as shown in Fig. 2.1(b). By shielding the dielectric materials in the radiating region as proposed in our study, however, possible interaction with radiating elements from the dielectric loading can be minimized. Fig. 2.1 illustrates the basic operating mechanism of the three different configurations as mentioned above.

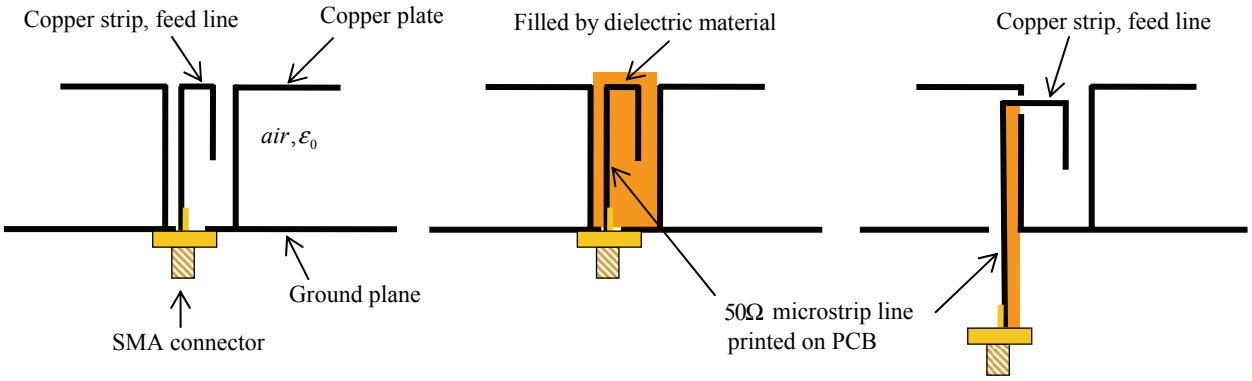

(a) w/o dielectric loading (b) w/ dielectric loading (c) w/ shielded dielectric loading

Fig. 2.1 Operation mechanism of the three different configurations

To analyze the performance of the proposed design, a parametric study was performed using the commercial software, HFSS, which is a full-wave EM simulator based

on the finite element method. The obtained results show that the proposed antenna has excellent characteristics, such as wideband response, symmetric E- and H-plane radiation patterns, and stable antenna gain over the operating bandwidth. The designed antenna was built and tested in order to verify the simulated results. It is found that the measured results are in good agreement with the simulated results.

2.2 Antenna description

The configuration of the proposed wideband patch antenna with shielded dielectric substrate operated at 2.5 GHz is shown in Fig. 2.2. The dimensions for the wideband patch antenna are adopted from the wideband unidirectional antenna element in [36]. The antenna is composed of two horizontal rectangular wings $0.25\lambda_0$ (λ_0 refers to the center frequency of the operation in air) above the finite ground plane and two vertical dielectric loaded substrates. Each rectangular wing has dimensions $W \times L = 60 \times 30\ mm^2$ ($0.5\lambda_0 \times 0.25\lambda_0$) and the ground plane is optimized to 160 mm×160 mm ($1.33\lambda_0 \times 1.33\lambda_0$). The vertical dielectric loaded substrates with dielectric constant of 2.94 and thickness of 1.524 mm are rectangular in shape, but with different size and the separation between them is S = 17 mm. On the back of the dielectric substrate, a microstrip transmission line of characteristic impedance 50 Ohms is printed to deliver the signal from the SMA connector to the antenna.

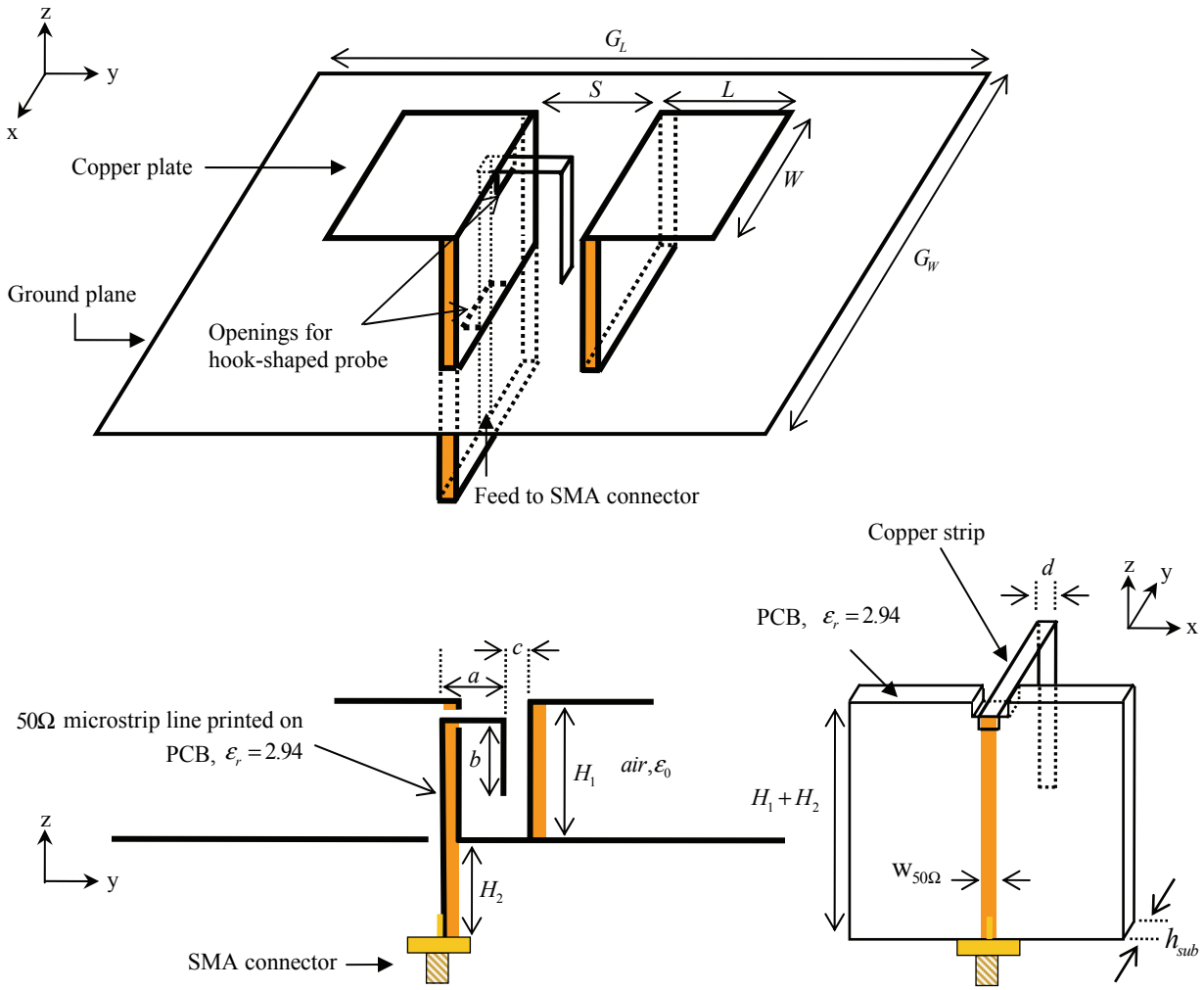

	a	b	c	d	$w_{50\Omega}$	h_{sub}	S	H_1	H_2	L	W	G_L	G_W
Value / mm	12	22	5.476	4.91	3.88	1.524	17	30	35	30	60	160	160
	0.10 λ_0	0.18 λ_0	0.05 λ_0	0.04 λ_0	0.06 λ_g	0.01 λ_0	0.14 λ_0	0.25 λ_0	0.29 λ_0	0.25 λ_0	0.50 λ_0	1.33 λ_0	1.33 λ_0

λ_g and λ_0 correspond to the center frequency of 2.5 GHz

Fig. 2.2 Configuration of a linearly polarized wideband patch antenna

To excite the proposed antenna, a hook-shaped probe feed is employed. The probe is composed of two portions, which are made by bending a rectangular copper strip into a hook shape. The first portion is horizontally oriented and is coupled with two horizontal wings that are representing an electric dipole of quarter wavelength above ground. One end of the probe is connected to a 50Ω transmission line, which is printed on the back of the vertical dielectric substrate. The length of this portion controls the input impedance of the antenna because this portion is an equivalent circuit model of an inductor. The second portion, which is vertically oriented, acts as an open circuited transmission line. This line with the vertical shorted patch introduces capacitive reactance, which can compensate the mismatch from the inductive reactance of the first portion.

2.3 Simulation design

The proposed antenna consists of a hook-shaped probe feed, a radiating element that consists of an electric dipole and a slot representing the magnetic dipole, both above a ground plane. In order to determine the effect of each part on the performance of the antenna, a parametric study has been conducted using the full-wave commercial software HFSS. A similar study had been performed for the wideband unidirectional antenna element in [36]. Using their design guideline, our proposed antenna with shielded dielectric loading has been analyzed under the assumption of zero thickness for all the metallic layers.

2.3.1 Hook-shaped probe feed

In this section, the effect of the hook-shaped probe feed is examined in terms of the

characteristic impedance of the input port by parametric study for each portion of the hook-shaped probe: *horizontal length (a)* and *vertical length (b)*. The dimension for *horizontal length (a) and vertical length (b)* as described in Fig. 2.2 is 12 mm ($0.1000\lambda_o$) and 22 mm ($0.1833\lambda_o$), respectively.

2.3.1.1 Impedance

Figs. 2.3 and 2.4 show the real and imaginary parts of the input impedance of the wideband patch antenna for different values of *a* and *b* with same *aperture width (S)*. The *horizontal length (a)* is varied from 10 mm ($0.0833\lambda_o$) to 14 mm ($0.1167\lambda_o$) with a step of 1 mm ($0.0083\lambda_o$) and a fixed value *b* of 22 mm, whereas the *vertical length (b)* is changed from 20 mm ($0.1667\lambda_o$) to 24 mm ($0.2000\lambda_o$) with a step of 1 mm ($0.0083\lambda_o$) and a fixed value *a* of 12 mm. Within the frequency range from 1.8 GHz to 2.8 GHz in Fig. 2.3, it can be observed that there are three local maxima of resistance $\mathrm{Re}(Z_{11})$ at 1.8 GHz, 2.1 GHz, and 2.6 GHz. The first maxima and the second maxima are shifted down when the value of *a* is increased, while the third one around 2.6 GHz is shifted up when the value of *a* is increased. At 2.6 GHz where all the resistances for different values of *a* are around 50Ω, the reactance $\mathrm{Im}(Z_{11})$ is increased when the value of *a* is increased.

As shown in Fig. 2.4, the overall response patterns for different values of the *vertical length (b)* are similar to that for the *horizontal length (a)* case in Fig. 2.3 as the parametric value is increased. All three local maxima are not shifted significantly with a variation of the *vertical length (b)*, but only the levels are varied. It is notable that variation of *a* gives more significant change on input impedance than that of *b* when both *a* and *b* are

varied with same step of 1 mm.

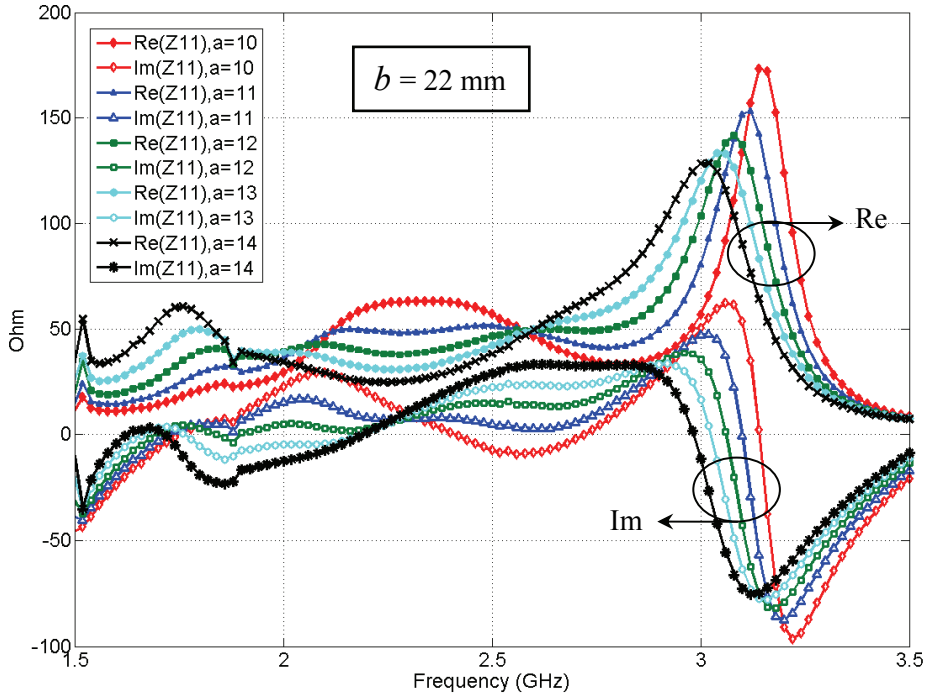

Fig. 2.3 Input impedance of the wideband patch antenna for different values of *a*

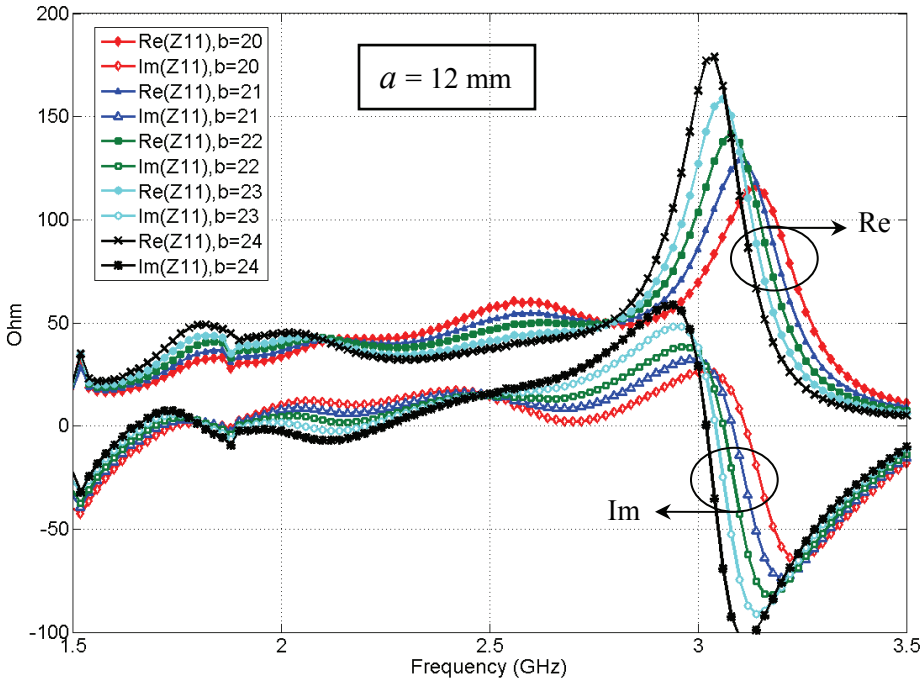

Fig. 2.4 Input impedance of the wideband patch antenna for different values of *b*

2.3.1.2 Reflection coefficient

Fig. 2.5 shows the reflection coefficient of the antenna for different values of *a*, from 10 mm ($0.0833\lambda_o$) to 14 mm ($0.1167\lambda_o$) with a step of 1 mm ($0.0083\lambda_o$) and a fixed value *b* of 22 mm ($0.1833\lambda_o$). The input impedance bandwidth is summarized in Table. 2.1. The impedance bandwidth for $S_{11} \le -10dB$ is increased when the length of *a* is increased until *a*=13mm. The maximum impedance bandwidth of 56.0% can be achieved when *a* = 13mm.

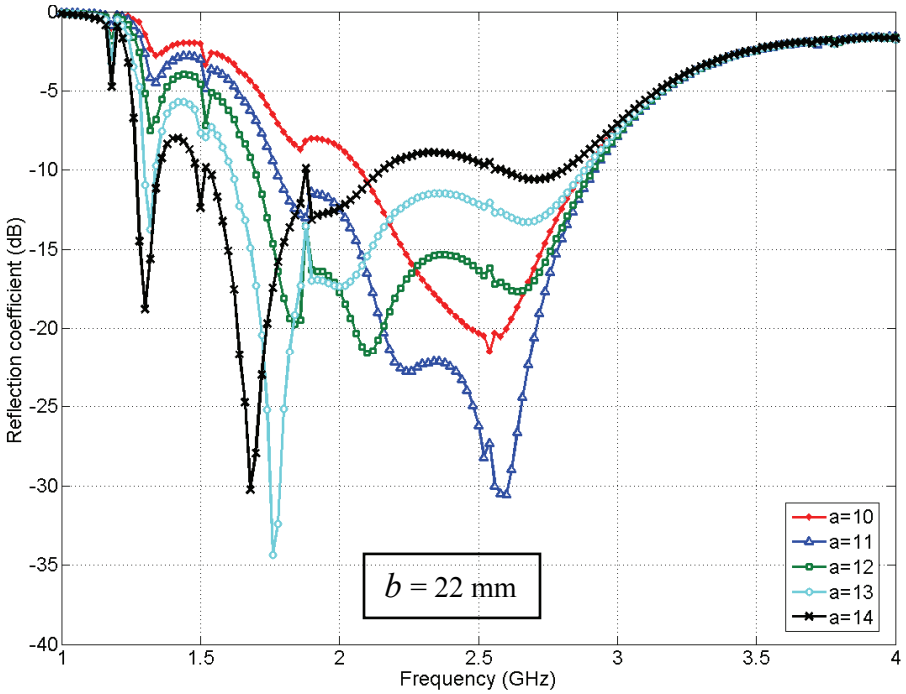

Fig. 2.5 Reflection coefficient of the wideband patch antenna for different values of *a*

Table 2.1 Impedance bandwidth for different values of *a*

a / mm	10	11	12	13	14
Range / GHz	2.08 ~ 2.88	1.78~2.92	1.70~2.90	1.62~2.88	1.54~2.14
BW ($S_{11} \le -10dB$)	32.3%	48.5%	52.2%	56.0%	32.6%

Fig. 2.6 shows the reflection coefficient of the antenna for different values of *b*, from 20 mm ($0.1667\lambda_o$) to 24 mm ($0.2000\lambda_o$) with a step of 1 mm ($0.0083\lambda_o$) and a fixed value *a* of 12 mm ($0.1000\lambda_o$). The input impedance bandwidth is tabulated in Table 2.2. The impedance bandwidth for $S_{11} \le -10dB$ only varies between 50.7% and 53.3% when the length of *b* is changed. That is due to the input impedance not being sensitive to the *vertical length (b)* as observed in Fig. 2.4. The maximum impedance bandwidth of 53.3% can be achieved when *b* = 20 mm.

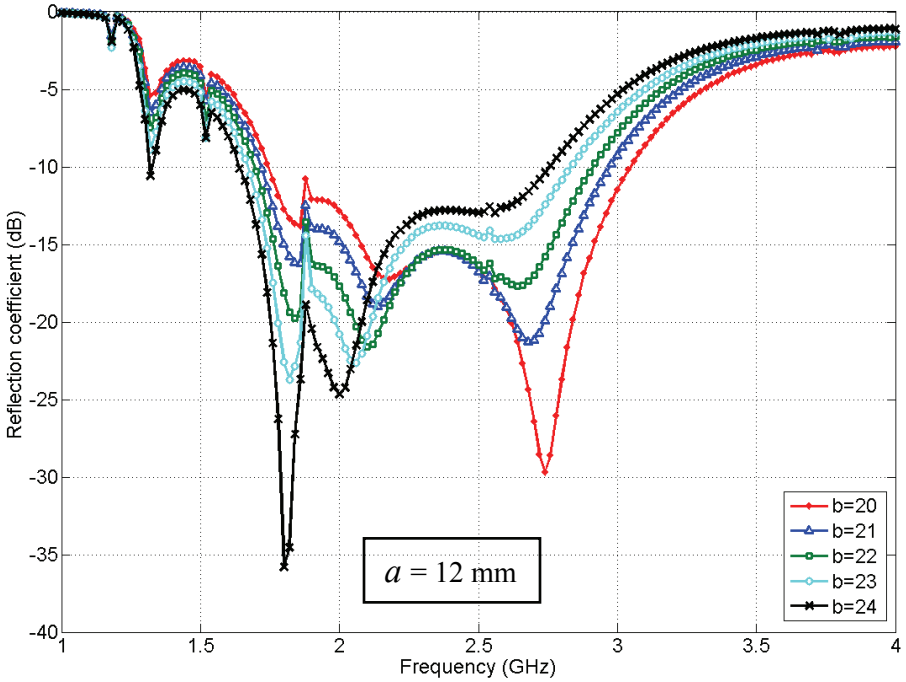

Fig. 2.6 Reflection coefficient of the wideband patch antenna for different values of *b*

Table 2.2 Impedance bandwidth for different values of *b*

b / mm	20	21	22	23	24
Range / GHz	1.76~3.04	1.72~2.96	1.70~2.90	1.68~2.82	1.64~2.76
BW ($S_{11} \le -10dB$)	53.3%	53.0%	52.2%	50.7%	50.9%

2.3.2 Radiating element

The radiating element of the antenna is a combination of the planar dipole and the half wavelength open slot quarter. The variation of the antenna characteristics, such as input impedance, reflection coefficient, gain and radiation pattern, is numerically investigated with different antenna parameters: *dipole width (W), dipole length (L), aperture width (S) and dipole height (H_1)*, whose original dimensions are W = 60 mm ($0.5000\lambda_o$), L = 30 mm ($0.2500\lambda_o$), S = 17 mm ($0.1400\lambda_o$) and H_1 = 30 mm ($0.2500\lambda_o$), respectively.

2.3.2.1 Impedance

The variation of the input impedance with different parameters of the radiating element is illustrated in Figs. 2.7 to 2.10. In Fig. 2.7, it can be found that there are two local maxima within the frequency range from 2.0 GHz to 2.7 GHz: the lower resonance at 2.0 GHz and the upper resonance at 2.6 GHz. When the *dipole width (W)* is increased, $\mathrm{Re}(Z_{11})$ and $\mathrm{Im}(Z_{11})$ is decreased at the upper resonance whereas the lower resonance is not changed much.

In Fig. 2.9, both lower and upper resonances are varied for different values of the *dipole length (L)* whereas only the upper resonance is varied with the *dipole width (W)*. The lower resonance of the resistance $\mathrm{Re}(Z_{11})$ is shifted down from 2.2 GHz to 1.8 GHz when L is increased.

The response of input impedance for different values of the *aperture width (S)* is shown in Fig. 2.9. When the value of *S* is increased, the first resonance is shifted up rapidly at 1.8 GHz, but the second resonance around 2.7 GHz is affected slowly. Because the *aperture width (S)* is associated with the hook-shaped probe, the variation of *S* affects significantly the performance of the antenna.

As observed in Fig. 2.10, the length of the *dipole height (H_1)* is varied from 26 mm ($0.2167\lambda_o$) to 34 mm ($0.2833\lambda_o$), with 2 mm ($0.0167\lambda_o$) step. The same dimension for the hook-shaped probe is used as a = 12 mm and b = 22 mm. The lower resonance peak at 1.9 GHz is decreased when the length of H_1 is increased, while the upper resonance at 2.5 GHz is shifted down as H_1 is increased.

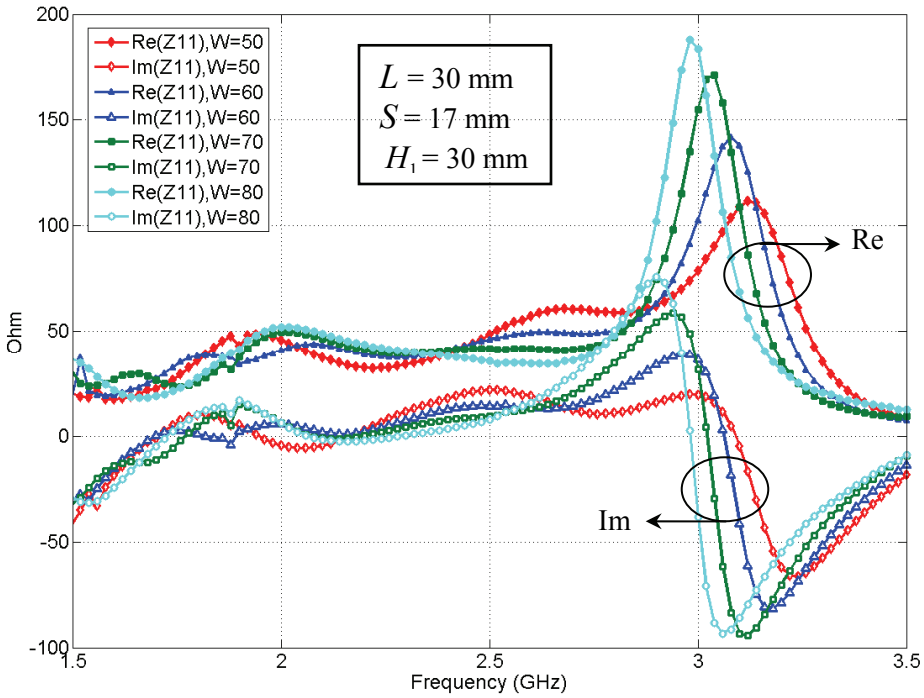

Fig. 2.7 Input impedance of the wideband patch antenna for different values of W

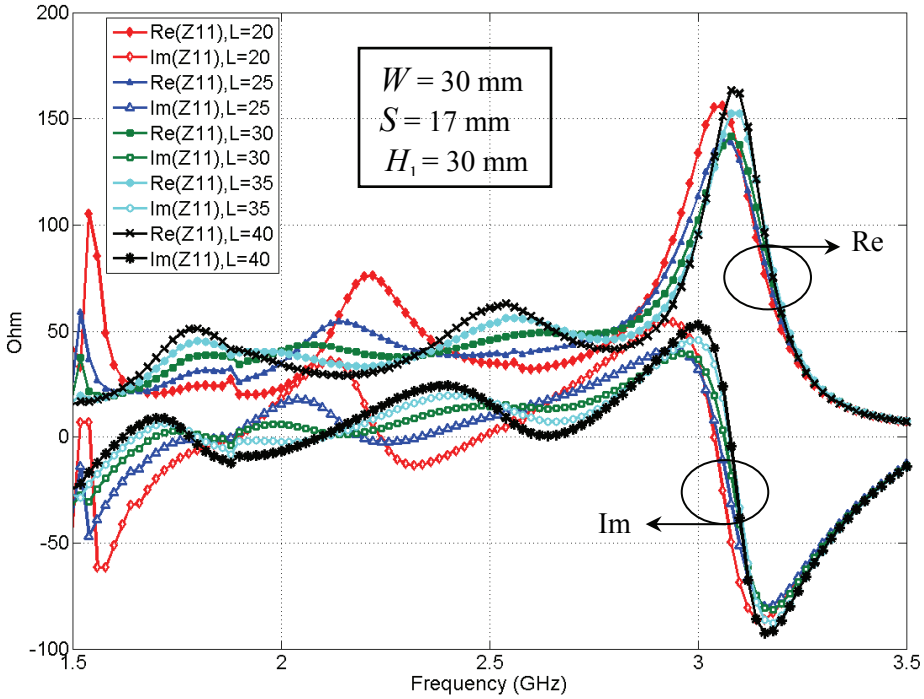

Fig. 2.8 Input impedance of the wideband patch antenna for different values of L

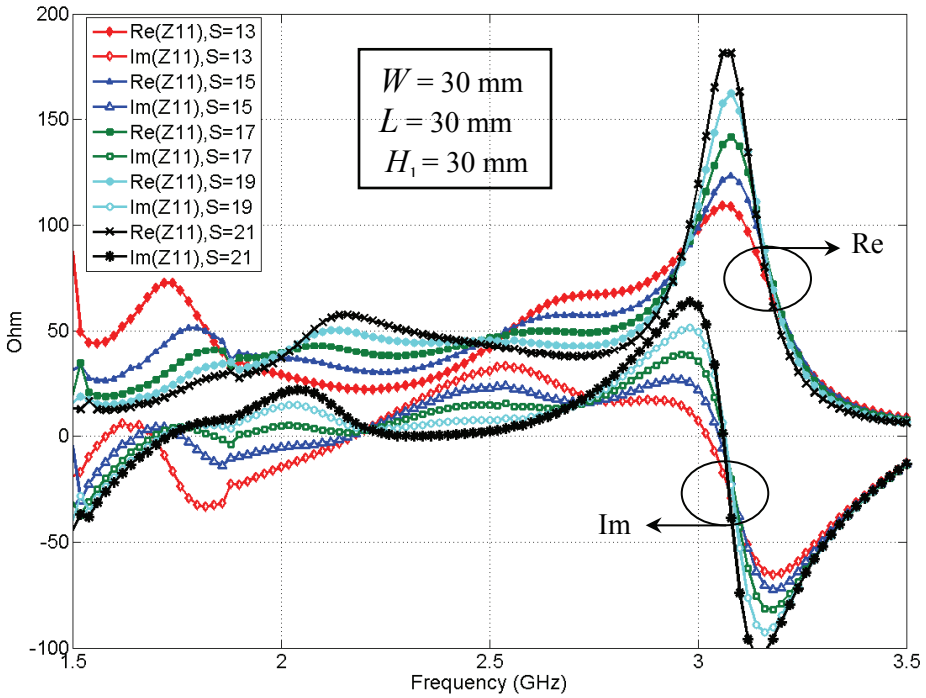

Fig. 2.9 Input impedance of the wideband patch antenna for different values of S

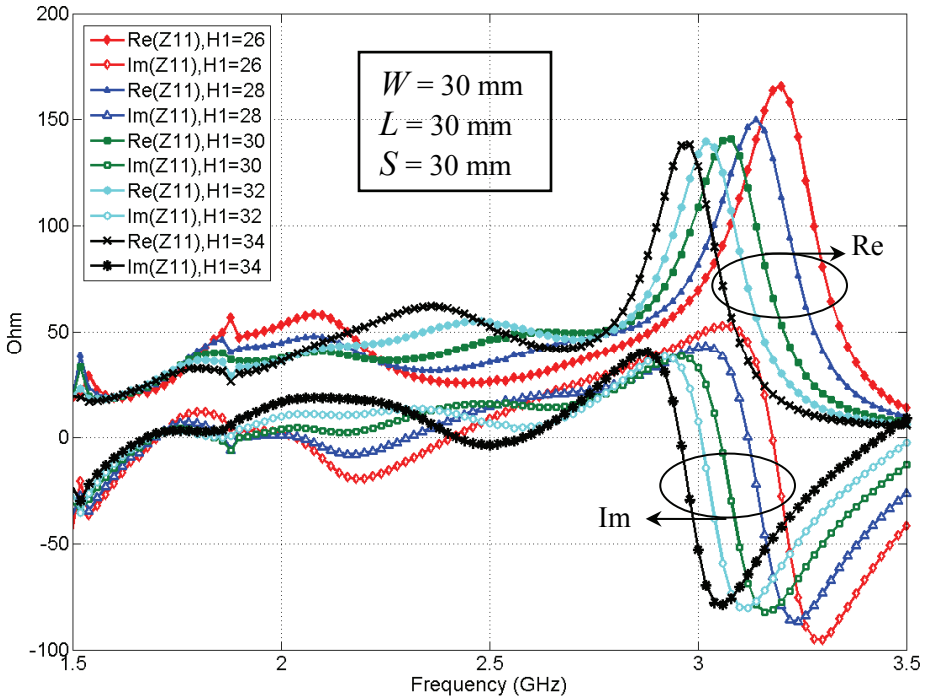

Fig. 2.10 Input impedance of the wideband patch antenna for different values of H_1

2.3.2.2 Reflection coefficient

Figs. 2.11 to 2.14 show the reflection coefficient of the antenna for different values of *W, L, S,* and H_1, respectively. As seen in Fig. 2.11, the upper cut-off frequency is shifted down when the *dipole width (W)* is increased whereas the lower one is not changed much. Hence the variation of the *dipole width (W)* can affect the upper resonance frequency. The maximum impedance bandwidth of 54.4% is achieved when *W* is 50 mm, as shown in Table. 2.3.

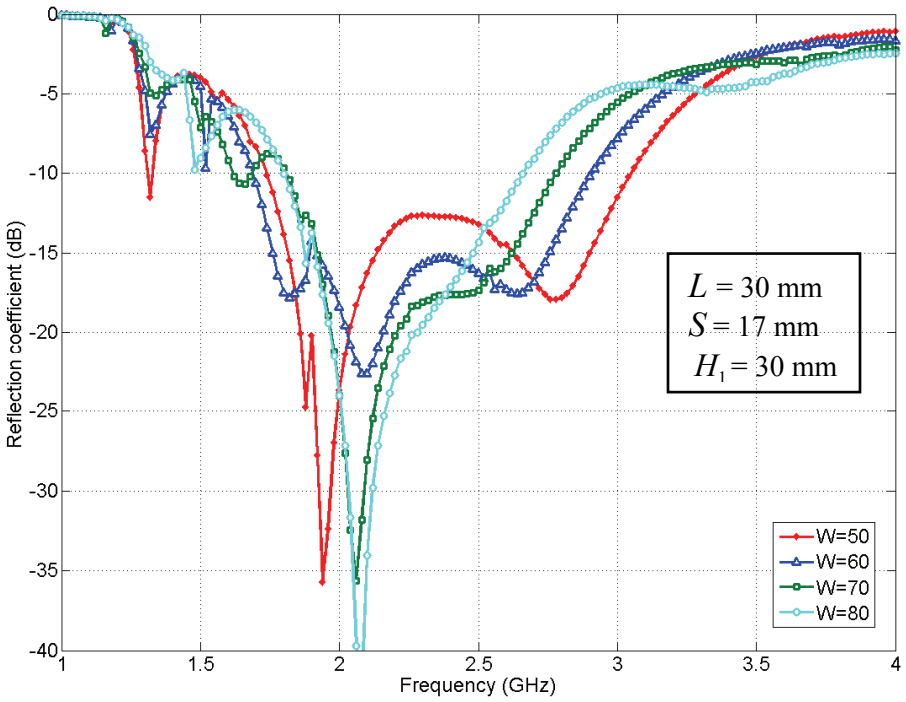

Fig. 2.11 Reflection coefficient of the wideband patch antenna for different values of *W*

Table 2.3 Impedance bandwidth for different values of *W*

W / mm	50	60	70	80
Range / GHz	1.74~3.04	1.70~2.90	1.82~2.78	1.80~2.66
BW ($S_{11} \le -10dB$)	54.4%	52.2%	41.7%	38.6%

Fig. 2.12 and Table 2.4 show the effect of the *dipole length (L)*, when L is varied from 20 mm ($0.1667\lambda_0$) to 40 mm ($0.3333\lambda_0$), with 5 mm ($0.0417\lambda_0$) step. Both lower and upper resonating frequencies are changed with the variation of the *dipole length (L)*. When L is bigger than 25 mm ($0.2083\lambda_0$), the impedance bandwidth achieved is about 50 % and it is not changed significantly with variation of L: 25 mm ($0.2083\lambda_0$) ~ 40 mm ($0.3333\lambda_0$).

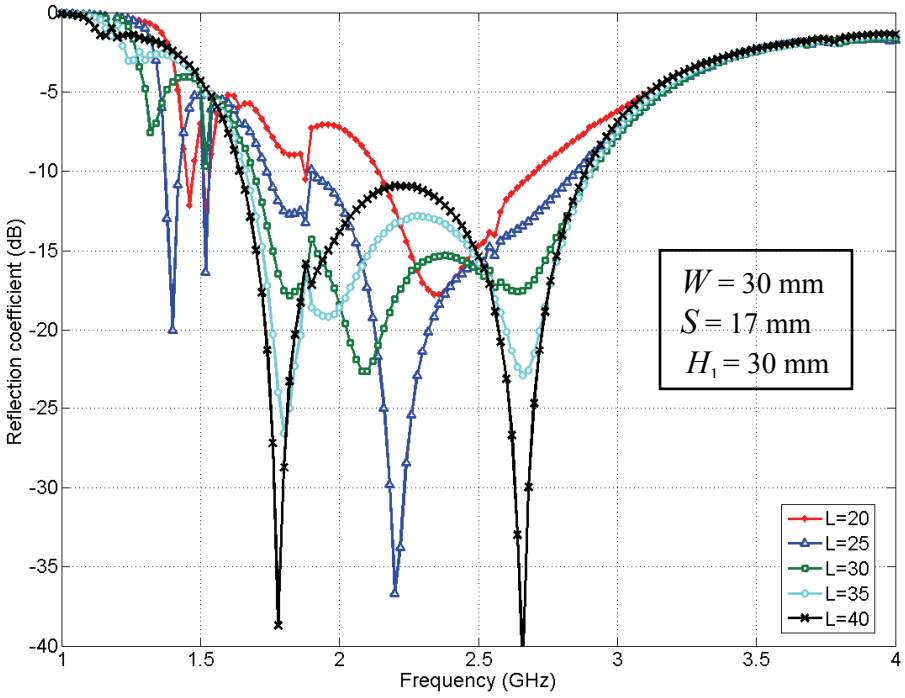

Fig. 2.12 Reflection coefficient of the wideband patch antenna for different values of L

Table 2.4 Impedance bandwidth for different values of L

L / mm	20	25	30	35	40
Range / GHz	2.14~2.70	1.74~2.84	1.70~2.90	1.66~2.90	1.64~2.88
BW ($S_{11} \le -10dB$)	23.1%	48.0%	52.2%	54.4%	54.9%

The reflection coefficient with varying the *aperture width (S)* is illustrated in Fig. 2.13 and its impedance bandwidth ($S_{11} \le -10dB$) is tabulated in Table 2.5. As observed in the response of the input impedance in Fig. 2.9, the response of the lower resonance is affected by the *aperture width (S)* significantly compared with that of the upper resonance case. When S = 15 mm, the maximum impedance bandwidth of 59.6% is achieved.

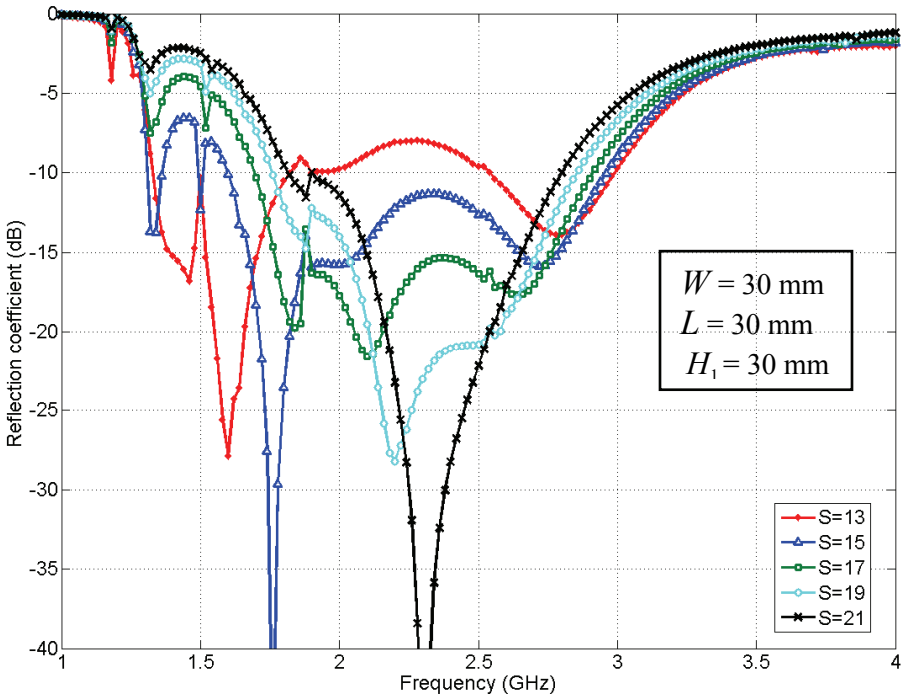

Fig. 2.13 Reflection coefficient of the wideband patch antenna for different values of S

Table 2.5 Impedance bandwidth for different values of S

S / mm	13	15	17	19	21
Range / GHz	1.34~1.82	1.6~2.96	1.70~1.90	1.76~2.84	1.82~2.80
BW ($S_{11} \le -10dB$)	30.4%	59.6%	54.1%	47.0%	42.4%

Lastly, the reflection coefficient of the antenna for different values of the *dipole height* (H_1), from 26 mm ($0.2167\lambda_0$) to 34 mm ($0.2833\lambda_0$) with 2 mm ($0.0167\lambda_0$) step, is plotted in Fig. 2.14. It seems H_1 doesn't affect the lower and upper cut-off frequencies. When H_1 = 26 mm, only one resonance at 1.96 GHz can be seen, and the impedance bandwidth is only about 31.1%. Table 2.6 summarized the input impedance with varying H_1.

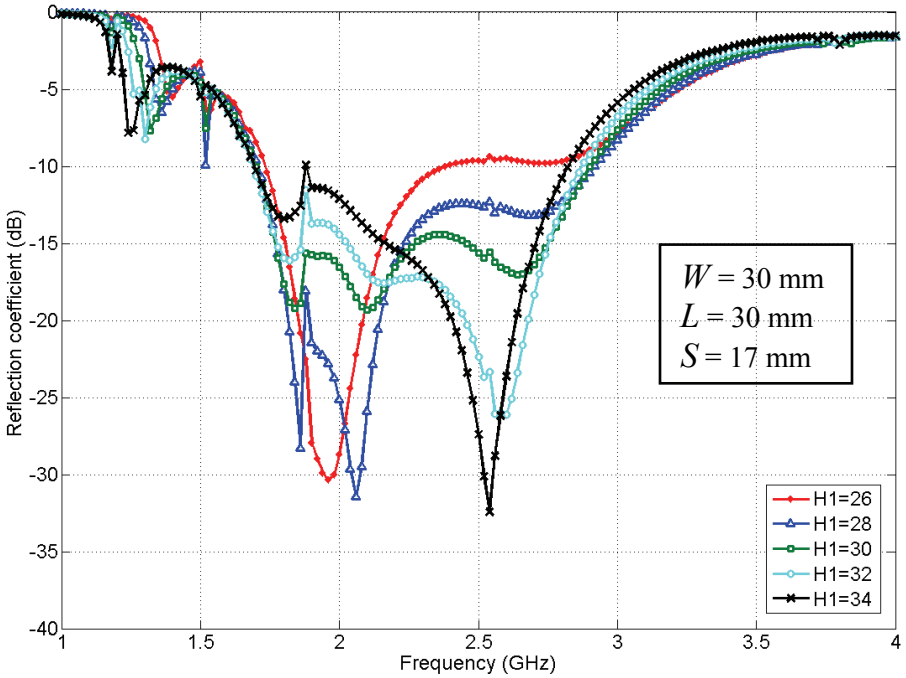

Fig. 2.14 Reflection coefficient of the wideband patch antenna for different values of H_1

Table 2.6 Impedance bandwidth for different values of H_1

H_1 / mm	26	28	30	32	34
Range / GHz	1.74~2.38	1.72~2.92	1.70~2.90	1.70~2.86	1.70~2.82
BW ($S_{11} \le -10dB$)	31.1%	51.7%	52.2%	50.9%	49.6%

2.3.2.3 Gain

In this section, the simulation study of the antenna gain for different values of the radiating element is investigated because it is desirable that the antenna has not only wide impedance bandwidth, but also stabilized high gain over the operating band. Table 2.8 shows the summary of the 2-dB gain bandwidth and maximum gain for different values of the *dipole width*, *length*, *height* and *aperture width*.

Table 2.7 Summary of simulated gain for different values of W, L, S and H_1

Dipole Width, W^*			*Dipole Length, $L^{\wedge}$*		
W (mm)	2-dB Gain BW (GHz)	Max. Gain (dBi)	L (mm)	2-dB Gain BW (GHz)	Max. Gain (dBi)
50	63.9%; 1.62~3.14	8.63	20	31.5%; 2.14~2.94	9.17
60	42.9%; 1.94~3.00	8.85	25	39.4%; 2.0~2.98	9.18
70	45.5%; 1.80~2.86	9.21	30	42.9%; 1.94~3.00	8.85
80	47.8%; 1.72~2.80	9.12	35	45.5%; 1.90~3.02	8.60
-	-	-	40	45.9%; 1.88~3.00	8.58
*Fixed L = 30mm, S = 17mm and H_1 = 30mm			^Fixed W = 60mm, S = 17mm and H_1 = 30mm		

Aperture Width, S^+			*Dipole Height, H_1^**		
S (mm)	2-dB Gain BW (GHz)	Max. Gain (dBi)	H_1 (mm)	2-dB Gain BW (GHz)	Max. Gain (dBi)
13	46.6%; 1.94~3.12	8.56	26	46.3%; 1.96~3.14	8.82
15	44.8%; 1.94~3.06	8.90	28	44.4%; 1.96~3.08	8.90
17	41.9%; 1.96~3.00	8.96	30	41.0%; 1.98~3.00	9.03
19	39.7%; 1.98~2.96	8.94	32	41.0%; 1.94~2.94	8.82
21	38.4%; 1.98~2.92	8.94	34	41.0%; 1.90~2.88	8.72
$^+$ Fixed W = 60mm, L = 30mm and H_1 = 30mm			*Fixed W = 60mm, L = 30mm and S = 17mm		

An average 2-dB gain bandwidth of 43.6% range from 1.92 GHz to 2.99 GHz is calculated from the overall simulated results in the Table 2.7. The maximum 2-dB gain bandwidth is 63.9% for the case of W = 50 mm, L = 30 mm, S = 17 mm and H_1=30 mm. When L = 20 mm, the gain deteriorates to 31.5% (2.14 GHz ~2.94 GHz). Hence, the *dipole length (L)* should not be smaller than 25 mm ($0.2083\lambda_0$) in order to have wide 2-dB gain bandwidth. The simulated maximum gain of 9.21 dBi is achieved for the case of W = 70 mm, L = 30 mm, S = 17 mm and H_1=30 mm.

The simulated gain versus frequency for different parameters is illustrated in Figs. 2.15 to 2.18. It can be observed that as the *dipole width (W)* is increased, the gain at the upper frequency deteriorates quickly, whereas when the *dipole length (L)* is increased, the gain at the lower frequency is enhanced in Figs. 2.15 and 2.16, respectively.

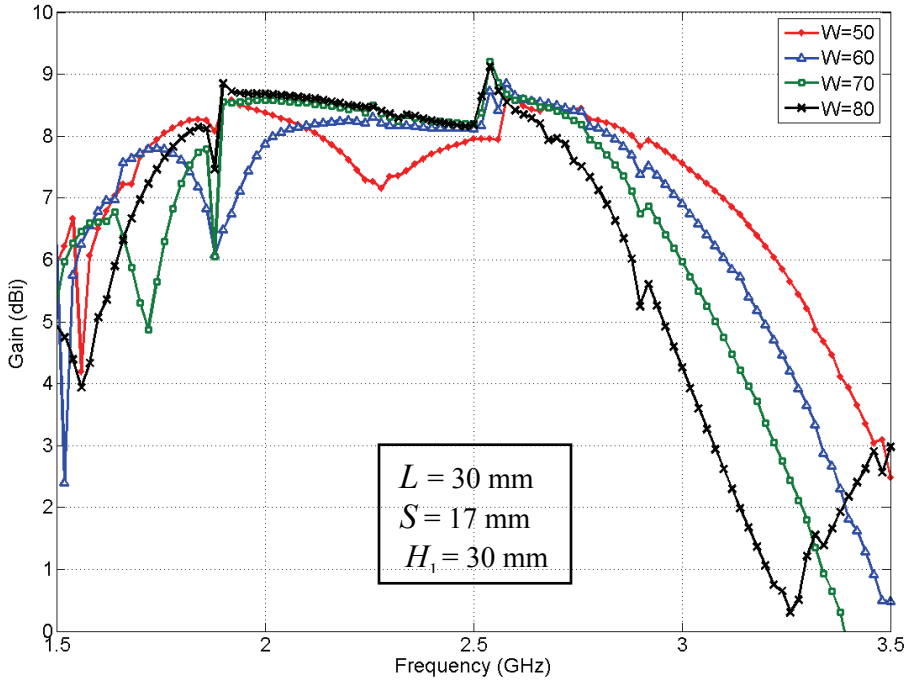

Fig. 2.15 Gain of the wideband patch antenna for different values of W

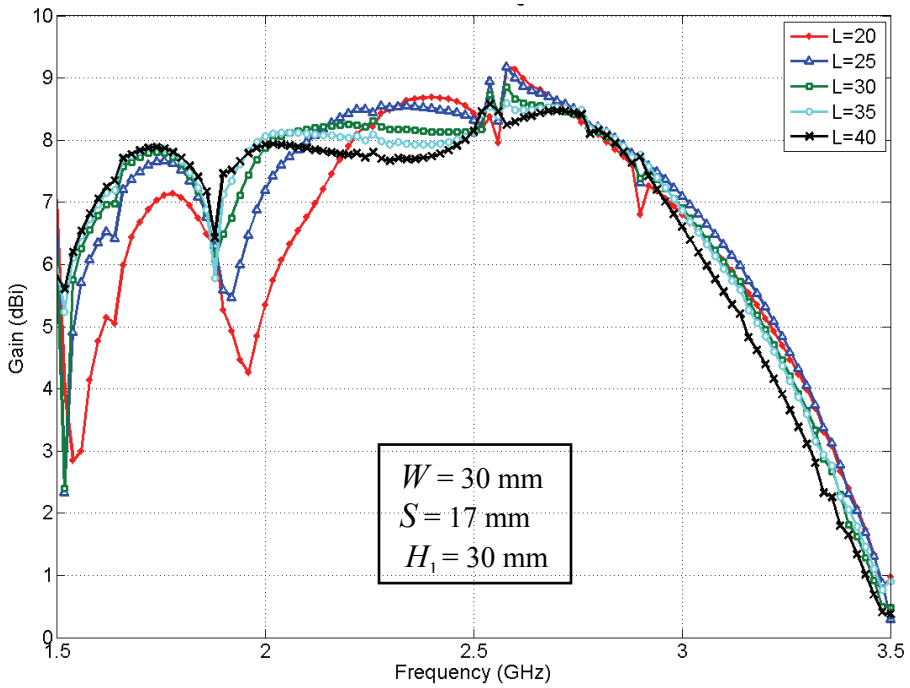

Fig. 2.16 Gain of the wideband patch antenna for different values of L

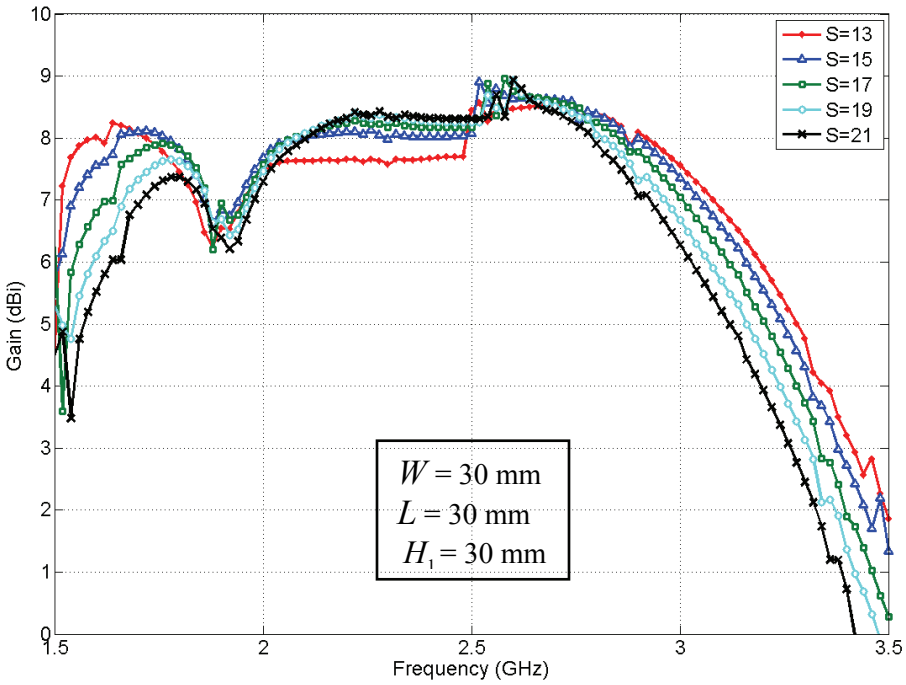

Fig. 2.17 Gain of the wideband patch antenna for different values of S

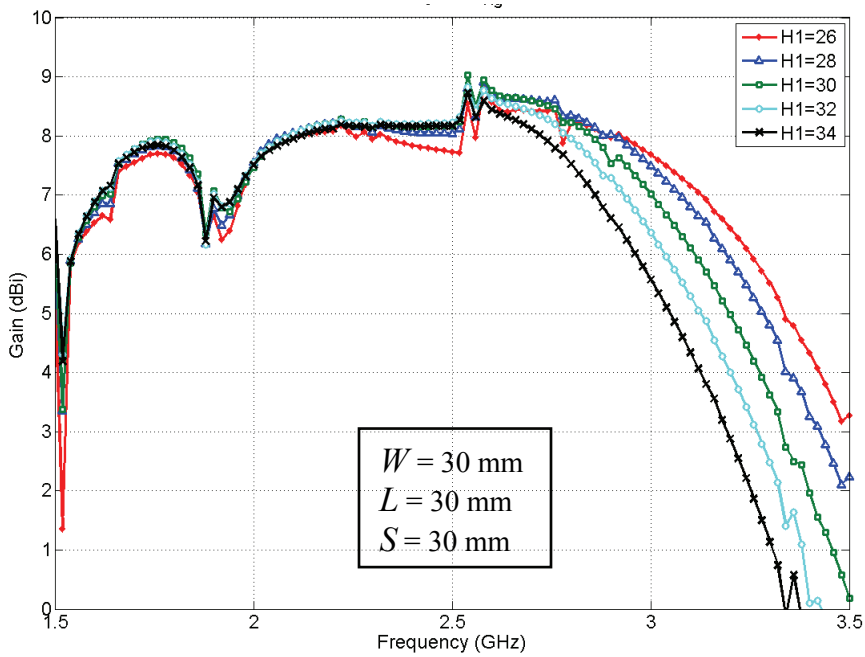

Fig. 2.18 Gain of the wideband patch antenna for different values of H_1

2.3.2.4 Radiation pattern

The variation of the radiation pattern for different values of the radiating element parameters is analyzed in this section. Figs. 2.19 to 2.22 illustrate both E-plane and H-plane radiation patterns of the antenna at the center frequency of 2.5 GHz when the values for parameters of the radiating element, *W, L, S,* and H_1, are swept, respectively. The 3dB beamwidth for each principle plane and front-to-back ratio are tabulated in Tables 2.8 to 2.11. The ground plane with size of 160 mm ($1.33\lambda_o$) × 160 mm ($1.33\lambda_o$) is used during the parametric study in this section.

In Fig. 2.19, the E-plane is not sensitive to the variation of the *dipole width (W)* within the range from 50 mm to 80 mm with 10 mm step, while the 3dB beamwidth in the H-plane is decreased from 80^o to 64^o when *W* is increased with the same step. In the case of *W* = 50 mm, the 3dB beamwidth in the H-plane is very stable up to 80^o and the front-to-back ratio is 20.67 dB. It is notable that the antenna has symmetric radiation patterns in the E-plane and H-plane.

When the *dipole length (L)* is varying, the opposite phenomenon is observed compared to the case of the *dipole width (W)*, as shown in Fig. 2.20. The H-plane does not change significantly with the sweep of *L*, from 20 mm to 40 mm, with 5 mm step. In the E-plane, however, the 3dB beamwidth is increased when *L* is increased. The 3dB beamwidth ranges from 58^o to 66^o and 72^o to 76^o in the E-plane and H-plane, respectively. The front-to-back ratio is achieved around 20 dB, but when *L* = 20 mm, the

3dB beamwidth is deteriorated by 14.80 dB.

As seen in Fig. 2.21 for the variation of the *aperture width (S)*, it can be observed that both E- and H-planes are not sensitive with different values of *S*, between 13 mm ($0.1083\lambda_o$) to 21 mm ($0.1750\lambda_o$). The 3dB beamwidth is around 64^o and 76^o in the E-plane and H-plane, respectively. The front-to-back ratio is slightly improved from 19.46 dB to 20.93 when *S* is widened.

Next, the radiation pattern of the antenna for different value of H_1 is illustrated in Fig. 2.22. Both E-plane and H-plane are stable with variation of the *dipole height* (H_1). Especially in the case of H_1 = 26 mm, the 3dB beamwidth in E- and H-planes is 72^o. The front-to-back ratio ranges from 20.58 dB to 22.34 dB.

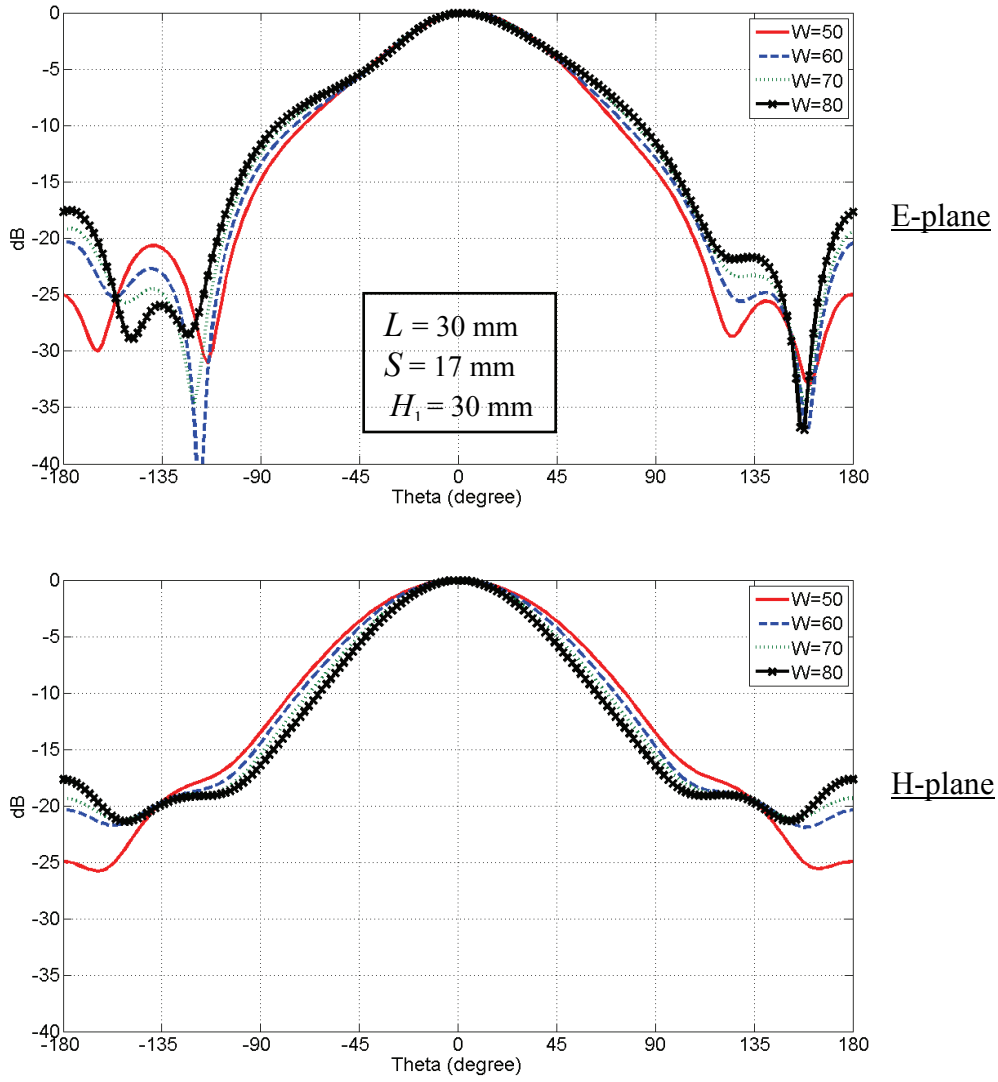

Fig. 2.19 Radiation pattern of the wideband patch antenna for different values of W

Table 2.8 3dB beamwidth and front-to-back ratio for different values of W

W (mm)	3dB Beamwidth, E-plane	3dB Beamwidth, H-plane	Front-to-back Ratio
50	66^o	80^o	20.67 dB
60	66^o	76^o	20.33dB
70	68^o	68^o	19.16dB
80	66^o	64^o	17.53dB

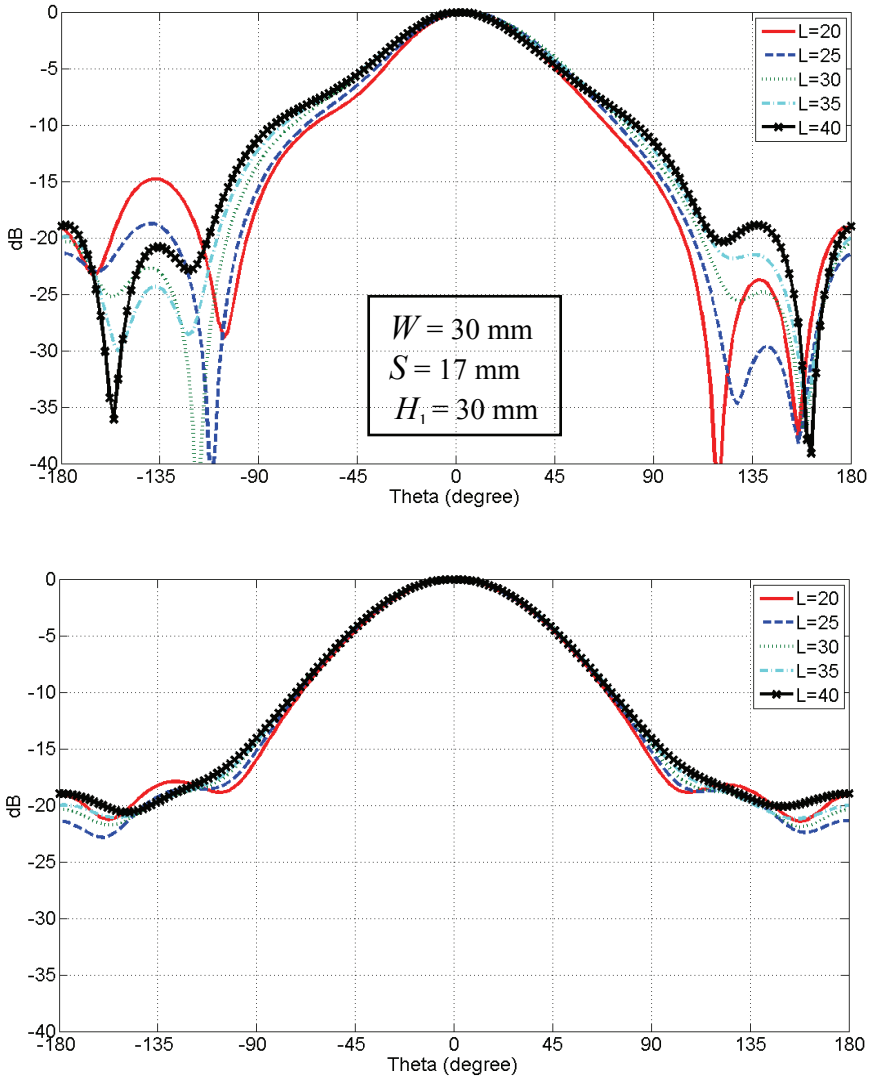

Fig. 2.20 Radiation pattern of the wideband patch antenna for different values of *L*

Table 2.9 3dB beamwidth and front-to-back ratio for different values of *L*

L (mm)	3dB Beamwidth, E-plane	3dB Beamwidth, H-plane	Front-to-back Ratio
20	58^o	72^o	14.80 dB
25	64^o	72^o	18.75 dB
30	66^o	72^o	20.33 dB
35	66^o	76^o	20.03 dB
40	64^o	76^o	18.87 dB

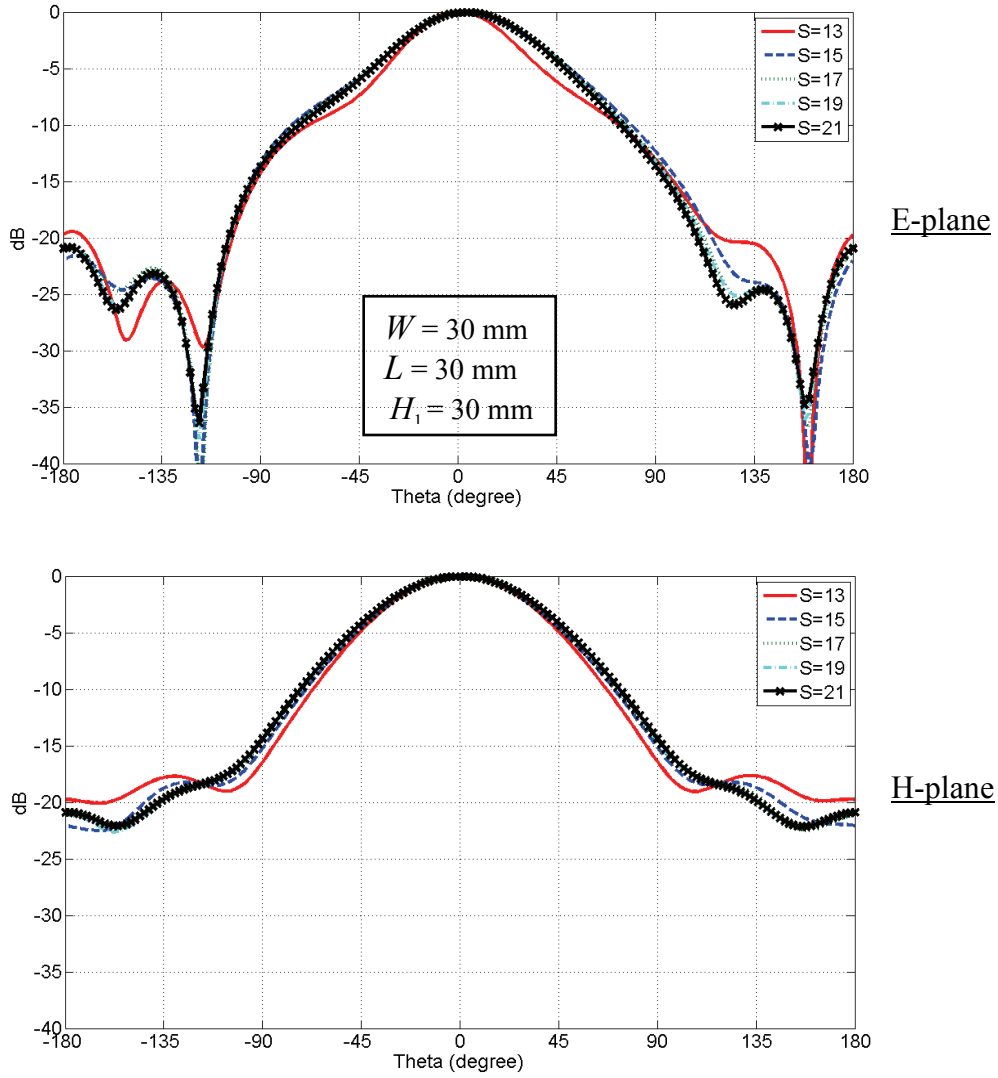

Fig. 2.21 Radiation pattern of the wideband patch antenna for different values of *S*

Table 2.10 3dB beamwidth and front-to-back ratio for different values of *S*

S (mm)	3dB Beamwidth, E-plane	3dB Beamwidth, H-plane	Front-to-back Ratio
13	60^o	68^o	19.46 dB
15	64^o	72^o	21.58 dB
17	66^o	76^o	20.96 dB
19	66^o	76^o	20.95 dB
21	64^o	76^o	20.93 dB

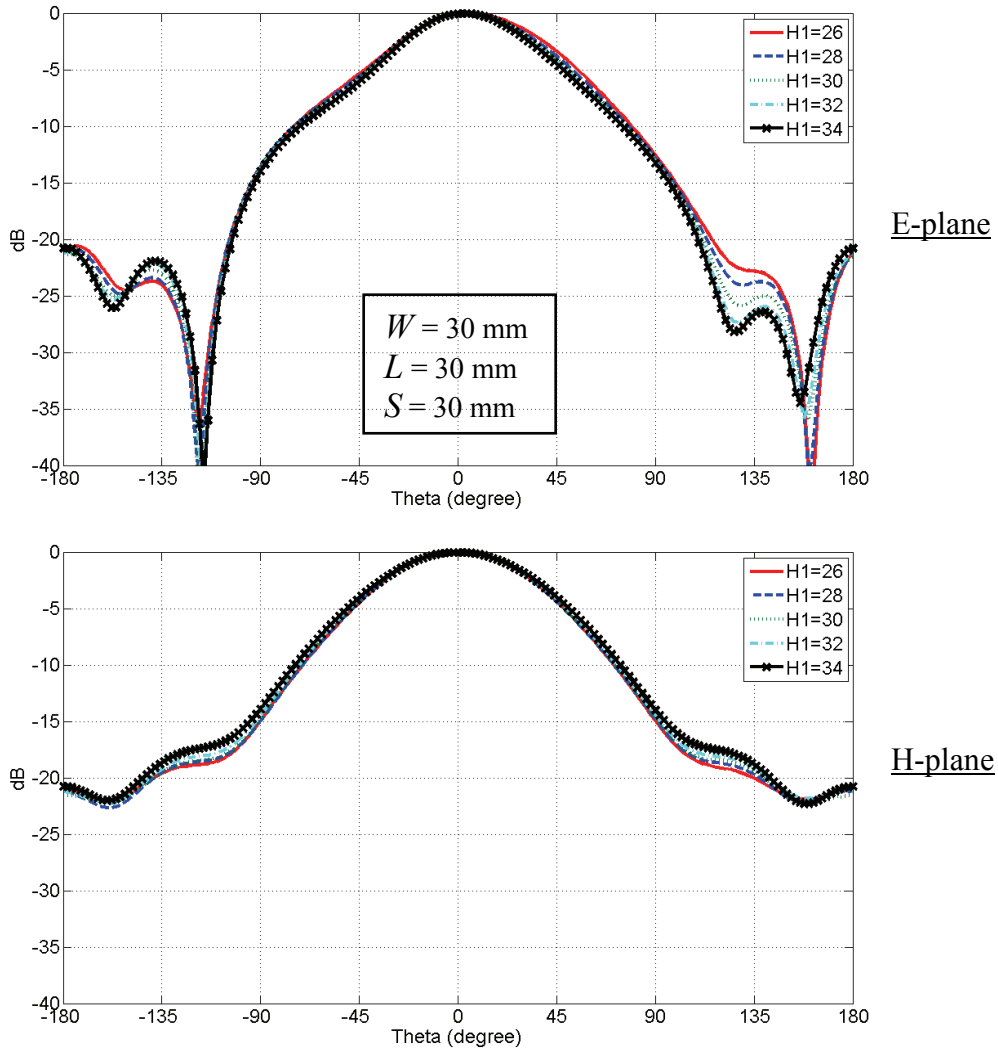

Fig. 2.22 Radiation pattern of the wideband patch antenna for different values of H_1

Table 2.11 3dB beamwidth and front-to-back ratio for different values of H_1

H_1 (mm)	3dB Beamwidth, E-plane	3dB Beamwidth, H-plane	Front-to-back Ratio
26	72^o	72^o	20.58 dB
28	68^o	72^o	20.86 dB
30	66^o	72^o	22.34 dB
32	64^o	76^o	21.15 dB
34	64^o	76^o	20.76 dB

2.3.3 Ground plane

Previously the studies for the hook-shaped probe and the radiating element of the antenna are discussed in section 2.3.1 and 2.3.2. In this section, we examine the effect of the ground plane size in terms of gain and radiation pattern. The values of other design parameters are chosen as a = 12 mm, b = 22 mm, W = 60 mm, L = 30 mm, S = 17 mm and H_1 = 30 mm.

2.3.3.1 Gain

The simulated gain of the antenna for different values of G_W versus frequency is shown in Fig. 2.23. The size of the *ground plane width* (G_W), which is equal to the *ground plane length* (G_L), is varied from 80 mm ($0.667\lambda_o$) to 240 mm ($2.000\lambda_o$) with 40 mm ($0.333\lambda_o$) step. The gain increases as G_W increases and the average gain in operating frequency range is around 8 to 9 dBi. The maximum gain is achieved as high as 9.03 dBi, but in the case of G_W = 80 mm, the maximum gain is dramatically reduced to 4.36 dBi.

Once the *ground plane width* (G_W) is bigger than 120 mm, the upper part of the gain curve doesn't change, but the lower part is still varying. This means that G_W =160 mm is sufficient length for an upper frequency of 3.0 GHz ($1.600\lambda_{o\_upper}$), but it is insufficient for a lower frequency of 2.0 GHz ($1.067\lambda_{o\_lower}$). In the case of G_W = 240 mm ($1.600\lambda_{o\_lower}$), the gain at lower frequency is maintained at same level as that at the center and upper frequencies. Hence it is preferable that the ground plane have at least a size of *1.6 wavelengths* of the lower frequency for the application where the very stable gain pattern is

required.

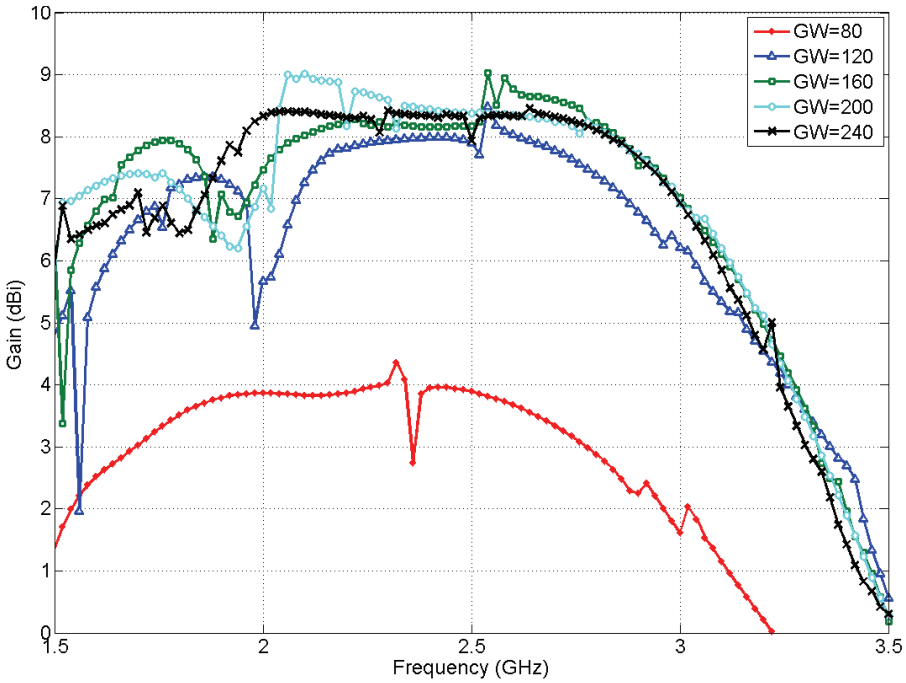

Fig. 2.23 Gain of the wideband patch antenna for different values of G_W

Overall, the gain curve is stable over the operating frequency band and the size of the ground plane is selected as G_W =160 mm for further fabrication.

2.3.3.2 Radiation pattern

Fig. 2.24 illustrates the radiation pattern of the antenna at the center frequency of 2.5 GHz for different values of G_W . Table 2.12 summarizes the 3dB beamwidth and front-to-back ratio in different cases. For the cases, the back radiation is suppressed to more than 20 dB when the *ground plane width* (G_W) is greater than 160 mm. When G_W = 200 mm, the maximum front-to-back ratio of 25.32 dB is observed.

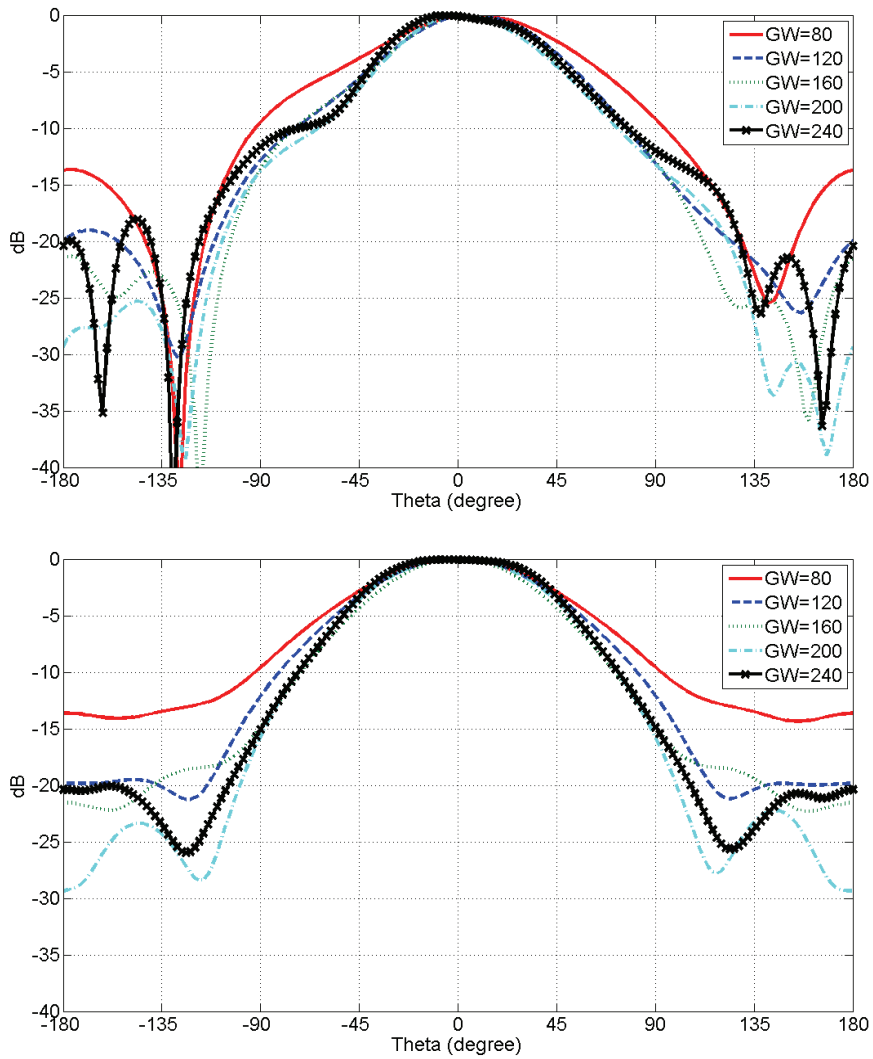

Fig. 2.24 Radiation pattern of the wideband patch antenna for different values of G_W

Table 2.12 3dB beamwidth and front-to-back ratio for different values of G_W

G_W (mm)	3dB Beamwidth, E-plane	3dB Beamwidth, H-plane	Front-to-back Ratio
80	88^o	92^o	13.63 dB
120	72^o	84^o	19.03 dB
160	66^o	72^o	21.34 dB
200	64^o	80^o	25.32 dB
240	74^o	88^o	20.05 dB

2.4 Enhancement of the bandwidth and gain

The proposed antenna has been fully investigated by parametric study for each component; the hook-shaped probe, the radiating element, and the ground plane in section 2.3. In this section, we extend our study for enhancing the performance of the antenna by modifying the hook-shaped probe as suggested in [46]. Instead of exciting the antenna using a single hook-shaped probe, twin hook-shaped probe is adopted for improving the bandwidth and gain of the antenna. Comparison of single hook-shaped probe and twin hook-shaped probe fed wideband antennas in terms of their input impedance, impedance bandwidth, and gain is discussed in this section.

2.4.1 Geometry modification

The modified configuration with twin hook-shaped probe is illustrated in Fig. 2.25. Two hook-shaped probes are located parallel to each other with separation of 39 mm ($0.33\lambda_o$), the *twin hook-shaped probe separation (e)*. A simple matching network, which is printed on the back of the same vertical substrate for the single hook-shaped probe case, excites the two hook-shaped metallic strips. A transmission line with characteristic impedance of 50Ω is connected to an SMA connector, which is located the bottom of the substrate, and branches into two 100Ω transmission lines for exciting the hook-shaped metallic strips. Dimensions for the *aperture width (S)* and the *metallic strip width (d)* are changed from the configuration of the single hook-shaped probe fed antenna for obtaining the optimized simulation results; other than that all other dimensions for the antenna remain the same.

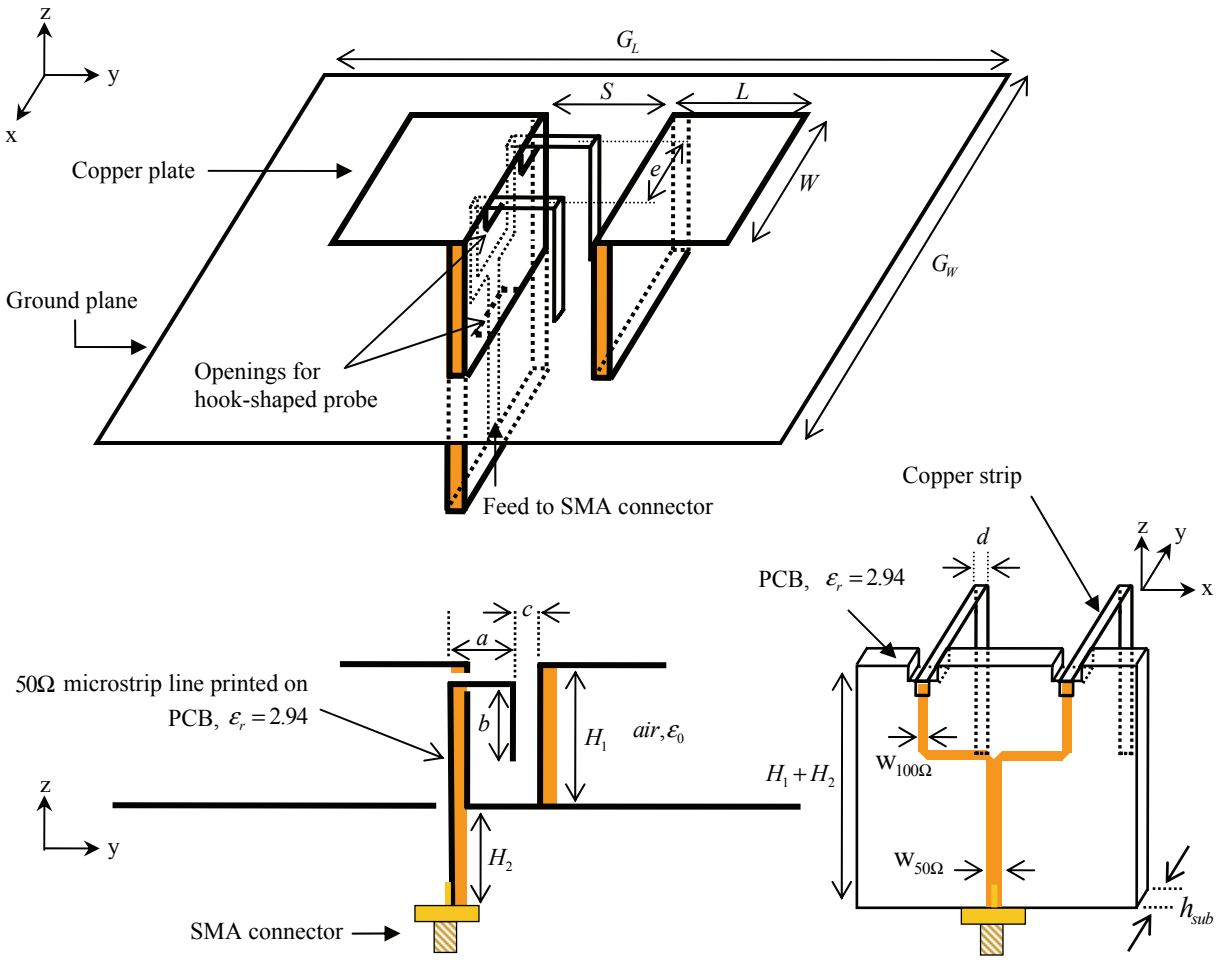

	a	b	c	d	e	W	L	S	H_1	H_2	G_L	G_W
Value / mm	11.5	26	3.024	1.613	39	60	30	13	30	35	160	160
	0.10 λ_0	0.22 λ_0	0.03 λ_0	0.01 λ_0	0.33 λ_g	0.50 λ_0	0.25 λ_0	0.11 λ_0	0.25 λ_0	0.29 λ_0	1.33 λ_0	1.33 λ_0

	$W_{50\Omega}$	$W_{100\Omega}$	h_{sub}
Value / mm	3.88	1.04	1.524
	0.06 λ_g	0.01 λ_g	0.01 λ_0

λ_g and λ_0 correspond to the center frequency of 2.5 GHz

Fig. 2.25 Configuration of a twin hook-shaped probe fed wideband patch antenna

2.4.2 Simulated results

Using the commercial EM simulator, HFSS, the effect of the twin hook-shaped probe feed is examined and the simulated result is compared with the single hook-shaped probe fed antenna. The thickness of the metallic strips and plates is assumed zero for relatively fast simulation. The summarized results are tabulated in Table 2.13.

Table 2.13 Simulated impedance bandwidth and gain for two different feeds

	Single-feed			Twin-feed		
BW($S_{11} \le -10dB$)	52.2%, 1.70 GHz ~ 2.90 GHz			84.4%, 1.26 GHz ~ 3.10 GHz		
Average Gain ^	8.03 dBi			8.18 dBi		
Maximum Gain	9.03 dBi			9.34 dBi		
	* Lower freq.	Center freq.	Upper freq.	+ Lower freq.	Center freq.	Upper freq.
3dB Beamwidth, E-plane	64^o	72^o	62^o	58^o	72^o	70^o
3dB Beamwidth, H-plane	84^o	80^o	72^o	80^o	72^o	60^o
Front-to-back Ratio	17.03 dB	22.14 dB	17.64 dB	12.16 dB	21.64 dB	22.77 dB
Max. X-polarization	-12.97 dB	-26.54 dB	-26.80 dB	- 14.76 dB	- 24.89 dB	- 30.34 dB

^ Average gain over the operating impedance bandwidth

* Single-feed : 1.7 GHz, 2.3 GHz and 2.9 GHz (lower, center, upper frequencies)

+ Twin-feed : 1.3 GHz, 2.2 GHz and 3.0 GHz (lower, center, upper frequencies)

2.4.2.1 Input impedance and reflection coefficient

Comparison of the simulated input impedance and reflection coefficient for the single and the twin hook-shaped probe fed antennas is shown in Figs. 2.26 and 2.27, respectively. In the frequency range from 1.7 GHz to 2.9 GHz of the Fig. 2.26, it can be observed that the first maxima of $\mathrm{Re}(Z_{11})$ for the single-feed at 1.84 GHz is shifted to the lower frequency of 1.66 GHz for the twin-feed case, while the second and third maxima of $\mathrm{Re}(Z_{11})$ for the single-feed at 2.10 GHz and 2.58 GHz are moved to the upper frequencies of 2.28 GHz and 2.90 GHz, respectively. The local maxima of $\mathrm{Re}(Z_{11})$ and $\mathrm{Im}(Z_{11})$ for the single-feed around 3 GHz are also shifted to around 3.6 GHz for the twin-feed case. The variation of the reactance for the single-feed is more than 100Ω, with range of -71Ω to 38Ω, whereas that for the twin-feed is less than 50Ω, with range of -26Ω to 22Ω.

As shown in Fig. 2.27, the impedance bandwidth for $S_{11} \leq$ -10dB for the twin-feed of 84.4% is achieved in the frequency range of 1.26 GHz to 3.10 GHz. Compared with the single-feed case, which has the impedance bandwidth of 52.2% from 1.70 GHz to 2.90 GHz, it can be observed that more than 60% of the impedance bandwidth is improved when the antenna is fed by twin hook-shaped probe.

2.4.2.2 Radiation pattern

Fig. 2.28 shows the simulated radiation patterns for the twin hook-shaped probe fed antenna at 1.3 GHz, 2.2 GHz and 3.0 GHz (lower, center, upper frequencies). Both Co-polarization and Cross-polarization in E-plane and H-plane are illustrated. The

Cross-polarization in the H-plane is not shown in the figure at the lower and the center frequencies because its level is below -40 dB. The 3dB beamwidths in the E-plane are 58^o, 72^o and 70^o at 1.3 GHz, 2.2 GHz, and 3.0 GHz, respectively; corresponding values in the H-plane are 80^o, 72^o, and 62^o. The level for the front-to-back ratio at the center and upper frequencies is greater than 20 dB, but it increases to -12.16 dB at the lower frequency. The maximum Cross-polarization level is -14.76 dB, -24.89 dB, and -30.34 dB at the lower, center, and upper frequency.

2.4.2.3 Gain

The simulated gain for two different feed configurations is plotted in Fig. 2.29. It can be observed that the gain for the twin-feed case is slightly higher than that for the single-feed configuration. For the twin hook-shaped probe feed, the average gain over the operating bandwidth is 8.18 dBi. The simulated gain for the single-feed is 8.03 dBi over the operating bandwidth. The maximum gain for the single and the twin hook-shaped probe fed antennas is 9.03 dBi and 9.34 dBi, respectively.

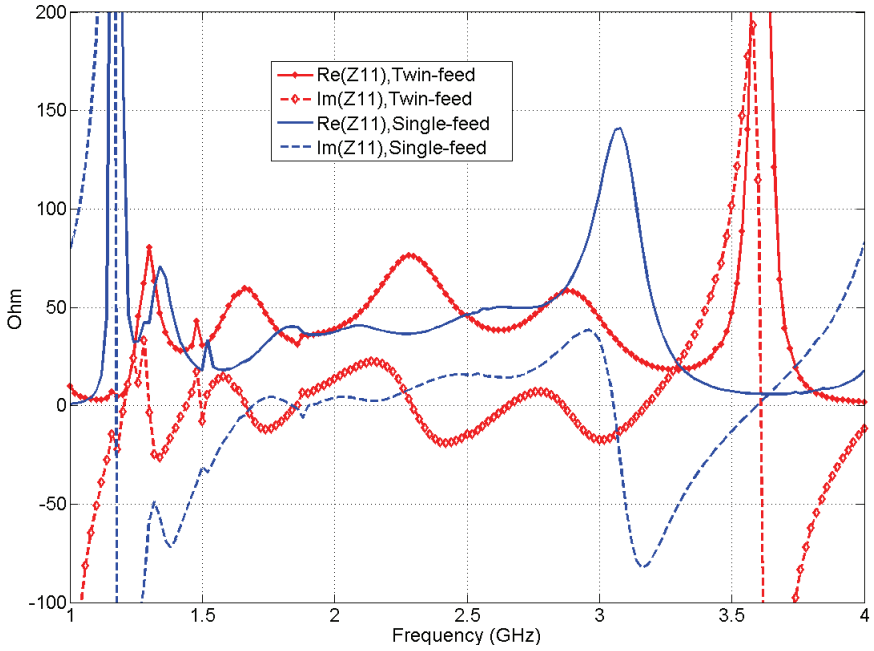

Fig. 2.26 Simulated input impedance for a single and a twin hook-shaped probe fed antennas

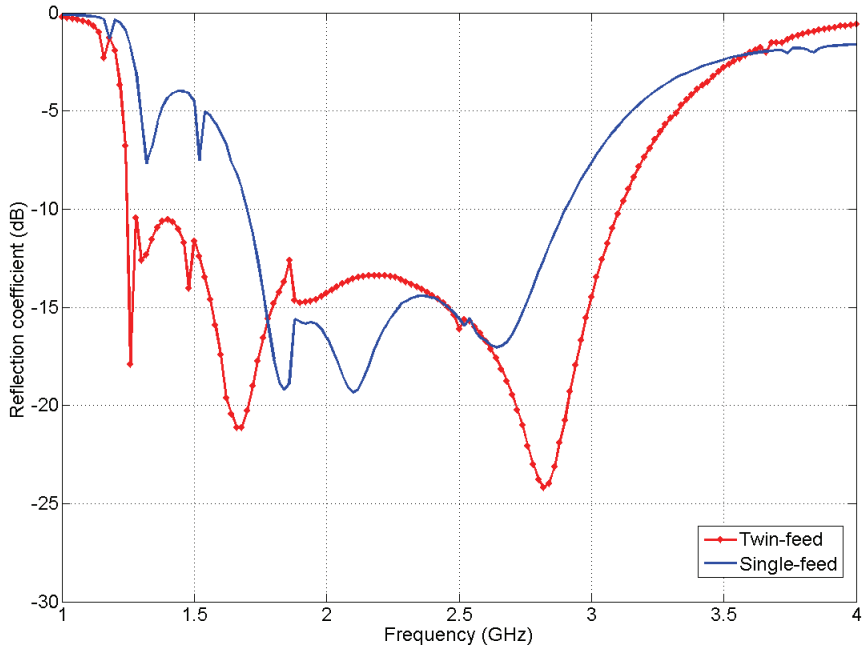

Fig. 2.27 Simulated reflection coefficient for a single and a twin hook-shaped probe fed antennas

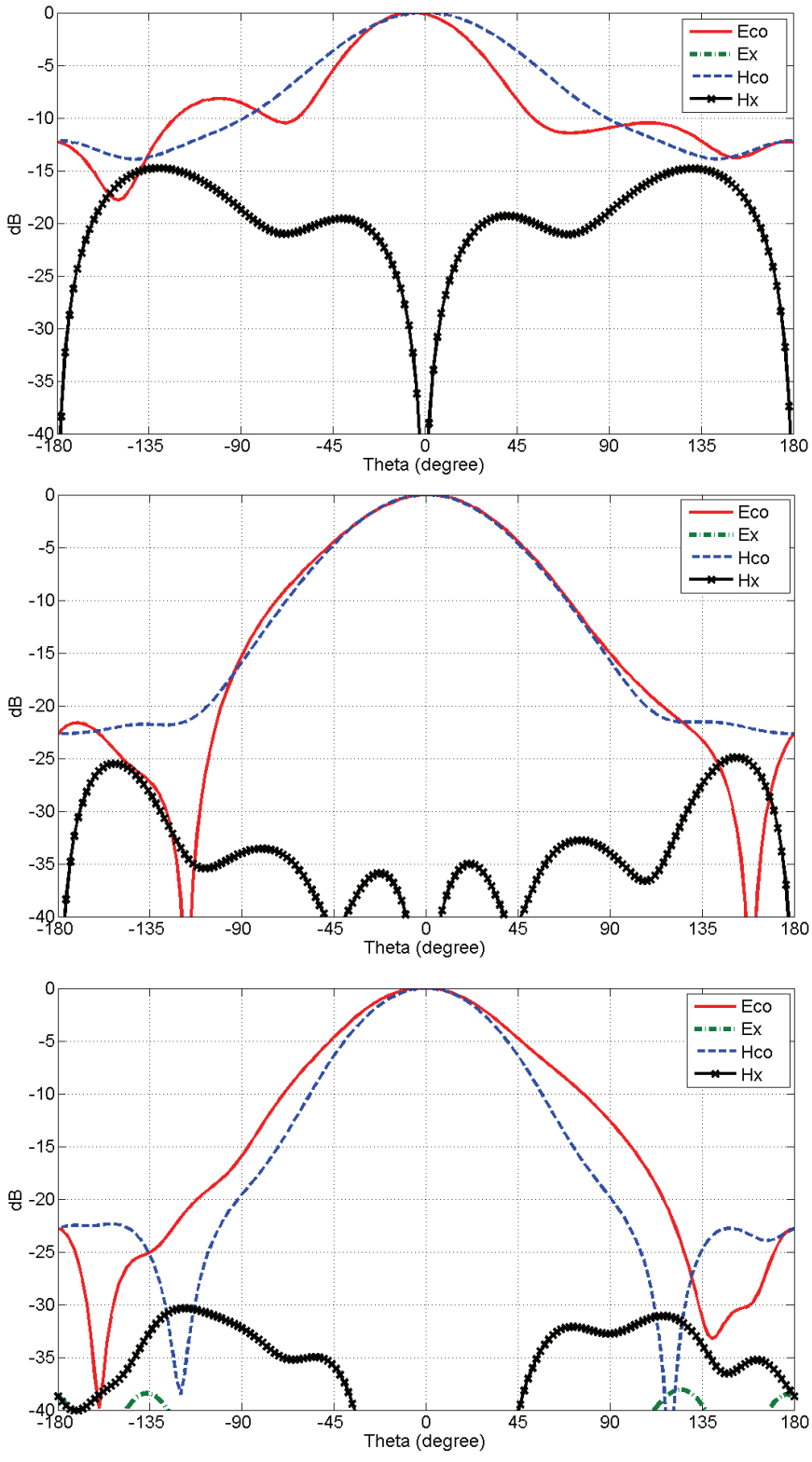

@ 1.3 GHz

@ 2.2 GHz

@ 3.0 GHz

Fig. 2.28 Simulated radiation patterns for a twin hook-shaped probe fed antenna

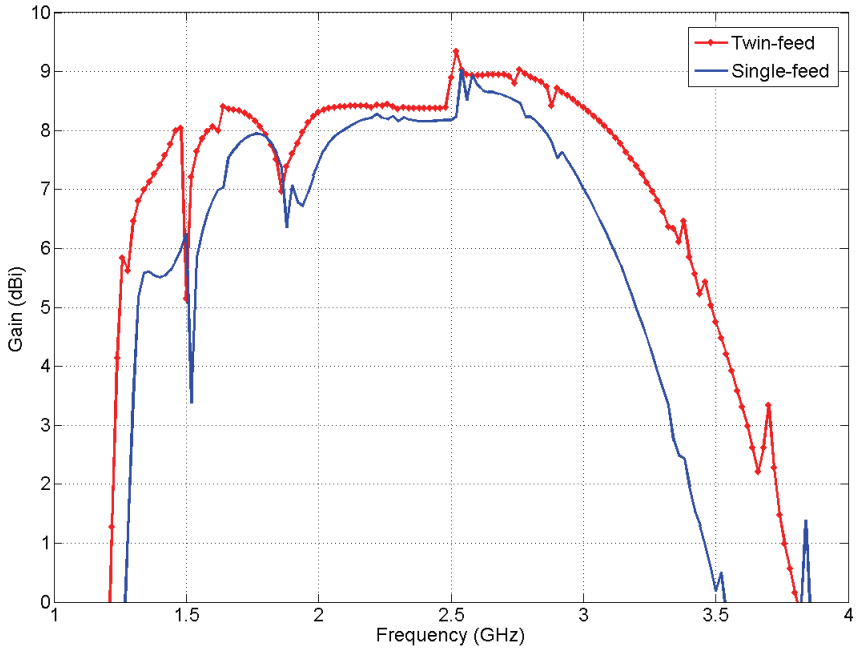

Fig. 2.29 Simulated gain for a single and a twin hook-shaped probe fed wideband antennas

2.5 Experimental verification

To verify the simulated results, prototypes of the proposed antenna were built and tested. Dimensions of the antenna for a single hook-shaped probe and a twin hook-shaped probe are listed in the tables inserted in Figs. 2.2 and 2.25, respectively. The pictures of the fabricated antennas are shown in Figs. 2.30 and 2.31. Experimental results of reflection coefficients were achieved using an HP8510C network analyzer and radiation patterns were measured using a compact range with an HP85103C antenna measurement system. Figs. 2.32 and 2.33 show comparisons between measured and simulated reflection coefficients of the proposed antenna with a single hook-shaped probe and a twin hook-shaped probe, respectively. For the single hook-shaped probe fed antenna, a wide impedance bandwidth of 53.2% from 1.74 GHz to 3.00 GHz is achieved. The twin hook-shaped probe fed antenna has a wider impedance bandwidth of 72.3% from 1.50 GHz to 3.20 GHz. The summarized results are tabulated in Table 2.14.

Table 2.14 Comparison of measured and simulated bandwidth for two different feeds

BW($S_{11} \le -10dB$)	Single-feed	Twin-feed
Measurement	53.2%, 1.74 GHz ~ 3.00 GHz	72.3%, 1.50 GHz ~ 3.20 GHz
Simulation	52.2%, 1.70 GHz ~ 2.90 GHz	84.4%, 1.26 GHz ~ 3.10 GHz

Figs. 2.34 and 2.35 illustrate measured radiation patterns at 1.75 GHz, 2.50 GHz, and 3.00 GHz for a single hook-shaped probe fed antenna and at 1.55 GHz, 2.50 GHz, and 3.20 GHz for a twin hook-shaped probe fed antenna, respectively. For both the E- and

H-planes, the broadside radiation patterns are symmetric and stable over the operating bandwidth. Low cross polarization level and low back radiation are maintained across the entire operating bandwidth. Relatively high back radiation is observed for the twin hook-shaped probe at 1.55 GHz due to a relatively small electrical length of the ground plane.

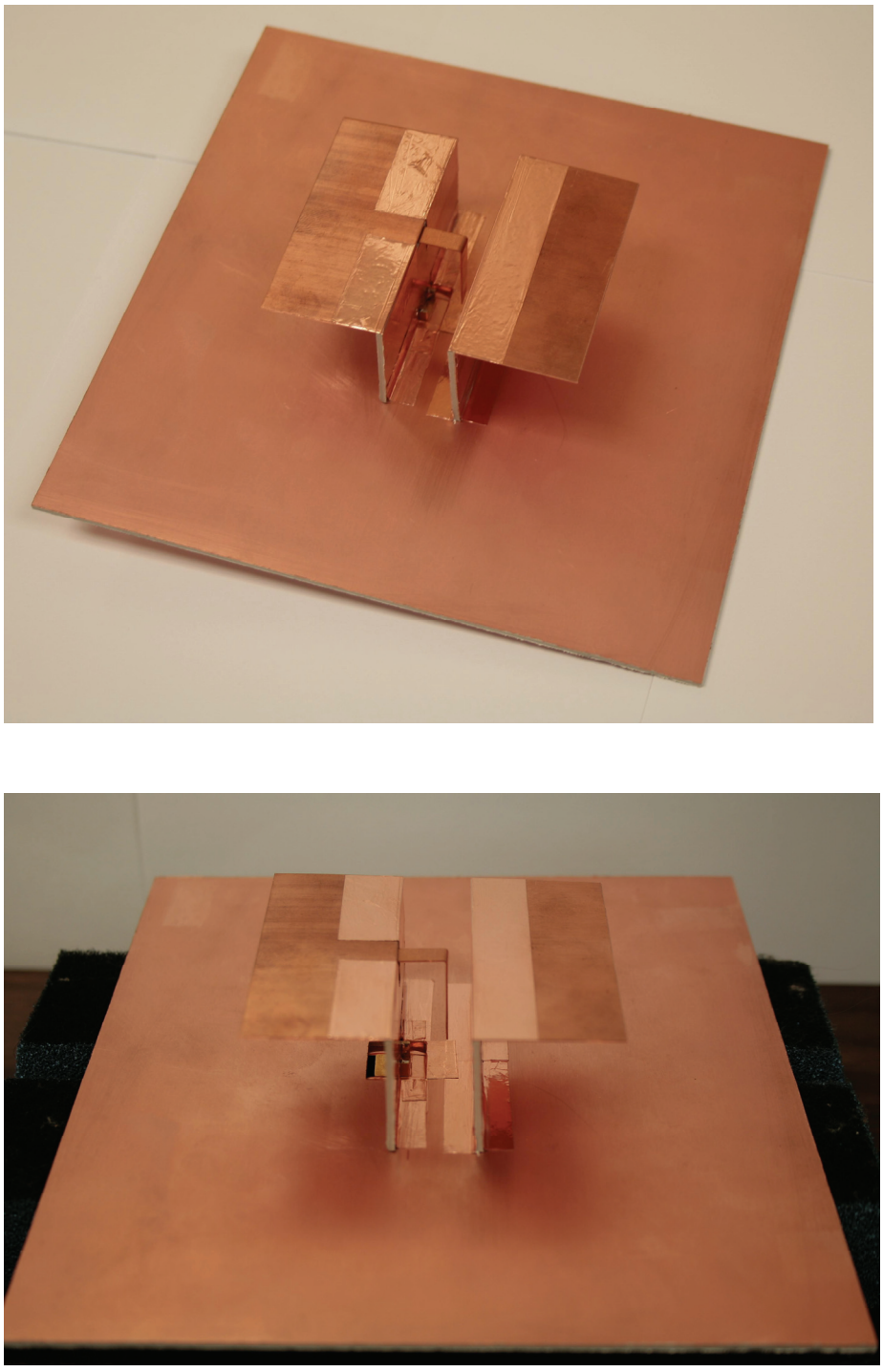

Fig. 2.30 Photograph of a wideband antenna fed by a single hook-shaped probe

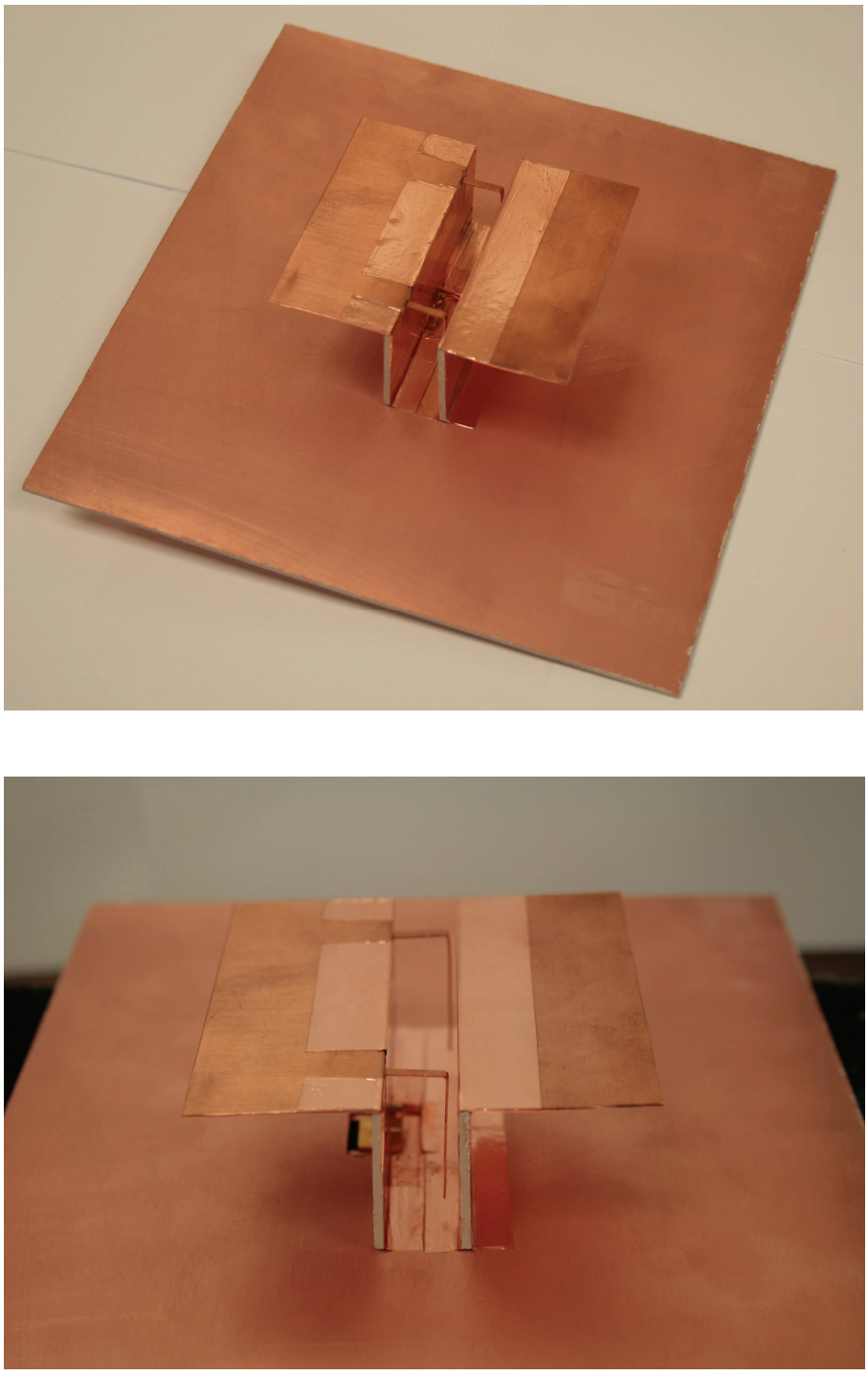

Fig. 2.31 Photograph of a wideband antenna fed by a twin hook-shaped probe

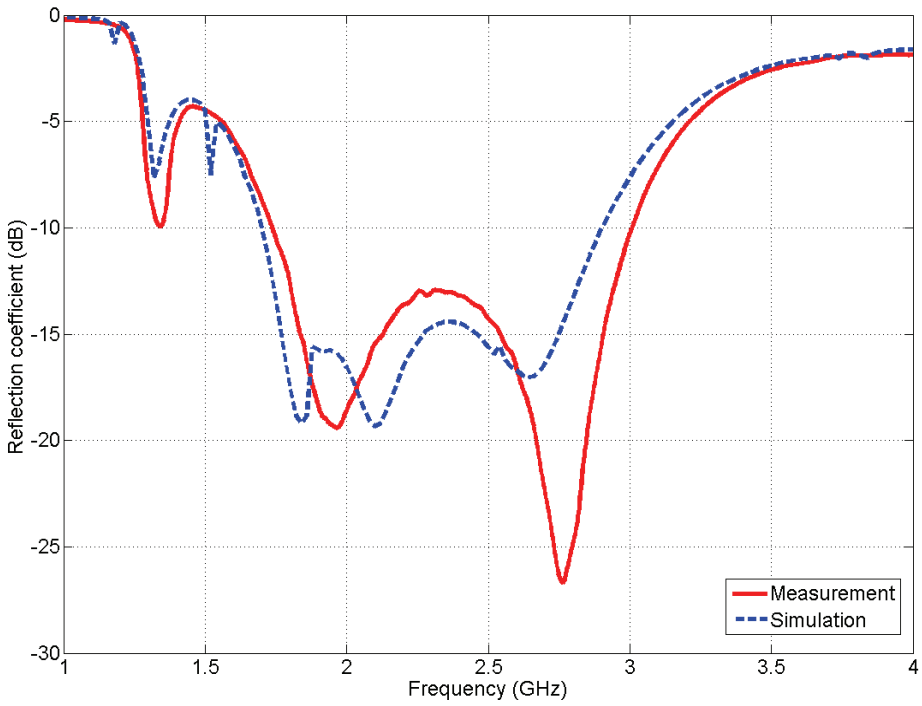

Fig. 2.32 Measured and simulated reflection coefficients for a single hook-shaped probe

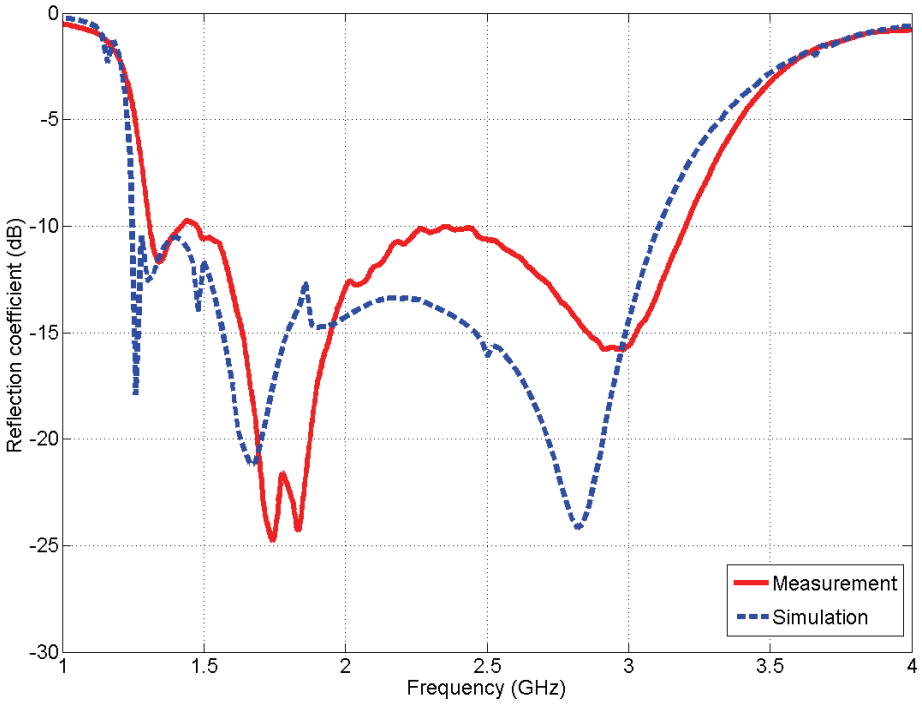

Fig. 2.33 Measured and simulated reflection coefficients for a twin hook-shaped probe

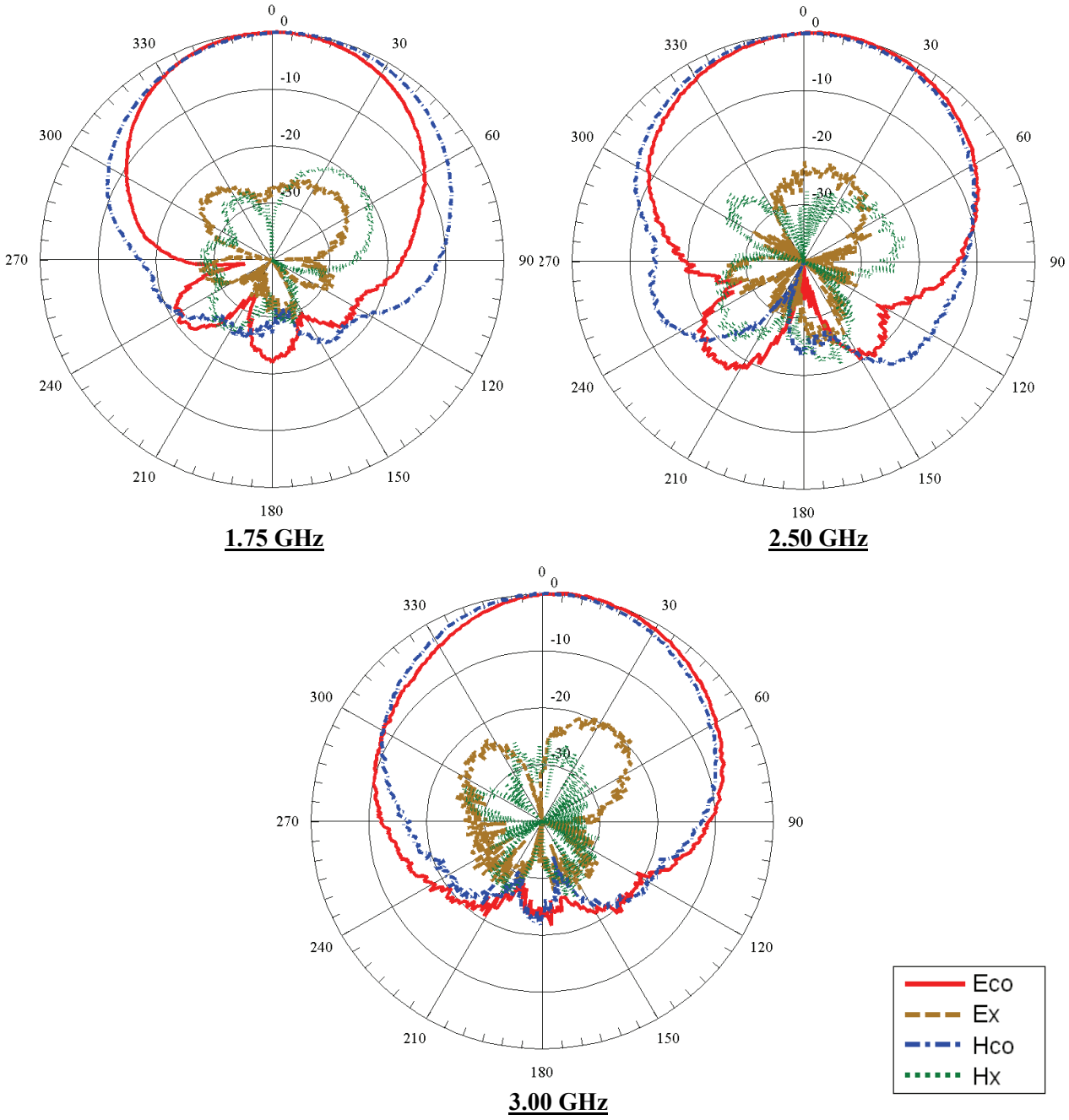

Fig. 2.34 Measured radiation patterns for a single hook-shaped probe fed antenna

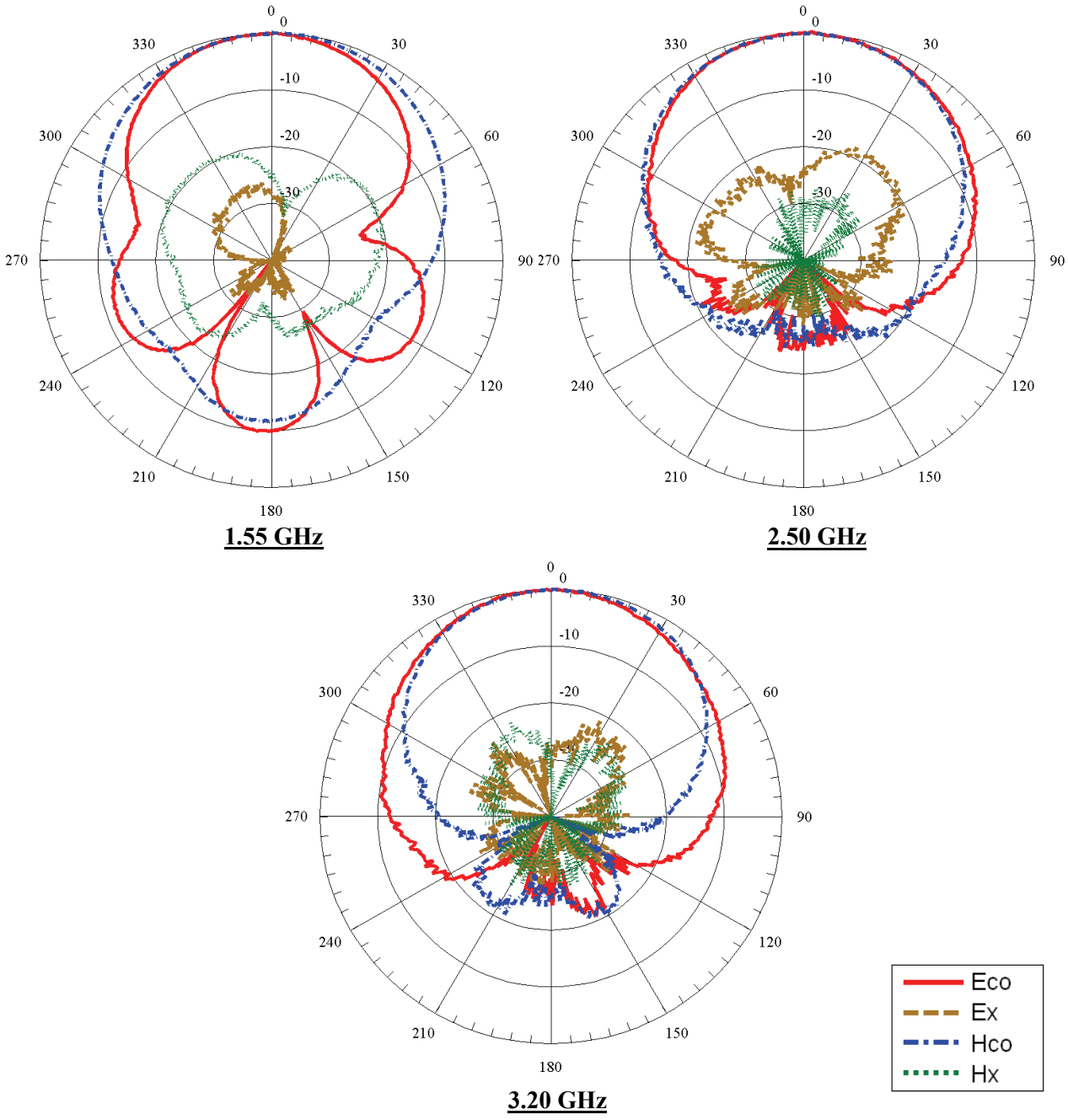

Fig. 2.35 Measured radiation patterns for a twin hook-shaped probe fed antenna

CHAPTER III

A DUAL-POLARIZED WIDEBAND PATCH ANTENNA WITH SHIELDED DIELECTRIC LOADING

3.1 Introduction

In chapter II, a wideband linearly polarized antenna with shielded dielectric loading is designed and tested. Based on the previous study, we have extended our study to a wideband dual-polarized antenna for its attractive characteristics, such as frequency reuse and polarization diversity. Due to the complexity of the dual-polarized antenna compared with linearly polarized antenna, there are many challenges to design such an antenna with excellent electrical characteristics of broad impedance bandwidth, low cross-polarization level, high isolation, and stable radiation pattern.

Recently, the concept of wideband unidirectional complementary antenna [36,37] has been extended to design a dually polarized antenna with dielectric material loading [45]. By introducing the dual-polarization from the linearly polarized antenna in [45], however, the input impedance bandwidth of the proposed antenna is reduced from 48 % to around 24 %. This is not only because of changing the physical dimension of the antenna, but also because of loading the dielectric materials, which might limit the performance regarding the impedance bandwidth, in the effective radiating region of the antenna.

In the present study, we are interested in improving of the impedance bandwidth of the dual-polarized antenna by shielding of the dielectric materials from the radiating region,

as introduced in chapter II of the linearly polarized patch antenna. The technique for shielding can effectively prevent the deterioration of the impedance bandwidth; meanwhile other excellent characteristics of the antenna, such as high isolation, high cross-polarization level, and radiation pattern, still remain. In addition to the wideband performance, the back-lobe level of the radiation pattern for the dual-polarized antenna is improved by employing the conventional back-lobe suppression technique, i.e., the addition of metallic side walls [47,48].

3.2 Antenna description

The concept of the dual-polarized antenna, which is extended from the linearly polarized antenna design, is illustrated in Fig. 3.1. Instead of having one slot along the vertical direction in Fig. 3.1 (a) and (b), a second slot is introduced along the horizontal plane for the dual-polarized antenna with four hook-shaped probes as shown in Fig. 3.1 (c).

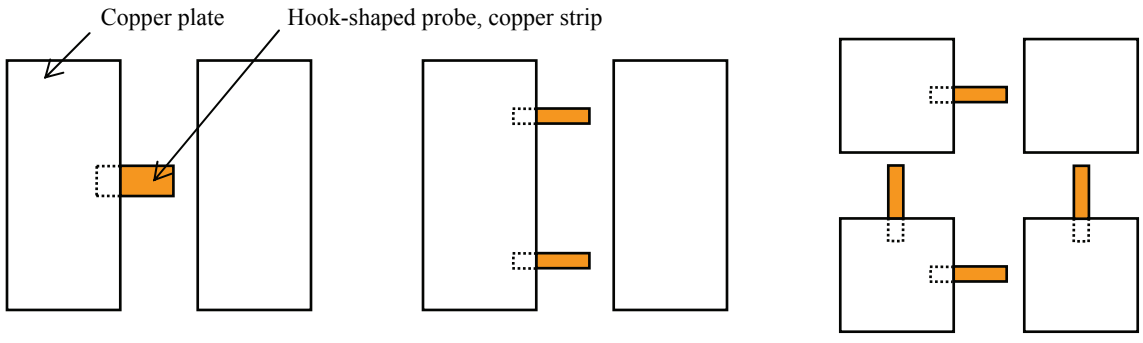

(a) Linear pol. w/ single hook-shaped probe

(b) Linear pol. w/ twin hook-shaped probes

(c) Dual pol. w/ four hook-shaped probes

Fig. 3.1 Principle of a dual-polarization from the linear polarization

The configuration of the dual-polarized wideband patch antenna with shielded dielectric substrate operated at 2.5 GHz with detail dimensions is shown in Fig 3.1. The antenna consists of four horizontal square patches above the finite ground plane and two vertical feeding substrates. Each patch of the antenna, which is located 30 mm ($0.25\lambda_o$, λ_o refers to the center frequency of operation) above the ground plane, has a dimensions P×P = 30×30 mm^2 . The patches are shorted to the ground plane by the vertical feeding substrates. The same size of the ground plane as for the linearly polarized patch antenna in chapter II is used for the dual polarized case and its dimension is $G_W \times G_L$ = 160 mm×160 mm ($1.33\lambda_o \times 1.33\lambda_o$). The separation between patches, *aperture width (S)*, is 13 mm.

Details of the two vertical feeding substrates with dielectric constant of 2.94 and thickness of 1.524 mm are also shown in Fig. 3.2. One substrate is oriented in the YZ-plane and the other is in the XZ-plane. As illustrated in Fig. 3.2(b), both substrates are orthogonally arranged to each other. A simple matching network is printed on one side of each vertical feeding substrate to deliver the signal from the SMA connector to the metallic hook-shaped feeding strips, whereas the other side of the vertical feeding substrate is filled by copper as a ground plane for the microstrip transmission line. The metallic strips are extended through an opening where the vertical shorted wall and the top horizontal patch meet, with size of 5 mm by 1 mm. A small 5 mm by 1 mm rectangular portion of the ground plane is also removed where the hook-shaped probe connects to the microstrip feed line to avoid shorting the feed.

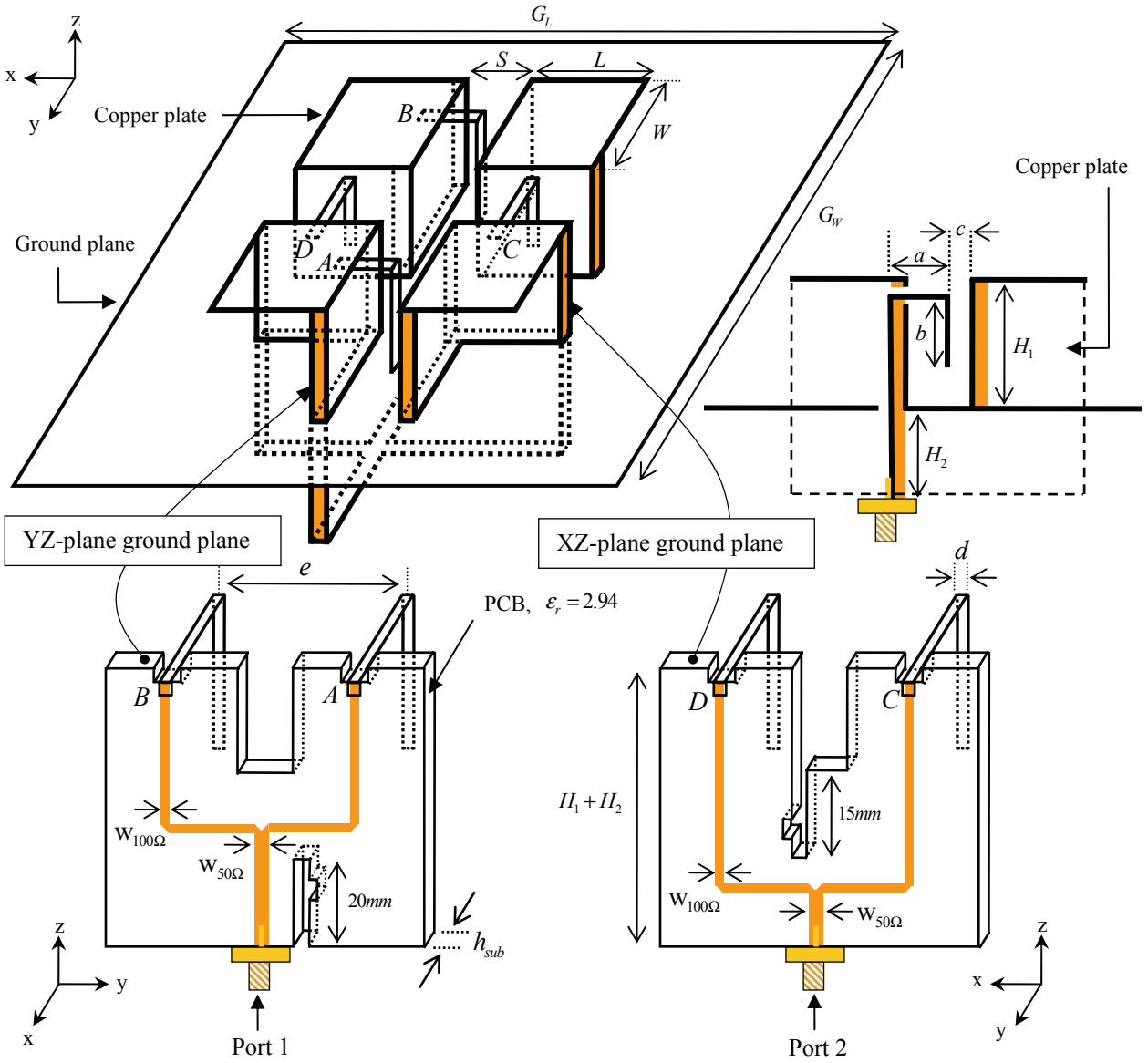

	a	b	c	d	e	W	L	S	H_1	H_2	G_L	G_W
Value / mm	12.024	22	2.5	1.6	39	30	13	13	30	35	160	160
	0.10 λ_0	0.22 λ_0	0.03 λ_0	0.01 λ_0	0.33 λ_g	0.25 λ_0	0.25 λ_0	0.11 λ_0	0.25 λ_0	0.29 λ_0	1.33 λ_0	1.33 λ_0

	$W_{50\Omega}$	$W_{100\Omega}$	h_{sub}
Value / mm	3.88	1.04	1.524
	0.06 λ_g	0.01 λ_g	0.01 λ_0

λ_g and λ_0 correspond to the center frequency of 2.5 GHz

Fig. 3.2 Configuration of a dual-polarized wideband patch antenna

3.3 Excitation of the antenna

As discussed earlier, the excitation of the dual-polarized patch antenna is composed of two main components:

1. Hook-shaped probe feed
2. Vertical matching network

Points A, B, C, and D shown in Fig. 3.2 are the connecting points between four hook-shaped probe feeds and two vertical substrates with matching networks.

3.3.1 Hook-shaped probe feed

Four hook-shaped probe feeds are employed to excite the antenna. Each probe consists of two portions, which are made by bending a rectangular metallic strip into a hook shape. The first portion, which is located horizontally, is coupled with nearby two horizontal patches. One end of this portion at points A, B, C, and D, is connected to the matching network by soldering. The length of this portion controls the input impedance of the antenna because this portion introduces inductive reactance which can cause a mismatch.

The second portion, which is oriented vertically, acts as open circuited transmission line. This line over the shorted metallic wall is an equivalent circuit model of capacitor and its capacitive reactance can compensate the mismatch from the inductive reactance of the first portion. Hence the length of these two portions of the hook-shaped probe feeds, *a* and *b*, along with the position of these feeds give more degrees of freedom to the design and an

optimization of these values is an important step to increase the impedance bandwidth of the antenna.

3.3.2 Matching network

Two separated vertical feeding networks, which are printed on printed circuit boards (PCB) of thickness of 1.524 mm and ε_r = 2.95, are located on back of the shorted metallic walls that support the patches. By shielding all matching networks inside these walls, the effect of the dielectric material in the region between the two vertical shorting walls can be minimized.

The scheme of a simple in-phase matching network is employed to excite the dual-polarized patch antenna. The hook-shaped probes at points A and B have the in-phase excitation of the feeding network, which is connected to an SMA connector (port 1). In the same manner the hook-shaped probes at points C and D have the same phase excitation by another feeding network, which is connected to another SMA connector (port 2). In order to match the input impedance of 50 ohms, microstrip lines, which are connected with hook-shaped probe feeds at the points A, B, C, and D, have characteristic impedance of 100 ohms. Hence two parallel 100 ohm microstrip lines give a 50 ohm characteristic impedance line and the input impedances at the SMA connectors can be matched. The only difference between the two vertical feeding networks is the length of the 50 ohm microstrip line in order to avoid the intersection between the two feeding networks and minimize the coupling effects between them.

3.4 Simulation, fabrication and measurement set-up

The Ansoft HFSS commercial software, a full-wave FEM-based simulator, is used for examining the performance of the dual-polarized wideband antenna with shielded dielectric loading. As in chapter II, the thickness of the metallic strip and plate are assumed to be zero for relatively fast simulation.

3.4.1 Fabrication

The above designed antenna was fabricated in the antenna fabrication facility at our department using the LPKF Protomat-91S milling machine. The substrate used was obtained from the Rogers Corporation as a sample of the RT/duroid 6002 with dielectric constant of 2.94 and thickness of 1.524 mm. Some photos of the fabricated prototype are shown in Figs. 3.3 to 3.5.

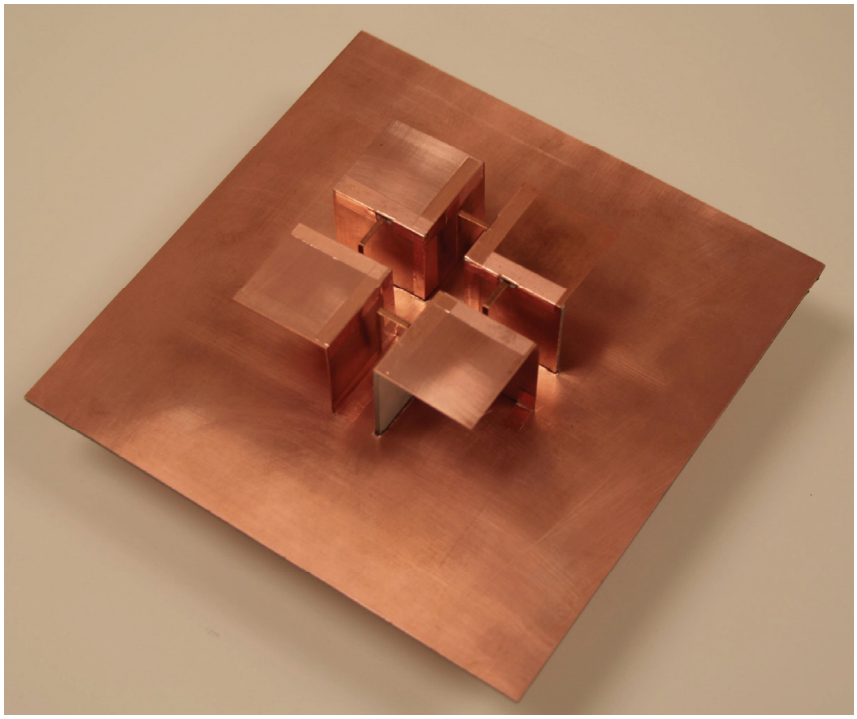

Fig. 3.3 Perspective view of the fabricated dual-polarized patch antenna

(a) Horizontal ground plane alone (b) Horizontal ground plane w/ antenna

Fig. 3.4 Top view of the fabricated dual-polarized patch antenna

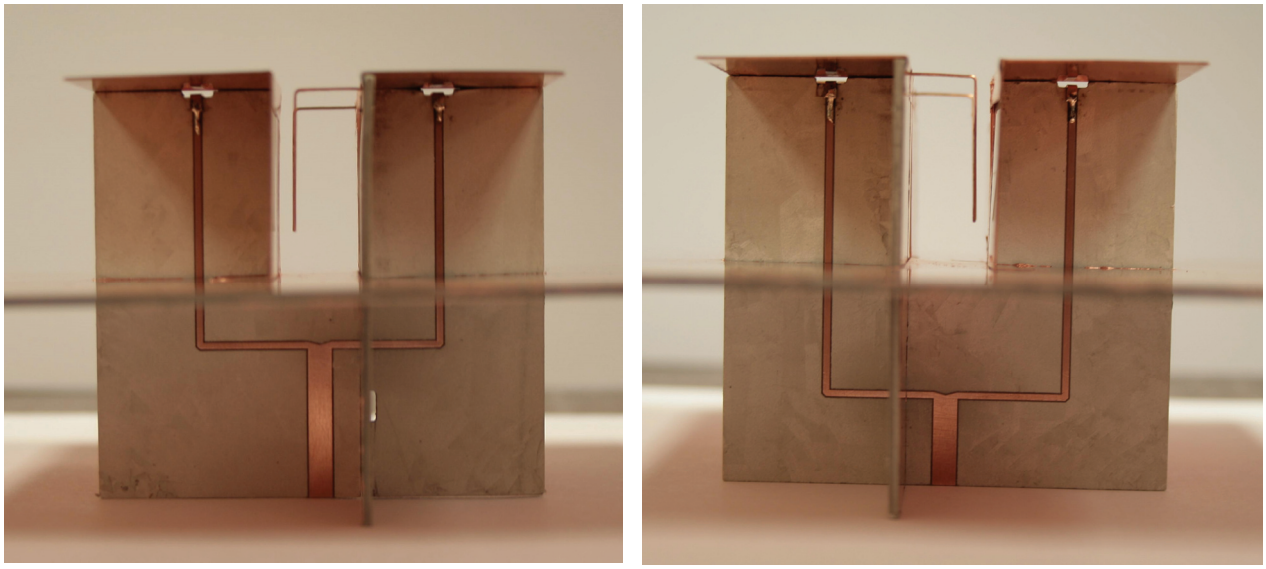

(a) YZ-plane cut view (b) XZ-plane cut view

Fig. 3.5 Side views of the fabricated dual-polarized patch antenna

Choosing the thickness of the copper plate - The patches and hook-shaped probes are made of a copper sheet with thickness of 16 mil (26 gauge). We stress that choosing the right thickness of the copper sheet is important in the fabrication process. Too thin copper, which is easily bent by hand, can not hold the square patches and the probes straight, and copper that is too thick makes it difficult to cut narrow probes with width of 1.04 mm with the cutting tools. The thickness of the copper sheet available in industry ranges from 1 mil to 22 mil and above. Sample copper sheets for 10 mil and 16 mil are examined. The 16 mil copper sheet is more rigid and less pliable than the thinner one. The 10 mil one can be used to create a 90 degree bend by hand, but the 16 mil one can be bent with tools. For the narrow and sharp hook-shaped probe, the 16 mil one is selected.

Assembling antenna – In order to assemble the pieces of patches and vertical substrates, an electrical copper tape from 3M is used. It is important that all vertical substrates and walls are required to touch the ground plane firmly. The horizontal ground plane used is the same sample for the substrate because it is easy to cut using the milling machine. Each edge of the ground plane is covered by the copper tape to have same ground level from the top and the bottom of its ground plane. A photo of the fabricated ground plane of the prototype is shown in Fig. 3.4.

3.4.2 Measurement set-up

The fabricated patch antenna is tested using the HP 8510C network analyzer. Full 2-port measurements (S11, S12, S21 and S22) can be taken from the network analyzer. The radiation patterns are measured using an anechoic chamber in antenna measurement facility at our department. The measurement set-up in the anechoic chamber is shown in Fig. 3.6. Each input port of the dual-polarized patch antenna is fed one at a time; meanwhile the other input port is matched. For the accuracy of the cross polarization measurement, the following factors are considered thoroughly:

1. Source horn's vertical / horizontal rotated position
2. Alignment of the source horn and a device under test (DUT)
3. Minimizing any reflection from a scanning pillar and a feeding cable

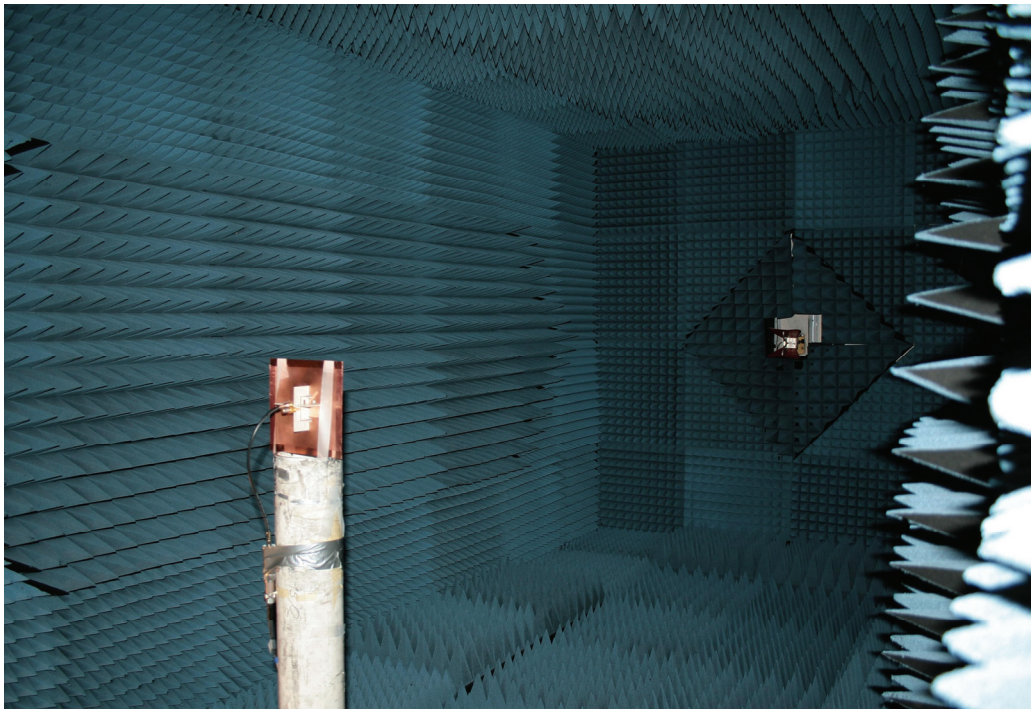

Fig. 3.6 Radiation pattern measurement set-up of the dual-polarized patch antenna

3.5 Performance evaluation of the designed antenna

The designed antenna is simulated using Ansoft HFSS commercial software, a full-wave FEM-based EM simulator, to evaluate its performance, which is measured in terms of following factors:

1. Reflection coefficient at port 1 and port 2
2. Isolation between the two input ports
3. Radiation patterns for both co-polarization (Co-pol.) and cross-polarization (X-pol.) at lower, center, and upper frequencies
4. Gain over the operating frequency range

Reflection coefficients of the dual-polarized patch antenna at port 1 and port 2 represent the input impedance matching bandwidth for each port. Common bandwidth for two input ports will be discussed for the dual-polarized antenna. The isolation level between two input ports shows how much one port is physically isolated from the other port, and it is desired to have maximum isolation between the two ports. Especially the cross-polarization of the radiation pattern is important in many dual-polarization antenna applications to minimize the cross talk between the two polarizations. Stable gain over the operating frequency bandwidth is preferable in addition to the wide bandwidth.

3.5.1 S-parameters

The measured and simulated reflection coefficient and isolation of the dual-polarized antenna are shown in Figs. 3.7 and 3.8, respectively. The simulated input

impedance bandwidths of the antenna are 64.4% ($S_{11} \leq -10$ dB) from 1.79 GHz to 3.49 GHz and 61.3% ($S_{11} \leq -10$ dB) from 1.81 GHz to 3.41 GHz for ports 1 and 2, respectively. From the measurement results of the reflection coefficient, the antenna is operated from 1.71 GHz to 3.59 GHz with input impedance bandwidth of 70.9% and from 1.74 GHz to 3.50 GHz with input impedance bandwidth of 67.2% for ports 1 and 2, respectively. Compared with the simulated result, the measurement reflection coefficient at port 1 shows the performance of the antenna has slightly deteriorated by about 2 dB difference at the center frequency to be -8.5 dB. This is probably due to the inaccuracy for the width and position of the hook-shaped probes.

Both simulated and measured isolation between the two input ports are shown in Fig. 3.8. Isolation levels are kept below about -35 dB from 2.18 GHz and above in the HFSS simulation and from 2.29 GHz and above in the measurement. At lower frequencies of the operating bandwidth, both simulated and measurement results show relatively low isolation levels up to -18 dB and -22 dB in simulation and measurement, respectively. These results indicate the need for further study to improve the isolation level, especially at the lower frequencies, and this will be discussed more in a later part of this chapter. It is observed that the measured isolation level is better than -28 dB for the operating frequency of 1.93 GHz and above.

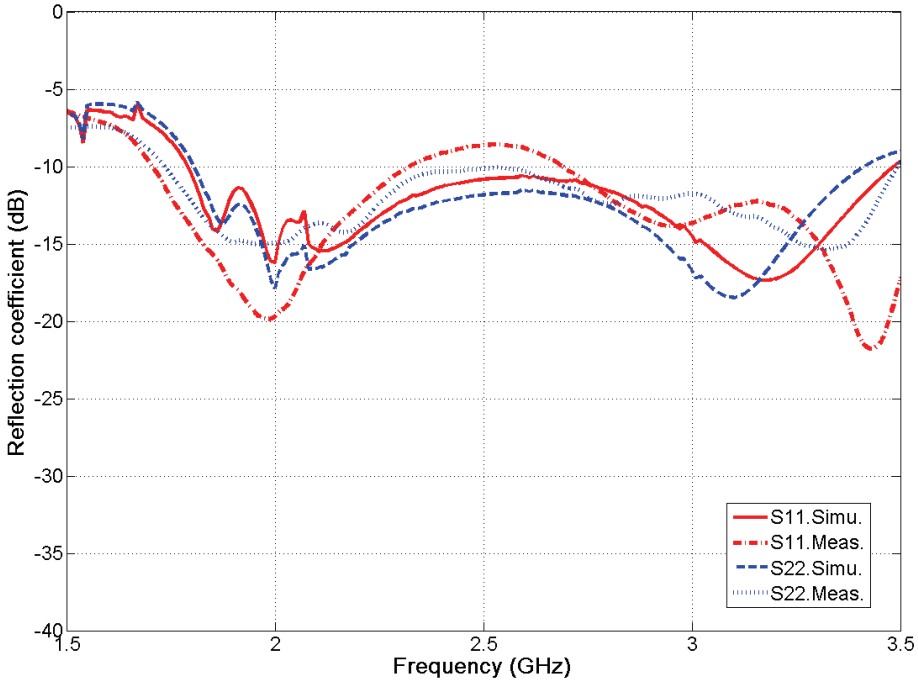

Fig. 3.7 Measured and simulated reflection coefficient of the dual-polarized patch antenna

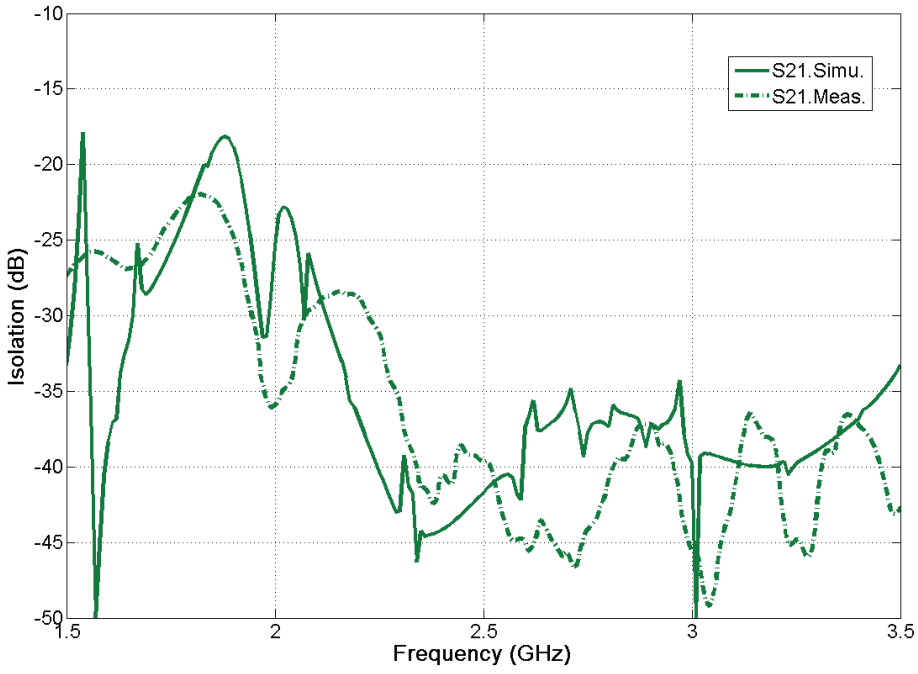

Fig. 3.8 Measured and simulated isolation of the dual-polarized patch antenna

3.5.2 Radiation patterns

The measured and simulated radiation patterns at ports 1 and 2 at 2.1 GHz, 2.7 GHz, and 3.4 GHz are plotted in Figs. 3.9 to 3.11. Each figure has four curves of measured co- and cross-polarizations and simulated co- and cross-polarizations at a specified plane-cut and frequency. The measured co-polarization radiation patterns are in good agreement with the simulated results. It is observed that both the XZ-plane and YZ-plane radiation patterns are stable over the entire operating frequency band and symmetrical to the broadside direction. The back radiations at lower frequency, which are relatively high compared with those at other frequencies, are about -14 dB for both ports 1 and 2. The radiation patterns at that frequency are also slightly deteriorated because of the relatively small electrical length of the ground plane at that frequency. This will be discussed in a later part of this chapter to minimize the back-lobe level without increasing the size of the ground plane.

From the simulation results using HFSS, the cross-polarization levels of the radiation patterns are less than -26 dB over the operating frequency band. The measured ones are as high as -15 dB at the upper frequency. It is notable that the cross-polarization levels at the lower and center frequencies are less than -20 dB, but only those at the upper frequency are relatively high as -17 dB. This is probably due to the accuracy factors, which are discussed previously in section 3.4.2, and which are more sensitive at the higher frequency. Therefore misplacement of the source horn's position or different levels of the source horn and the device under test yields huge difference between the simulation and the measurement.

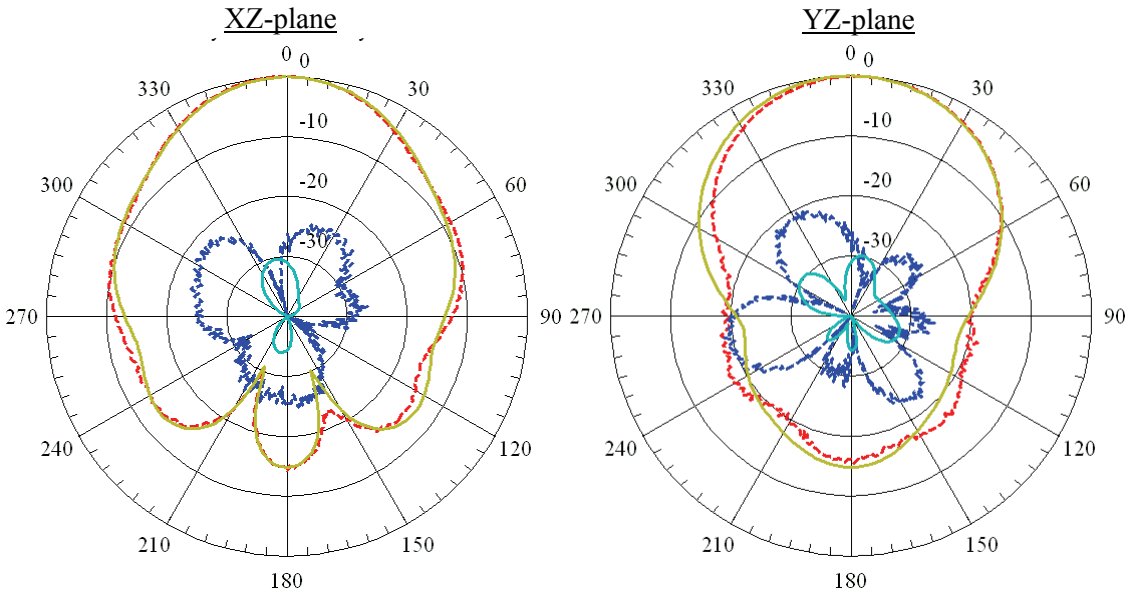

Fig. 3.9(a) Measured and simulated radiation pattern at 2.1 GHz of port 1

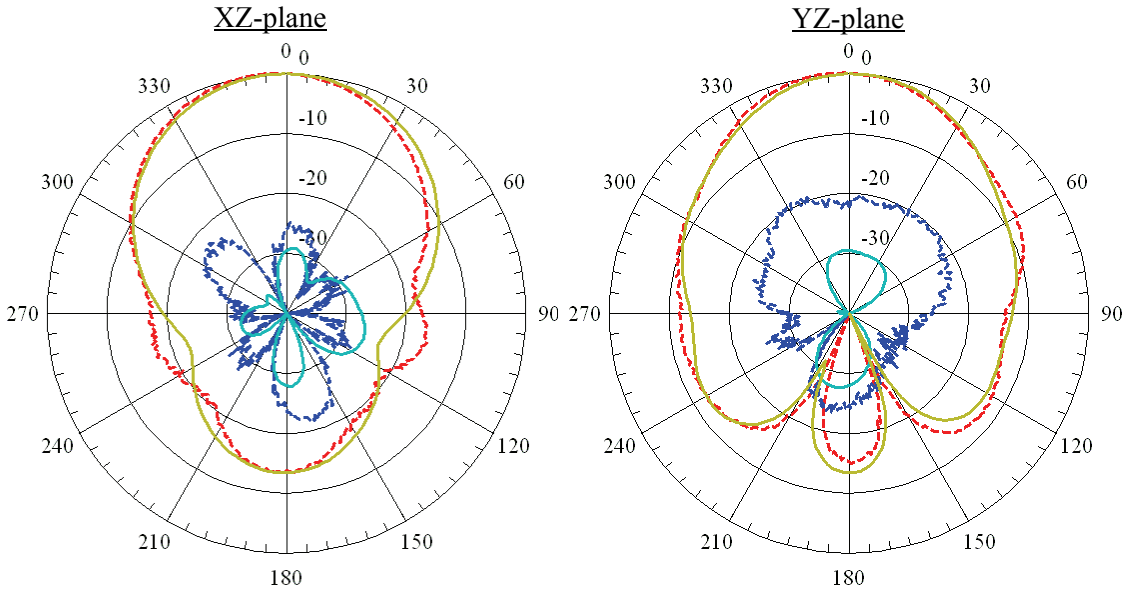

Fig. 3.9(b) Measured and simulated radiation pattern at 2.1 GHz of port 2

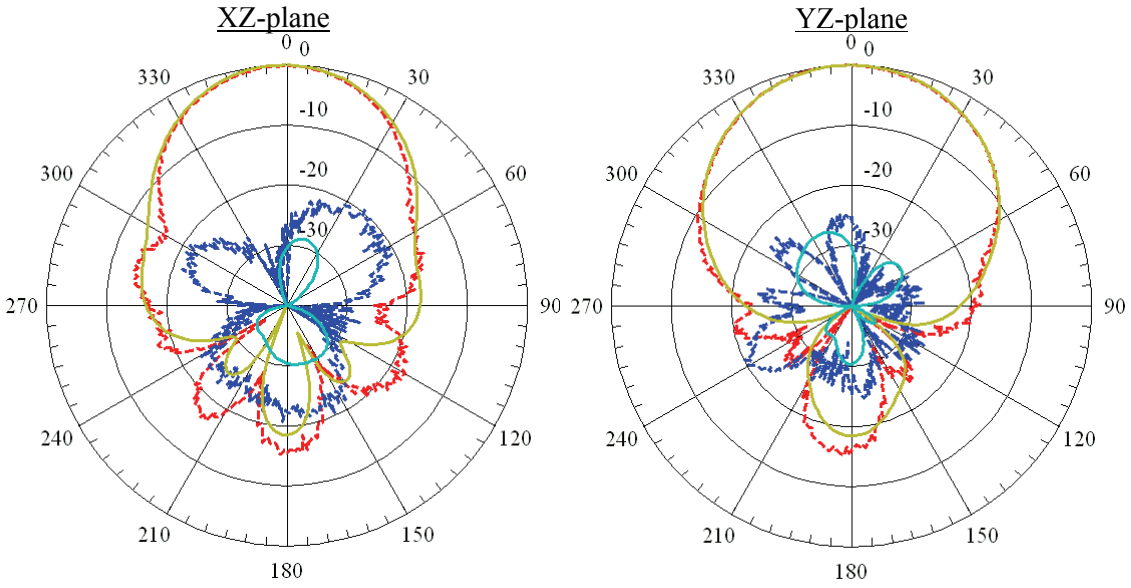

Fig. 3.10(a) Measured and simulated radiation pattern at 2.7 GHz of port 1

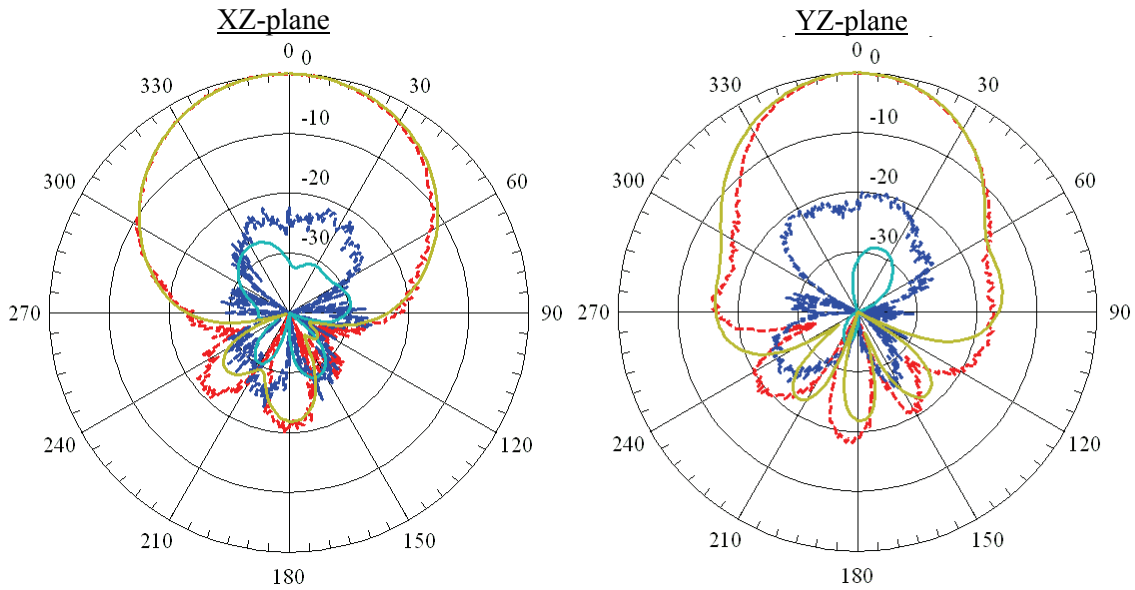

Fig. 3.10(b) Measured and simulated radiation pattern at 2.7 GHz of port 2

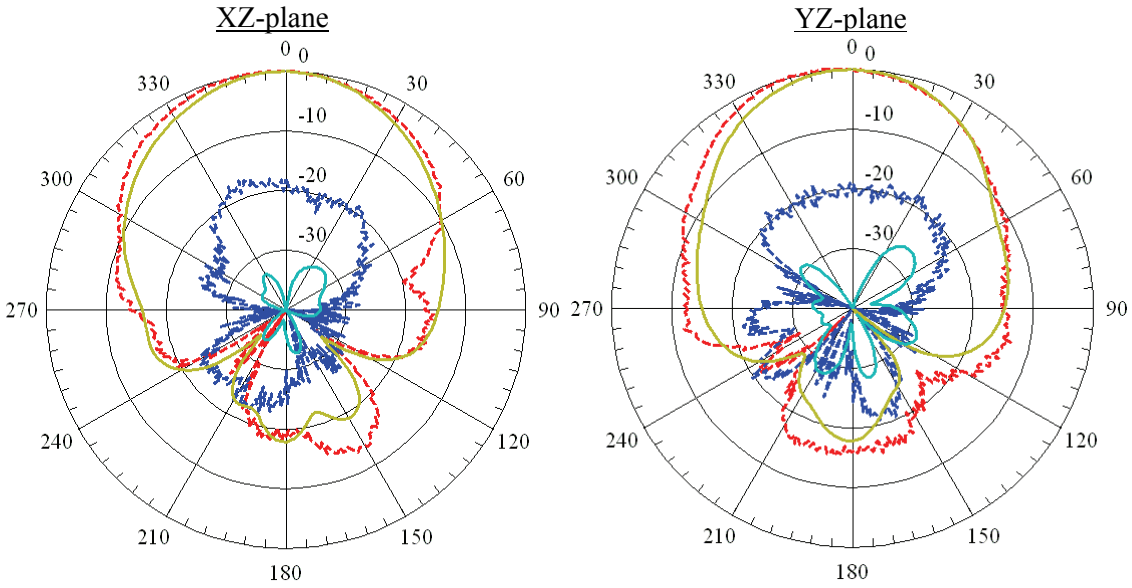

Fig. 3.11(a) Measured and simulated radiation pattern at 3.4 GHz of port 1

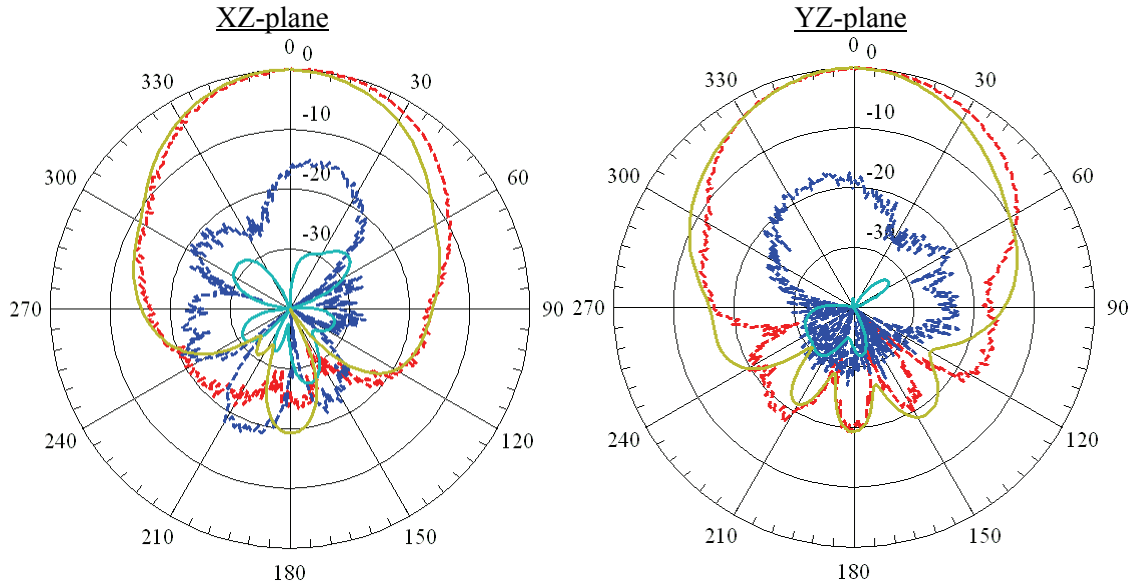

Fig. 3.11(b) Measured and simulated radiation pattern at 3.4 GHz of port 2

3.5.3 Gain

Fig. 3.12 illustrates the simulated gain of the designed antenna over the operating frequency range. The maximum gain of the antenna is about 10.1 dBi, and the 3-dB gain bandwidth ranges from 1.89 GHz to 3.50 GHz, which covers almost the entire common input impedance bandwidth, which is corresponding to range of 1.81 GHz to 3.41 GHz in simulation. It is worthwhile to comment that this antenna has a very stable gain over the operating frequency band.

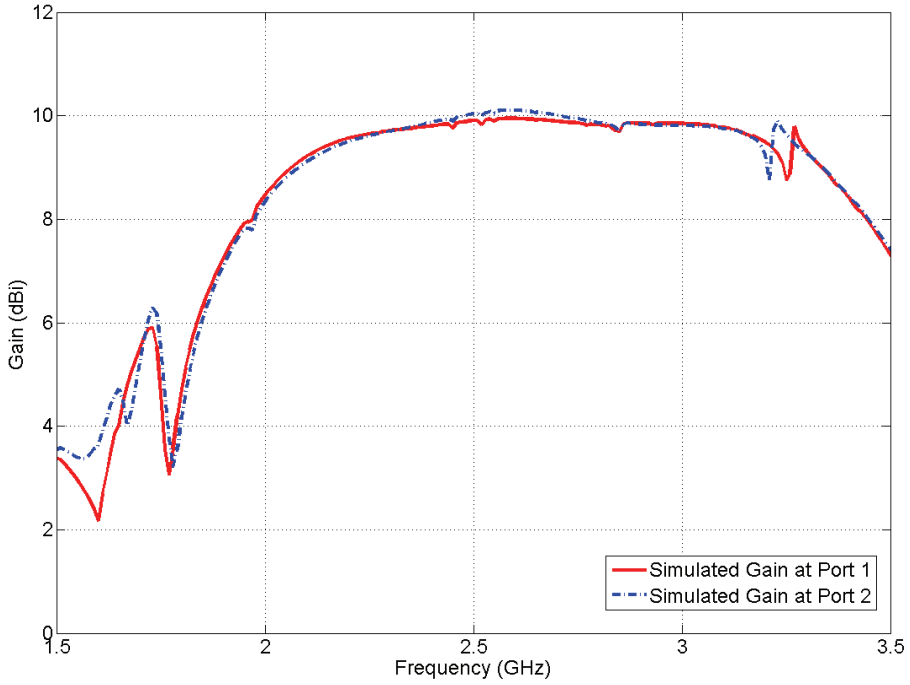

Fig. 3.12 Simulated gain of the dual-polarized patch antenna

3.6 Enhancement of the isolation and the radiation pattern

After designing the antenna, further studies are examined for enhancing the performance of the antenna, such as improving the isolation level and reducing the levels of the back radiation lobes. It is observed that a modified antenna has great improvements on the isolation and back radiation pattern.

3.6.1 Increasing the opening for isolation improvement

As described in Fig. 3.8, the isolation of the dual-polarized antenna deteriorates at the lower frequencies of the operating band. The reason for this deterioration is mainly due to the narrow opening around the microstrip line in the vertical ground plane that crosses the orthogonal ground plane.

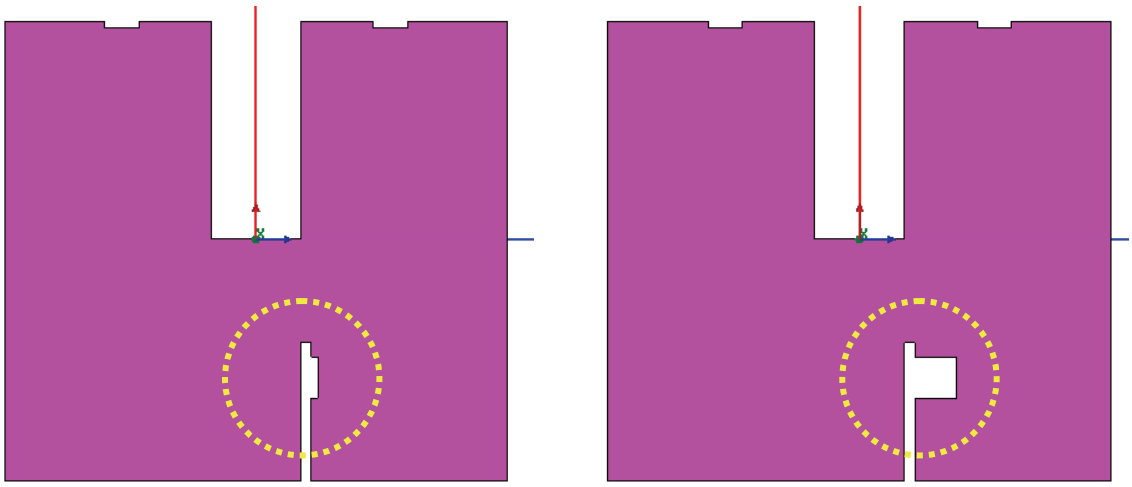

(a) Narrow opening (b) Wide opening

Fig. 3.13 Schematic of the vertical ground plane with different sizes of the opening

The modified vertical ground plane, whose opening is increased, is illustrated in Fig. 3.13. In the circle of the Fig. 3.13 (a) represents the narrow opening area where the

length of the opening has only 1 mm ($0.007\lambda_0$ at the lower frequency of 2.1 GHz) distance above the microstrip line. After parametric study to find an optimum opening, the dimension for the length of the opening was selected as 6 mm ($0.042\lambda_0$ at the lower frequency of 2.1 GHz) as shown in Fig. 3.13 (b).

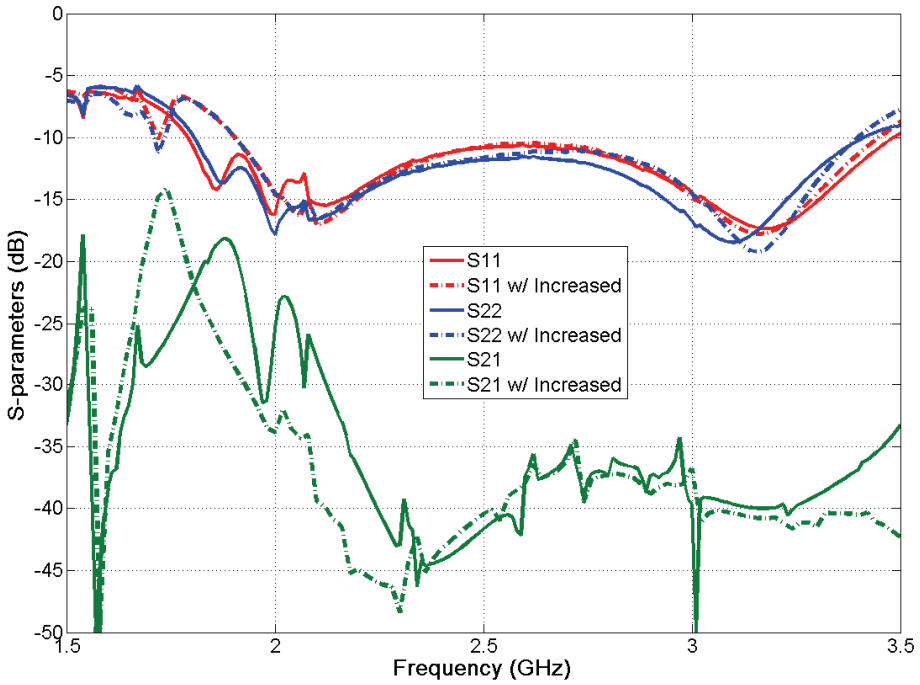

Fig. 3.14 Simulated S-parameters of the dual-polarized antenna with increased opening

The simulated S-parameters of the antenna with increased opening, which are plotted in Fig. 3.14, show that the increased opening improves the isolation level effectively. The simulated isolation is better than 29.6 dB across the entire operating bandwidth of the modified antenna. The opening area doesn't affect much the reflection coefficient at ports 1 and 2. Only slight decreases of the input impedance bandwidth are

observed at the lower frequency band. It is notable that the opening area has an effect particularly at the lower frequency band because the relatively small electrical length opening around the microstrip line affect more significant at the lower frequency band than the upper one.

3.6.2 Adding the metallic side wall for radiation pattern enhancement

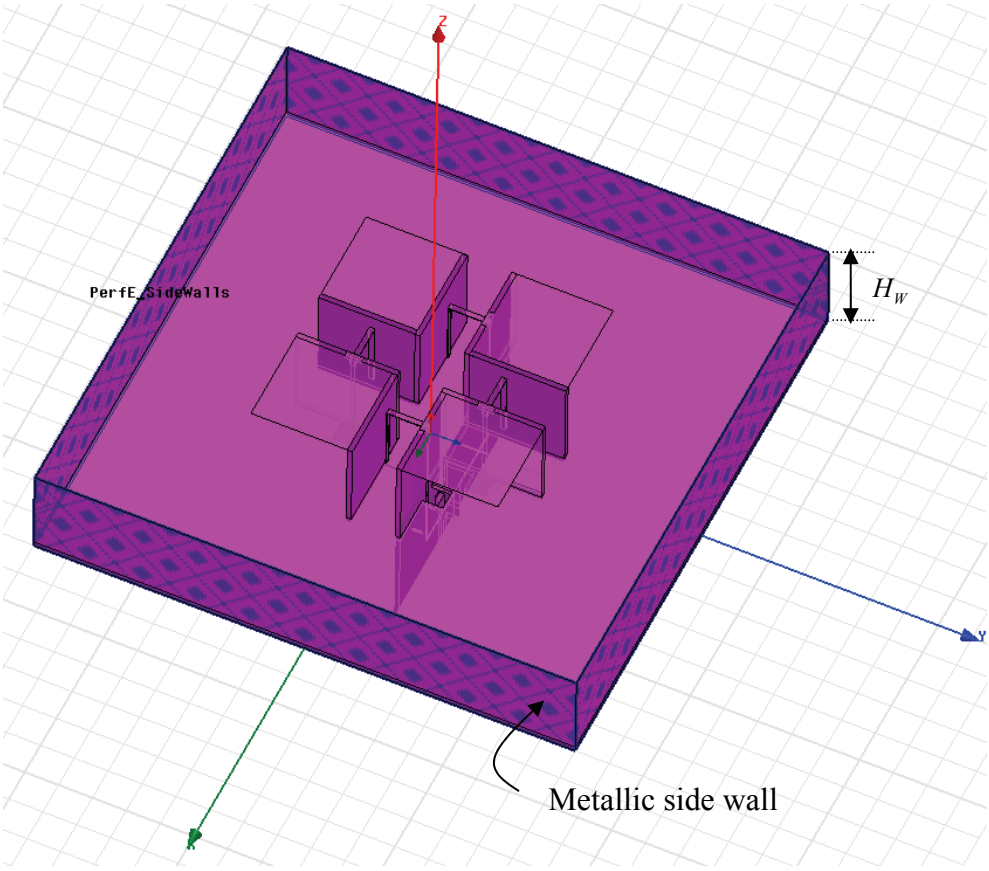

Fig. 3.15 Configuration of the dual-polarized patch antenna with metallic side wall

Although the designed antenna has already symmetric and stable radiation patterns, it has a relatively large back radiation at lower frequency band because of the small ground

plane. Instead of increasing the size of the ground plane, a vertical side wall is employed for radiation pattern enhancement. A simulation study for the antenna with different H_w, the height of the vertical side wall, is conducted to examine the effect of the metallic side wall as shown in Fig. 3.15. The thickness of the metallic wall in the simulation is assumed to zero for demonstrating the concept only.

3.6.2.1 S-parameters

Fig. 3.16 illustrates the simulated reflection coefficient with different H_w = 0 mm, 15 mm, and 30 mm. From the obtained results, it is found that the reflection coefficient and the isolation are not sensitive to the presence of the vertical metallic side wall. The antenna can maintain the wide impedance bandwidth of more than 55 % (S_{11} ≤ -10dB) when the metallic side wall is placed at the edge of the ground plane.

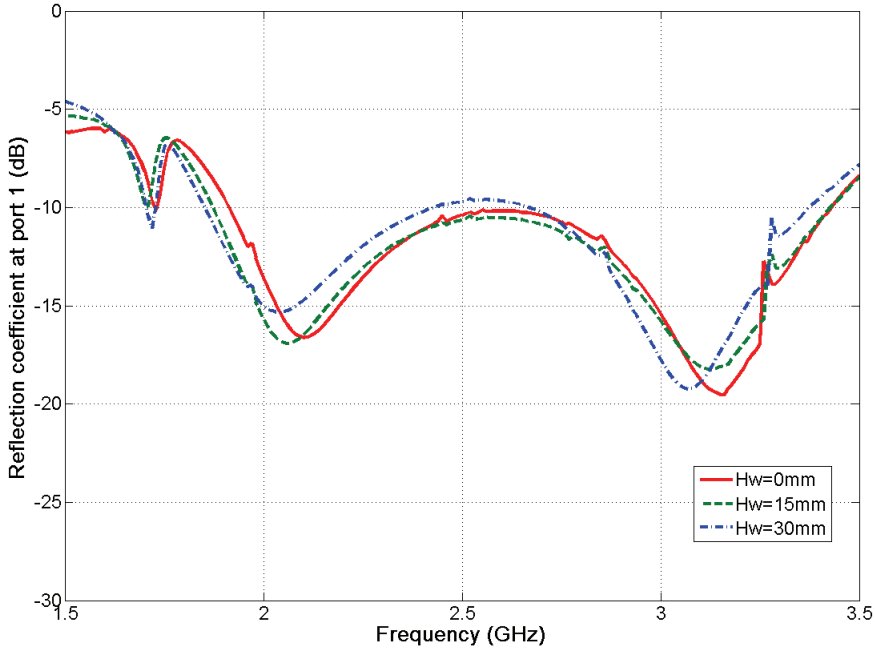

Fig. 3.16(a) Simulated reflection coefficient at port 1 with different heights of side wall

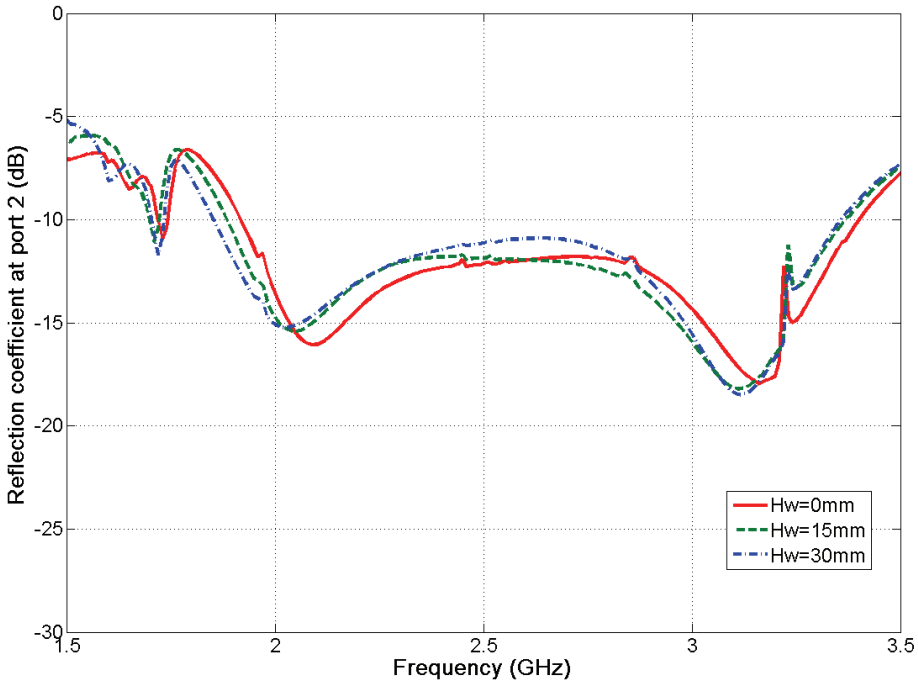

Fig. 3.16(b) Simulated reflection coefficient at port 2 with different heights of side wall

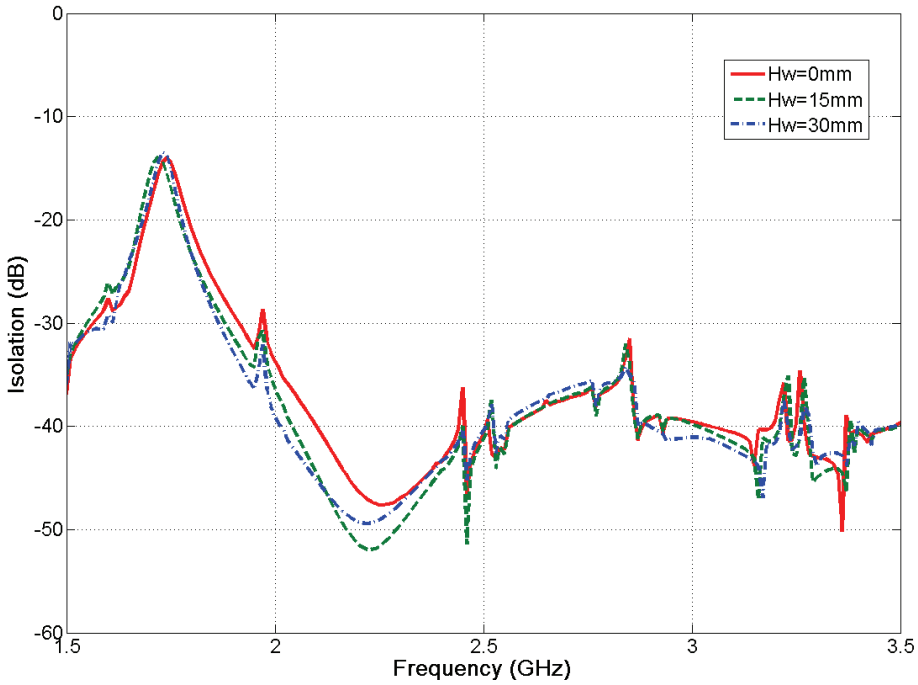

Fig. 3.16(c) Simulated isolation with different heights of side wall

3.6.2.2 Gain

Fig. 3.17 shows the simulated gain of the antenna with different H_w of the side wall at ports 1 and 2. At the center frequency of 2.5 GHz, the gain varies only about 0.6 dB when H_w is increased. The lower frequency band and the upper frequency band, however, the gain is increased by more than 1.4 dB when H_w is increased. From the simulated results, the gain can be increased when the additional metallic side wall is surrounded. The maximum gain of 11.4 dBi is obtained at 3.0 GHz for H_w = 30 mm at port 1, and the maximum gain of 11.3 dBi is achieved at 3.0 GHz for H_w = 30 mm at port 2.

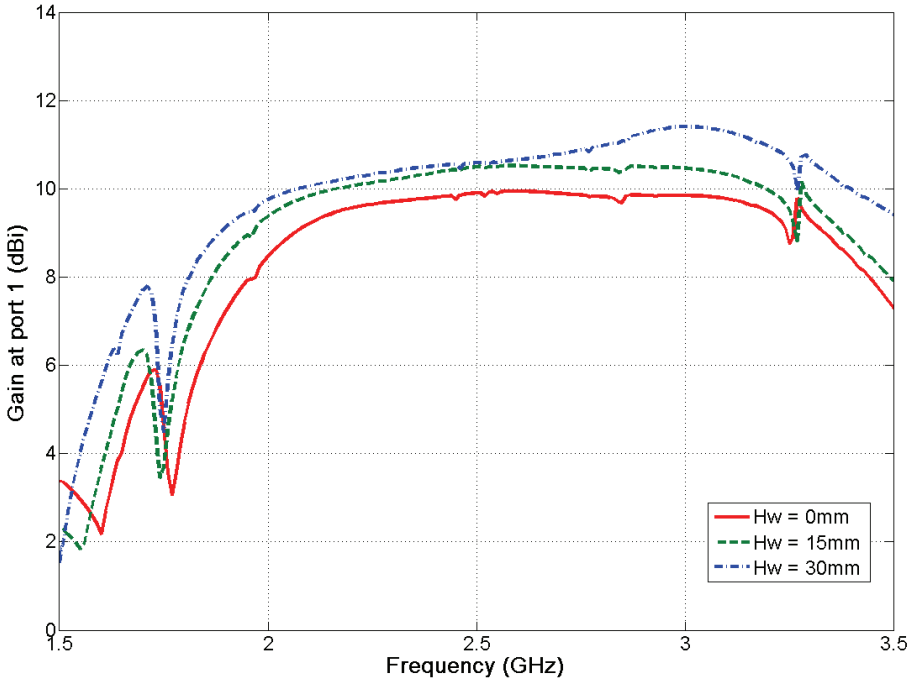

Fig. 3.17(a) Simulated gain of the antenna with different heights of side wall at port 1

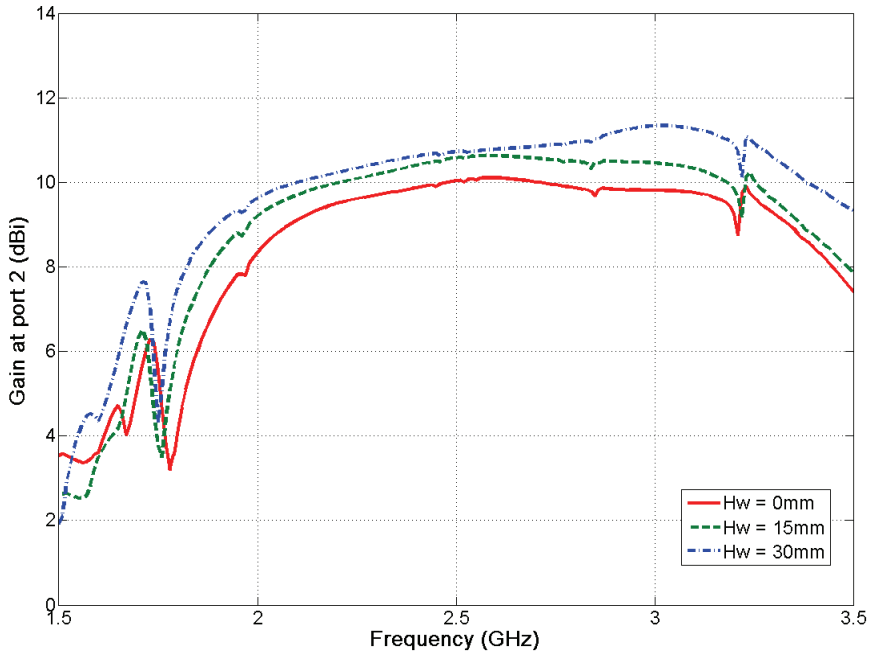

Fig. 3.17(b) Simulated gain of the antenna with different heights of side wall at port 2

3.6.2.3 Radiation pattern

Figs. 3.18 to 3.20 show the simulated radiation patterns of port 1 with different heights of the side wall at 2.1 GHz, 2.7 GHz, and 3.4 GHz, which represent the lower, center, and upper frequency, respectively. From the radiation pattern for different H_w in Fig. 3.18, the back radiation is reduced when H_w is increased. For H_w = 0 mm, the front-to-back ratio is about 14 dB at the lower frequency, but the front-to-back ratio is improved to around 20 dB when H_w = 30 mm. The cross-polarization of the radiation at lower frequency of 2.1 GHz is also slightly reduced when H_w is increased. From Figs. 3.19 and 3.20, it is observed that the back-lobe level is less than 20 dB for all the cases with different heights of the vertical side wall. The cross-polarization levels of the radiation patterns are not sensitive to the heights of the metallic side walls.

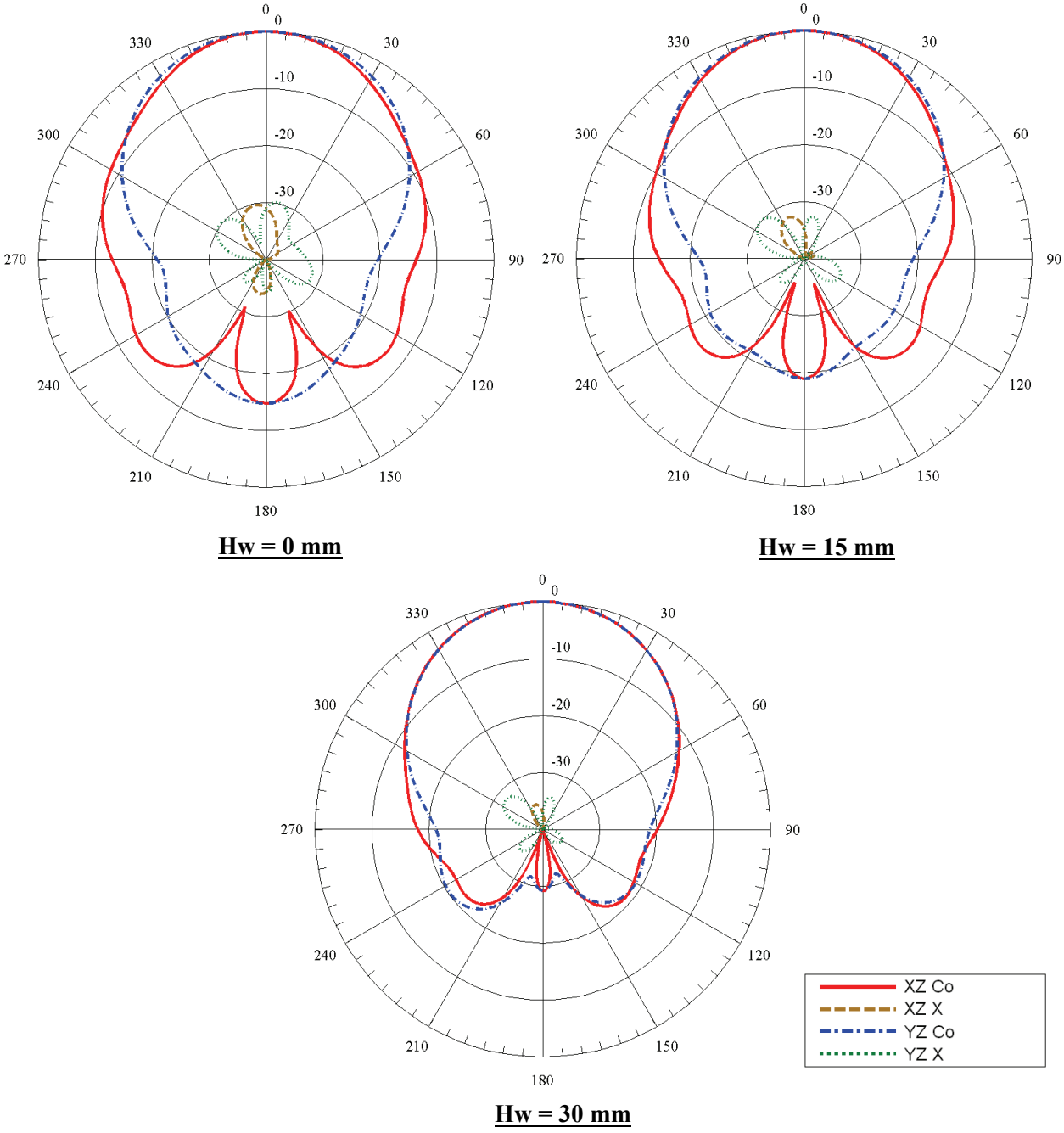

Fig. 3.18 Simulated radiation patterns of port 1 at 2.1 GHz with different values of H_w

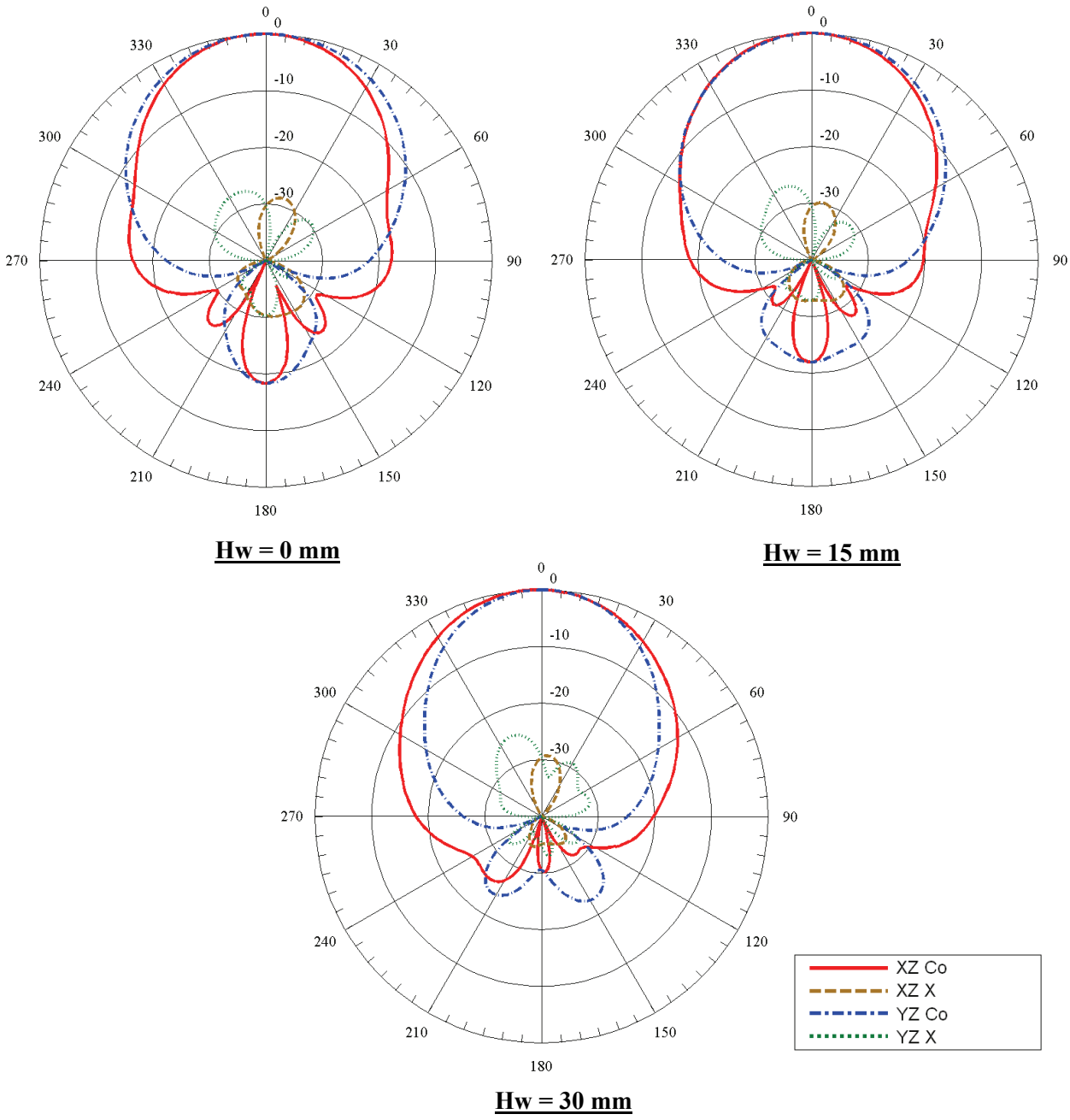

Fig. 3.19 Simulated radiation patterns of port 1 at 2.7 GHz with different values of H_w

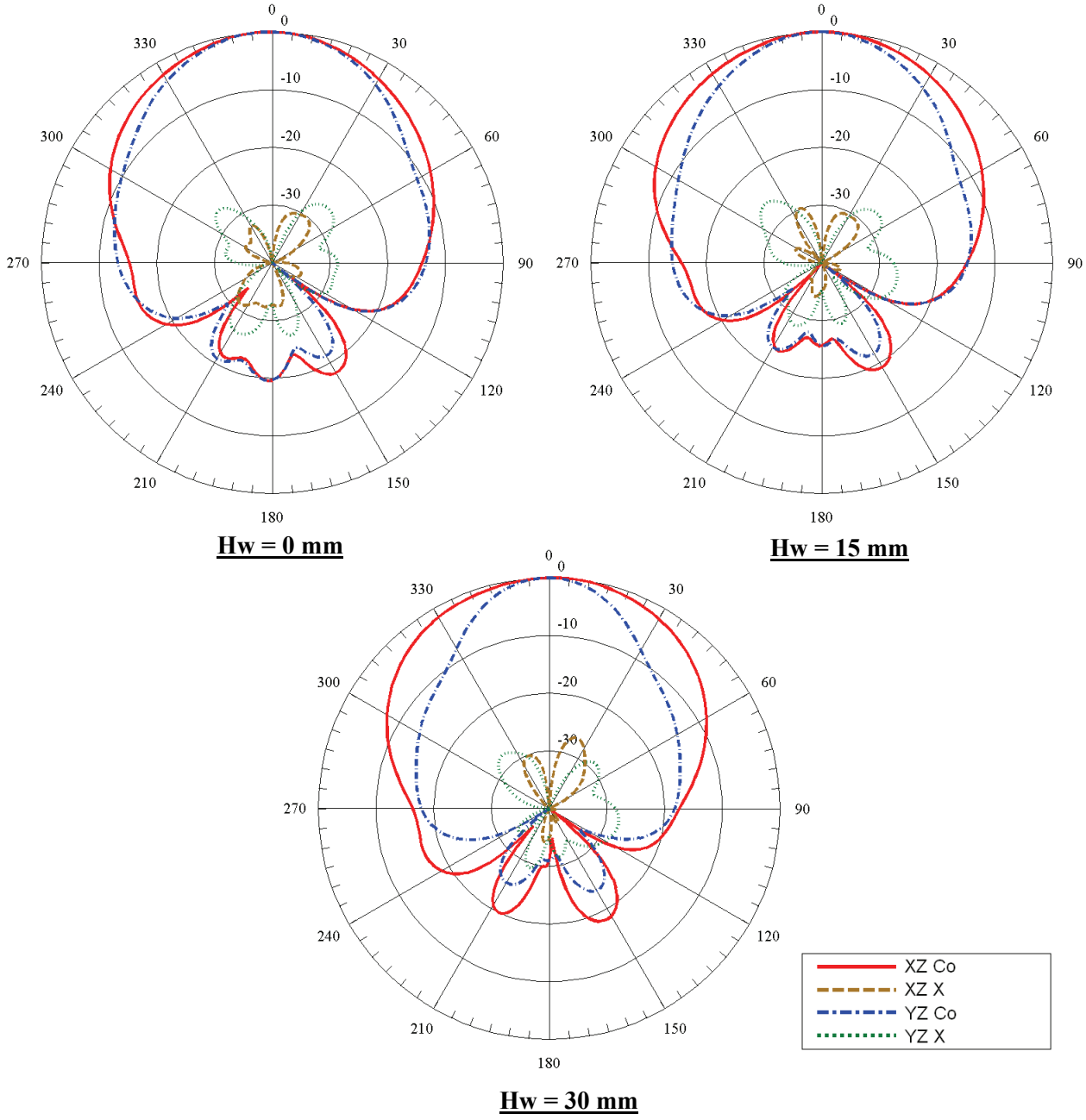

Fig. 3.20 Simulated radiation patterns of port 1 at 3.4 GHz with different values of H_w

CHAPTER IV

STUDY FOR A NOVEL DUAL-POLARIZED PATCH ANTENNA WITH EMBEDDED EBG STURCTURES

4.1 Introduction

In previous chapter, the wideband dual-polarized patch antenna, which is evolved from the linearly polarized patch antenna in chapter II by introducing second slot aperture, was analyzed and built for testing. It was shown that the wideband performance of the linearly polarized antenna is successfully retained in the case of the dually polarized antenna. In order to generate the second polarization, however, a complex geometry is required having four separated patches with four hook-shaped probes. Here, a novel dual-polarized antenna with simple structure is proposed and the performance of the antenna is examined in this chapter.

To generate the second polarization in the linearly polarized patch antenna in chapter II, a perfect magnetic conductor (PMC) wall is introduced within the geometry of the previous structure and one of the conventional methods to realize the PMC using an electromagnetic band gap (EBG) structure is adopted in the present study. Two kinds of EBG walls are modeled and analyzed in this chapter: One is a conventional mushroom-like EBG structure [49,50] and the other is a wideband planar type EBG structure from the recently introduced paper in [51]. In order to utilize the above EBG walls in our frequency range of interest at 2.5GHz, modification of the dimensions and frequency scaling are necessary and details of this procedure are demonstrated in Appendix I.

A brief idea for introducing this dual-polarization mechanism is illustrated in Fig. 4.1. The linear and dual-polarization, which are discussed in the chapters II and III, are shown in Fig. 4.1 (a) and (b), respectively. Fig. 4.1 (c) describes new approach to produce the second polarization which will be discussed in this chapter. In Fig. 4.1 (c), two monopoles with 180° anti-phased feeding network along the EBG walls are excited to generate the possible dual polarization of the antenna. Analyses of the monopole excitation as well as the unit-cell of the two different EBG surfaces will be discussed in the remainder of the chapter. Finally, the performance of the proposed antenna with embedded EBG walls such as the radiation pattern and reflection coefficients will be included in this chapter.

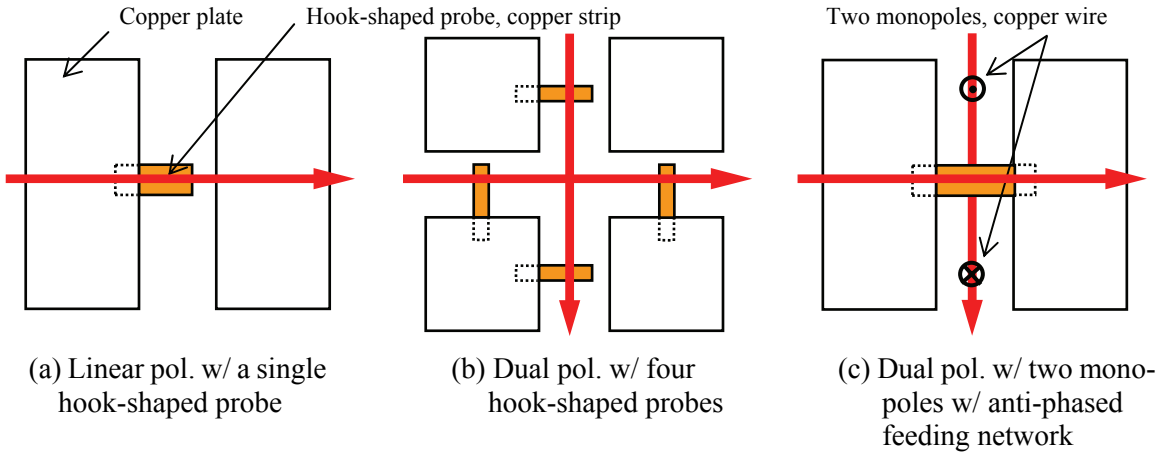

Fig. 4.1 Concept of generating a dual-polarization from the geometry of a linearly polarized structure

4.2 Antenna description

The configuration of a prototype dual-polarized patch antenna with embedded EBG structure walls is shown in Fig. 4.2. The geometry of the prototype is similar with that of

the linear polarized antenna in chapter II, but two vertical EBG structure walls along with two monopoles with anti-phased feeding network are employed for examining the possible polarization in the direction of the slot aperture. A hook-shaped probe is extended and

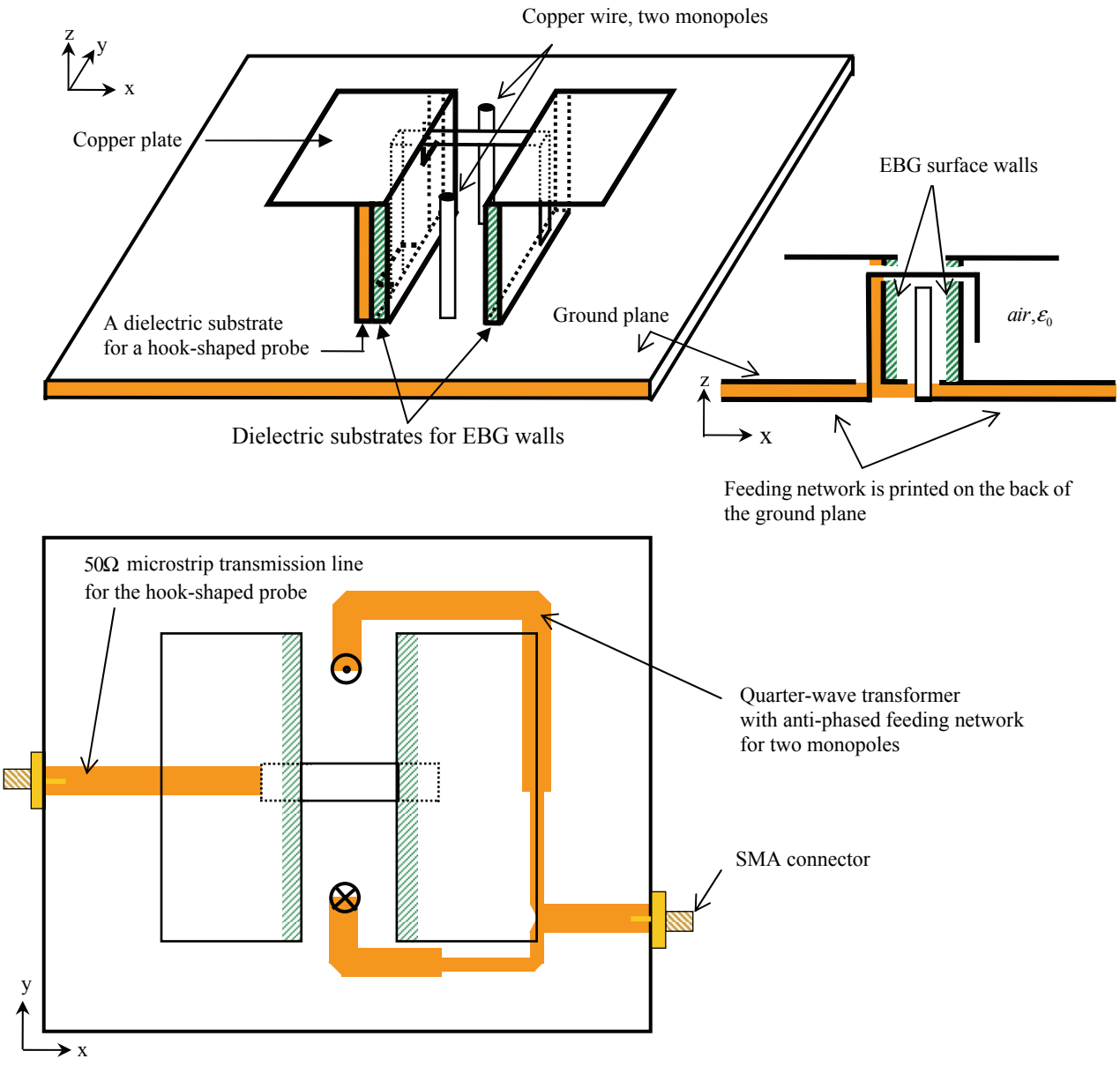

Fig. 4.2 Configuration of a prototype dual-polarized patch antenna with EBG walls

penetrates two EBG walls, and a dielectric substrate for 50 ohm microstrip transmission

line of the hook-shaped probe is stacked together with one of the EBG wall substrates.

4.3 Excitation of the proposed antenna

There are two possible excitations for generating the second polarization of the proposed antenna as described in Fig. 4.3. First, the slot excitation in Fig. 4.3 (a) was examined due to its simple implementation by placing a slot on the ground plane with a 50 ohms microstrip transmission line and an open stub. With different offset positions and lengths of the open stub, the slot excitation has a main drawback of high back-radiation, which is not desired for radiating along the slot aperture.

As shown in Fig. 4.3 (b), a configuration of two monopoles with anti-phased feeding network and nearby PMC walls is another possible excitation for having the desired uni-directional radiation pattern. An equivalent configuration to Fig. 4.3 (b) using image theory is illustrated in Figs. 4.4 (c) and 4.5.

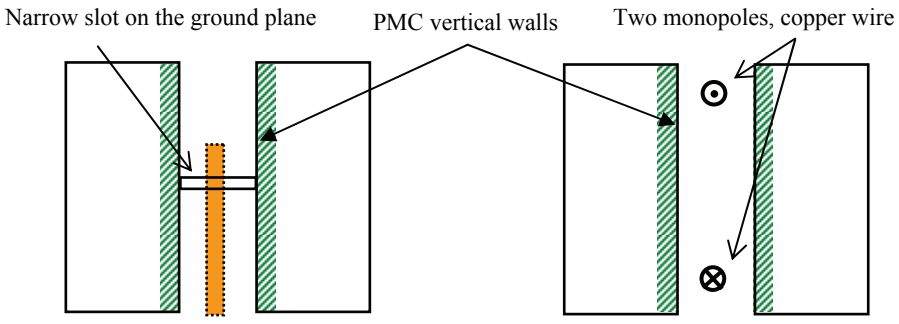

Fig. 4.3 Two possible excitations for generating unidirectional radiation pattern

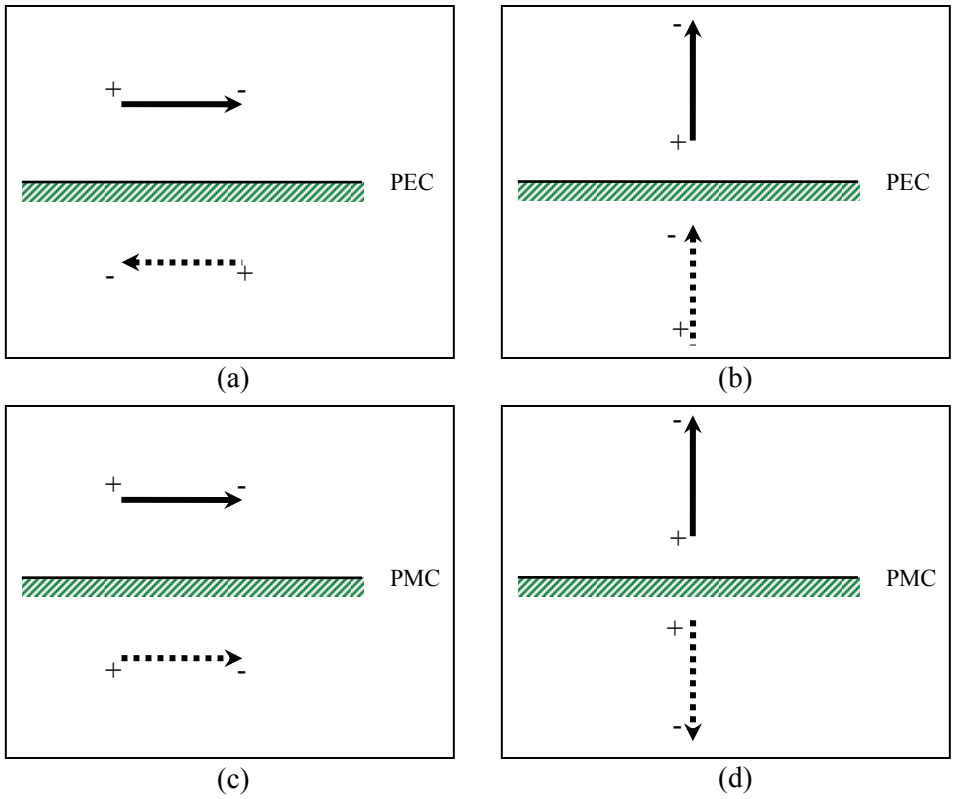

Fig. 4.4 Image of an electric monopole with different configurations of PEC/PMC walls

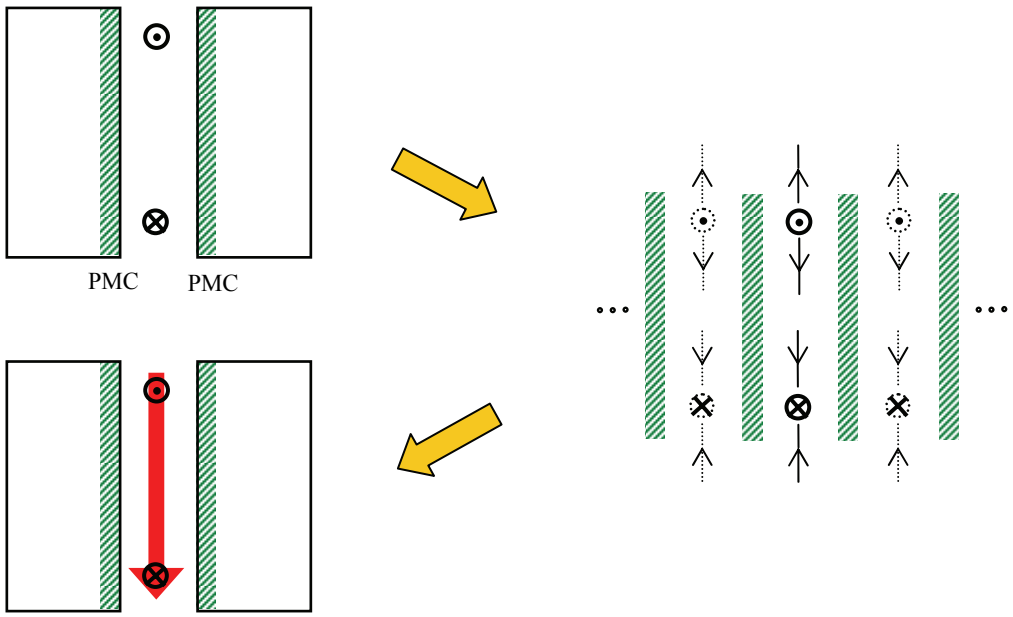

Fig. 4.5 Current distribution of two monopoles with PMC walls using the image theory

4.3.1 Simulation results

Before the EBG walls and horizontal rectangular patch wings were placed on the proposed antenna, a simulation study for two monopoles excitation was conducted using Ansoft HFSS. Different shapes and positions of the two monopoles were analyzed and two bent monopoles with radius of 0.3 mm were selected as shown in Fig. 4.6. The distance between the two monopoles is 50 mm ($0.42\lambda_o$) and the total length of the bent monopole is 30 mm ($0.25\lambda_o$). Instead of having the quarter-wave transformer on the back of the ground plane substrate, direct coaxial probes with 0^o and 180^o phase are used for exciting port 1 and port 2, respectively. Simulation results of reflection coefficient and radiation pattern at 2.5 GHz are plotted in Figs. 4.7 and 4.8, correspondingly.

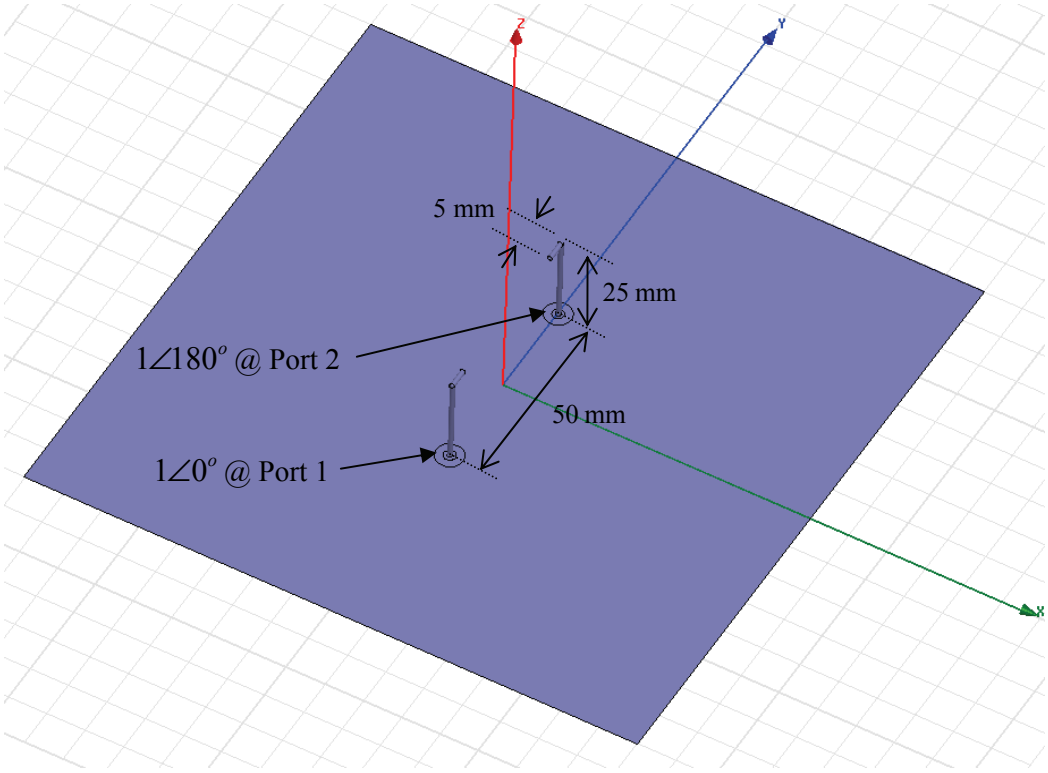

Fig. 4.6 Configuration of two bent monopoles without presence of PMC walls

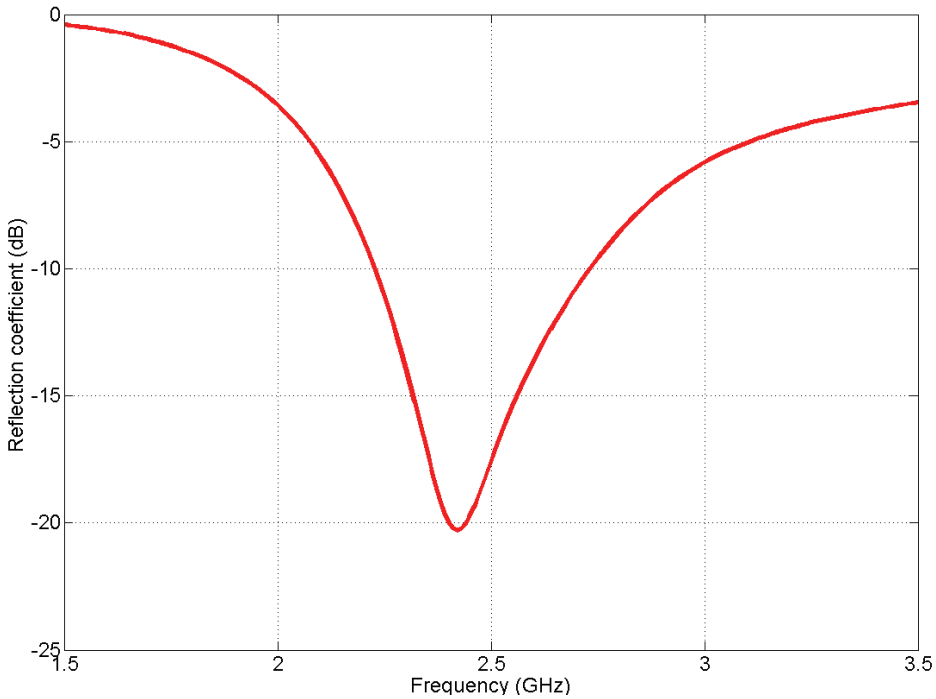

Fig. 4.7 Simulated reflection coefficient for two bent monopoles at port 1

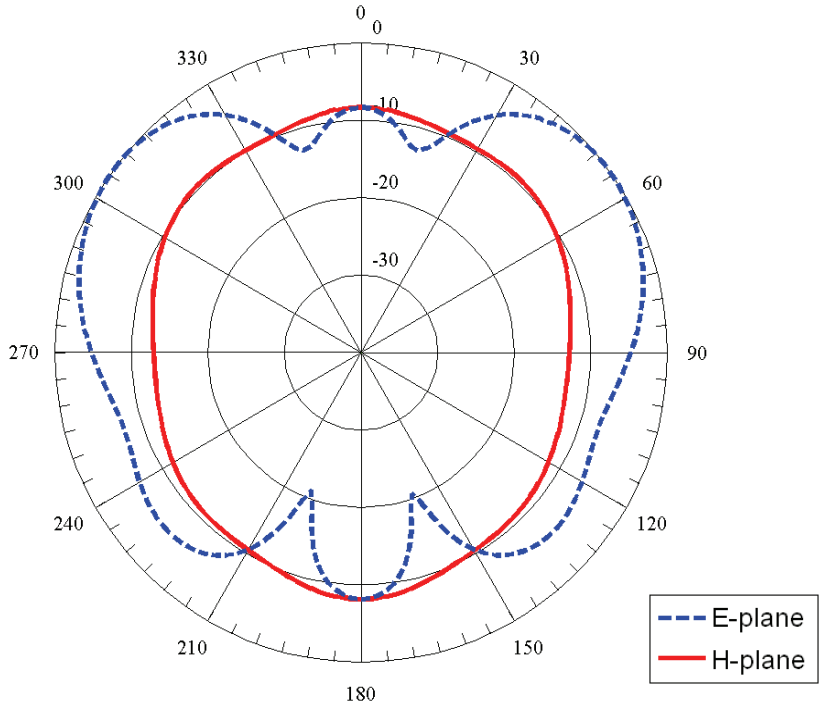

Fig. 4.8 Simulated radiation pattern for two bent monopoles at 2.5 GHz

4.4 EBG structure characterization

The characteristics of the EBG structures are studied using the Ansoft HFSS. Conventional methods to analyze the unit-cell of the EBG structure are either an in-phase reflection coefficient for plane wave incidence or a surface wave band gap by $k-\beta$ dispersion diagram of the infinite arrays. In our study, the $k-\beta$ dispersion diagrams of two different EBG structures are simulated to find frequency band gaps. Due to the only $0.11\lambda_o$ distance between two EBG walls in our configuration, the coupling effect between these walls has to be included in the analysis setup.

4.4.1 Mushroom-like EBG structure

The geometry of the mushroom-like EBG structure as shown in Fig. 4.9 is placed 2.54 mm above a PEC ground plane, while the substrate is filled by RT/Duroid 6002 with dielectric constant of 10.2. The unit-cell size of the EBG surface is w = 9.0 mm and the gap between two unit-cells is 0.2 mm. The EBG surface and the PEC ground plane are connected through vias with radius of 0.3 mm.

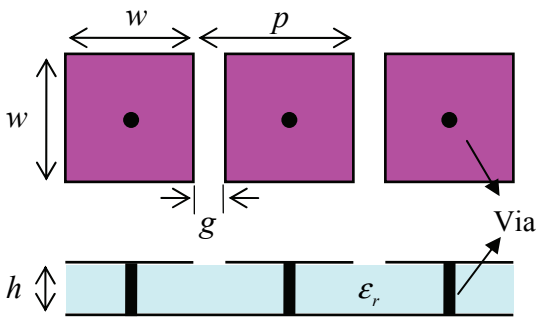

- Dielectric Constant (ε_r) = 10.2
- Substrate Thickness (h) : 2.54 mm
- Radius of the via : 0.3 mm
- Dimensions

p	w	g
9.2	9.0	0.2

mm

Fig. 4.9 Geometry of the mushroom-like EBG structure

4.4.1.1 Simulation setup

The simulation setups for the unit-cell of the mushroom-like EBG structure in HFSS with two different configurations are illustrated in Fig. 4.10. The conventional method to analyze the dispersion diagram of the EBG surface consists of three main parts: an EBG geometry, a periodic boundary condition (B.C.) region, and a perfectly matched layer (PML) as shown in Fig. 4.10 (a). The upper part of the setup has the perfectly matched layer which can absorb any reflections toward the top and the bottom part of the configuration has a metallic PEC ground plane as a part of the mushroom-like EBG

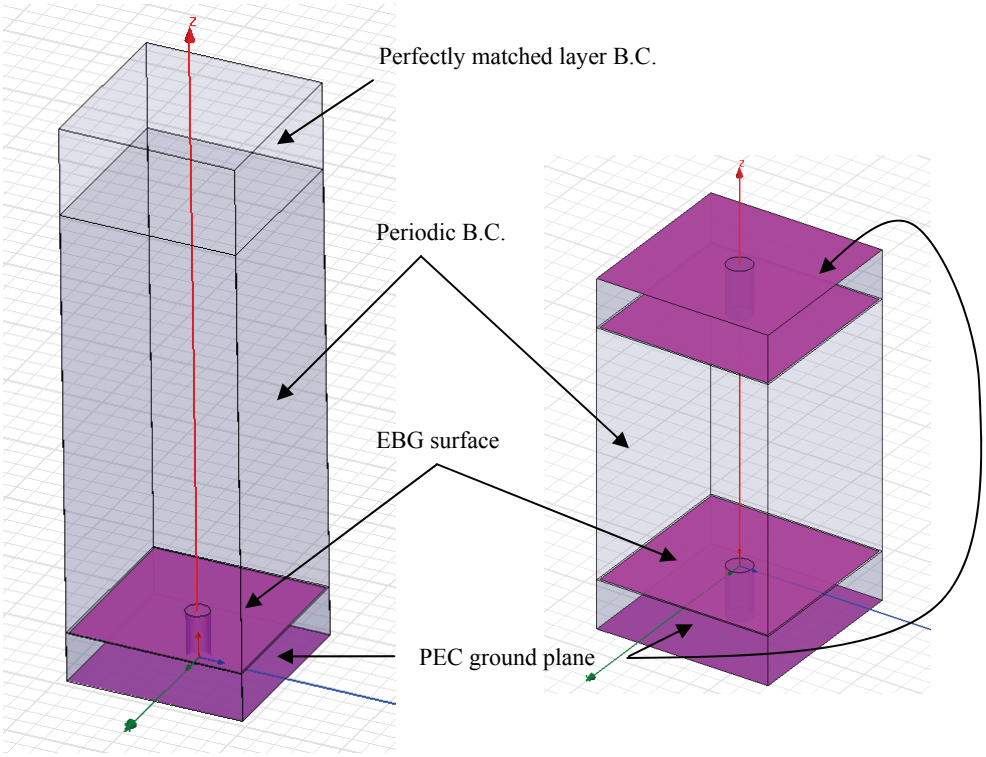

(a) Conventional method (b) Two layers method

Fig. 4.10 Two different simulation setups for a unit-cell of the mushroom-like EBG

structure. From the top of the PML to the bottom end, the periodic B.C. is assigned to the surrounding faces of the simulation setup for implementing an infinite array configuration from the unit-cell.

Under our configuration in Fig. 4. 10 (b), however, the PML B.C. is not needed to the simulation setup, and only the periodic B.C. for two closed EBG walls is required. The actual distance, S = 13 mm ($0.11\lambda_o$), between two EBG walls is used for the simulation. Such a configuration seems more reasonable to analyze the interaction between two EBG walls and can allow us to examine the effect of them more accurately.

4.4.1.2 Simulation results

Figs. 4.11 (a) and (b) show the dispersion diagram of the mushroom-like EBG structure on the conventional method and the two layers method, respectively. A complete stopband is observed for both cases, but a much narrower bandgap exists for the two layers case. For the conventional method, the bandgap is centered at 2.56 GHz and spans the frequency range from 2.27 GHz to 2.85 GHz (22.7%); whereas for the two layers case, the bandgap bandwidth of 7.0% was achieved from 2.22 GHz to 2.38 GHz with center frequency at 2.3 GHz. Detail views of the $\Gamma - X$ branch of the Brillouin Zone (BZ) for both cases are plotted in Fig. 4.12.

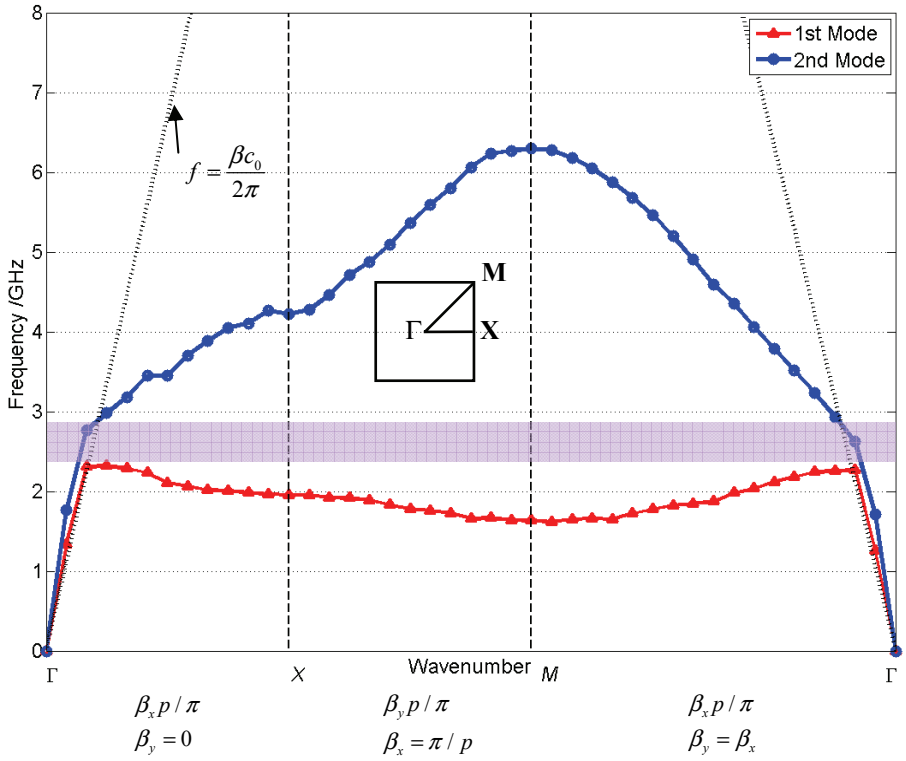

Fig. 4.11(a) Simulated dispersion diagram for mushroom-like EBG structure using conventional method

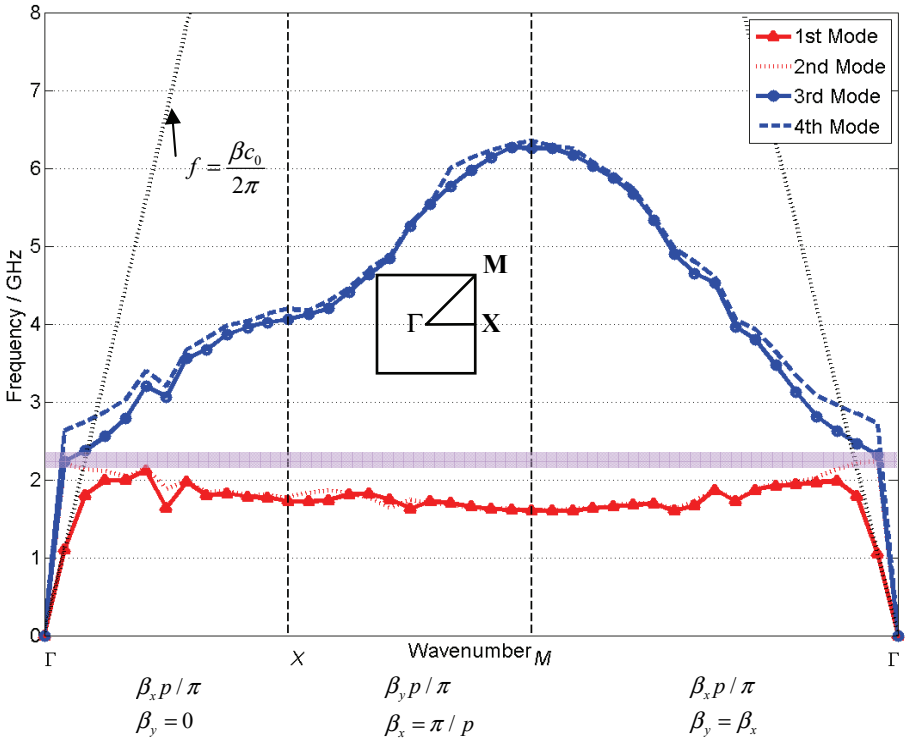

Fig. 4.11(b) Simulated dispersion diagram for mushroom-like EBG structure using two layers method

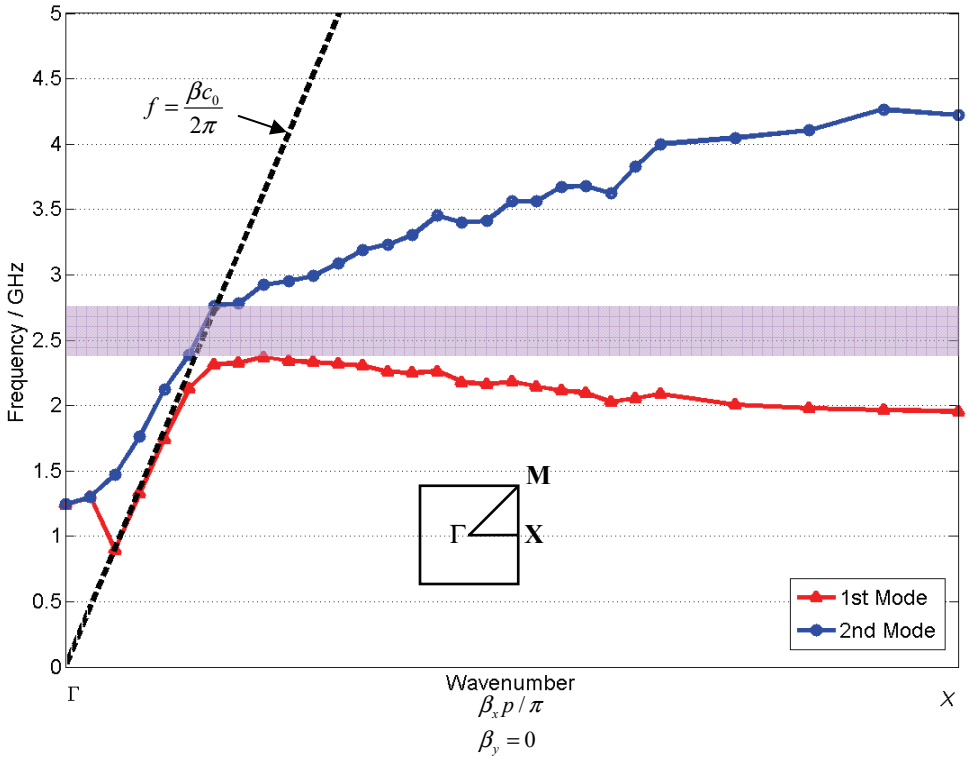

Fig. 4.12(a) Detail view of $\Gamma - X$ branch of the dispersion diagram for mushroom-like EBG structure using conventional method

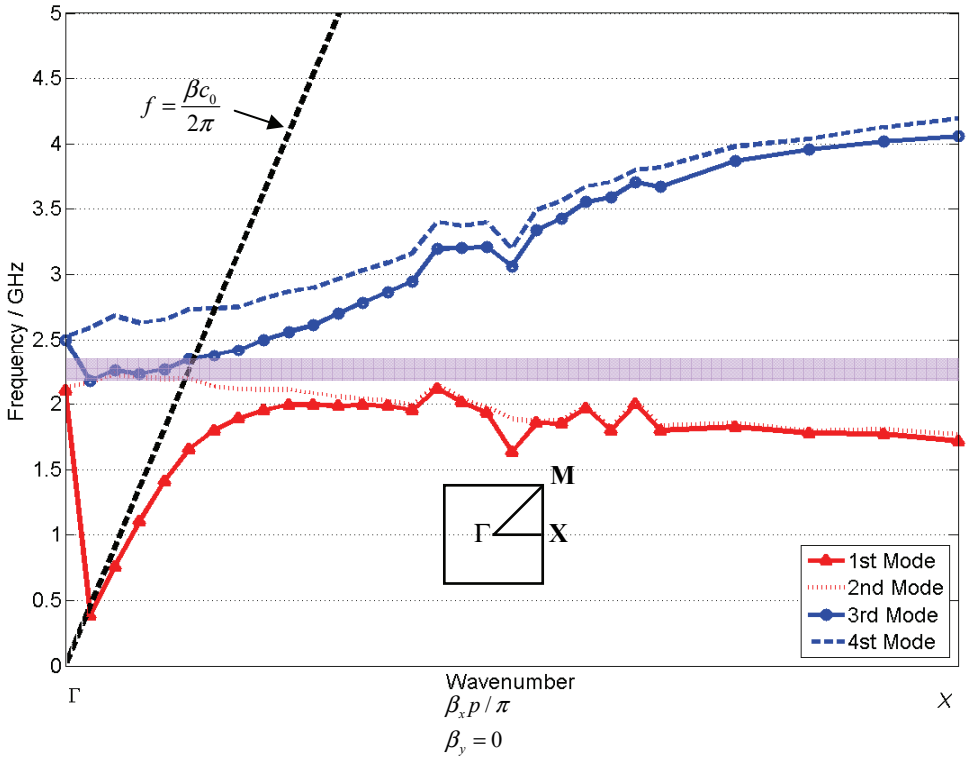

Fig. 4.12(b) Detail view of $\Gamma - X$ branch of the dispersion diagram for mushroom-like EBG structure using two layers method

4.4.2 Wideband uniplanar EBG structure

The top view of the wideband uniplanar EBG structure as proposed in [51] is shown in Fig. 4.13. The dark area denotes the presence of PEC materials. The metallic surface is placed 0.8 mm above a PEC ground plane, while the substrate is filled by RT/Duroid 6002 with dielectric constant of 10.2. The unit-cell size of the EBG structure is p = 11.2 mm.

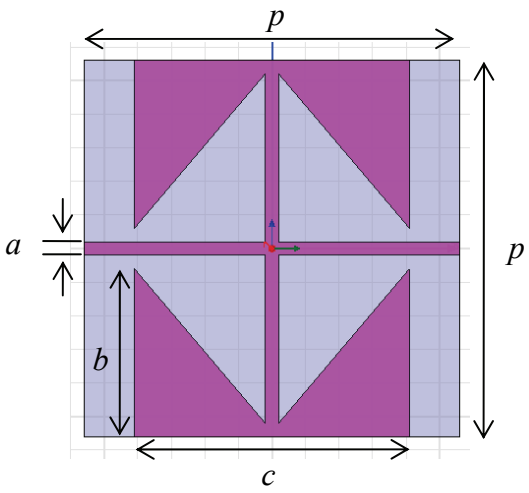

- Dielectric Constant (ε_r) = 10.2
- Substrate Thickness : 0.8 mm
- Dimensions

p	*a*	*b*	*c*
11.2	0.4	5	7.6

mm

Fig. 4.13 Geometry of the wideband uniplanar EBG structure

4.4.2.1 Simulation setup

The simulation setups for the unit-cell of the wideband uniplanar EBG structure in HFSS with two different configurations are described in Fig. 4.14. The simulation setups are similar to those for the mushroom-like EBG structure in section 4.4.1.1.

4.4.2.2 Simulation results

Figs. 4.15 (a) and (b) show the dispersion diagram of the wideband uniplanar EBG

structure on the conventional method and two layers method, respectively. For the details of the $\Gamma - X$ branch of the Brillouin Zone (BZ), where the stop or go bandgap can be determined, more points within the $\Gamma - X$ region are simulated, as shown in Fig. 4. 16. A complete stopband exists for the conventional case and the bandgap is 63.8 % with center frequency at 2.40 GHz and frequency range from 1.63 GHz to 3.16 GHz. Under the two layers simulation setup, however, the 3rd mode in the $\Gamma - X$ and $M - \Gamma$ regions of the Brillouin Zone (BZ) is inside the light mode. This means that surface waves are propagated and no stopband around the frequency at 2.5 GHz exists under our configuration even though an open-spaced EBG structure itself has a certain stopband.

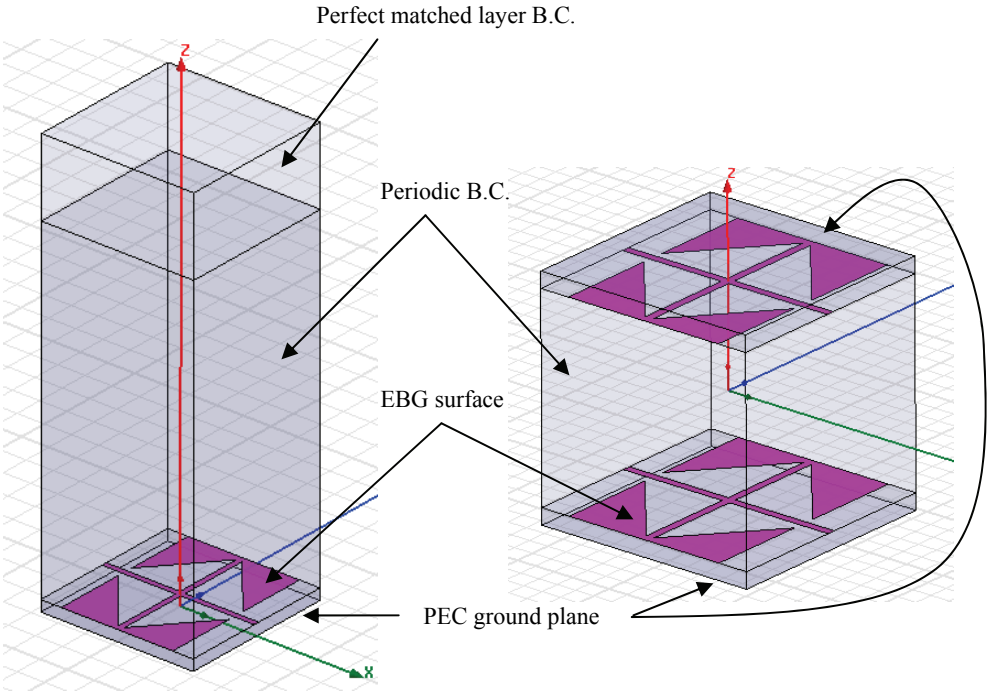

(a) Conventional method (b) Two layers method

Fig. 4.14 Two different simulation setups for a unit-cell of the wideband uniplanar EBG

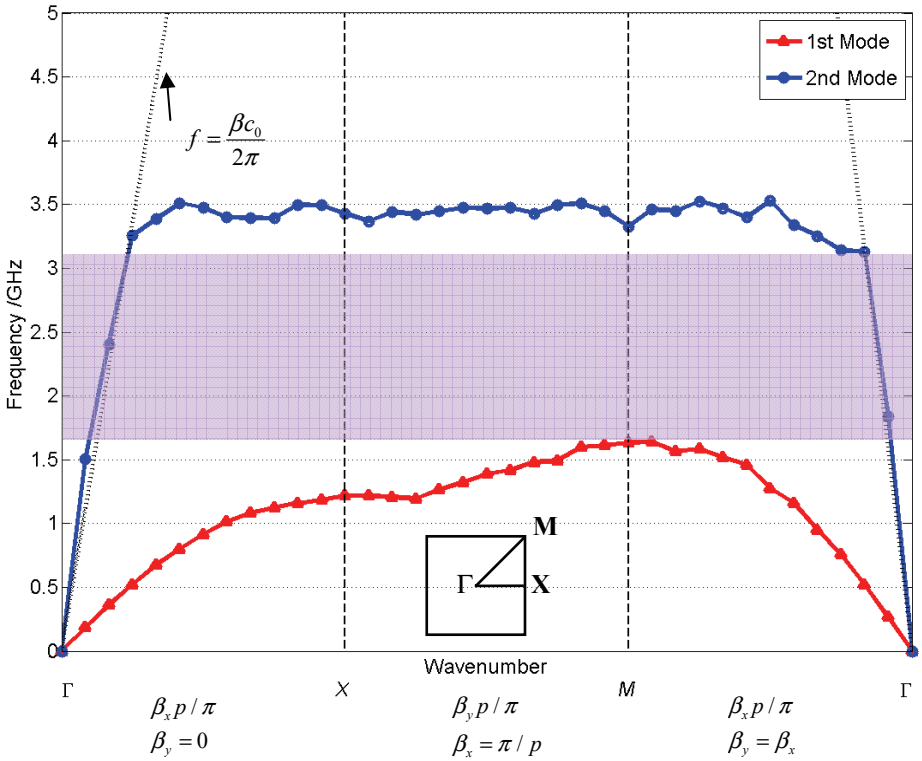

Fig. 4.15(a) Simulated dispersion diagram for wideband uniplanar EBG structure using conventional method

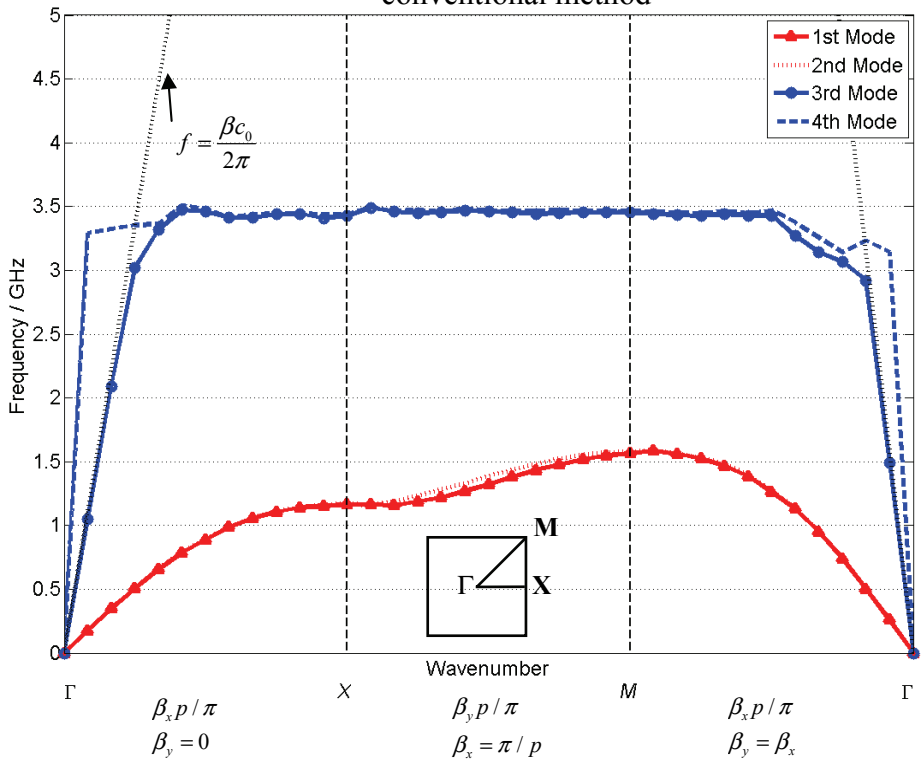

Fig. 4.15(b) Simulated dispersion diagram for wideband uniplanar EBG structure using two layers method

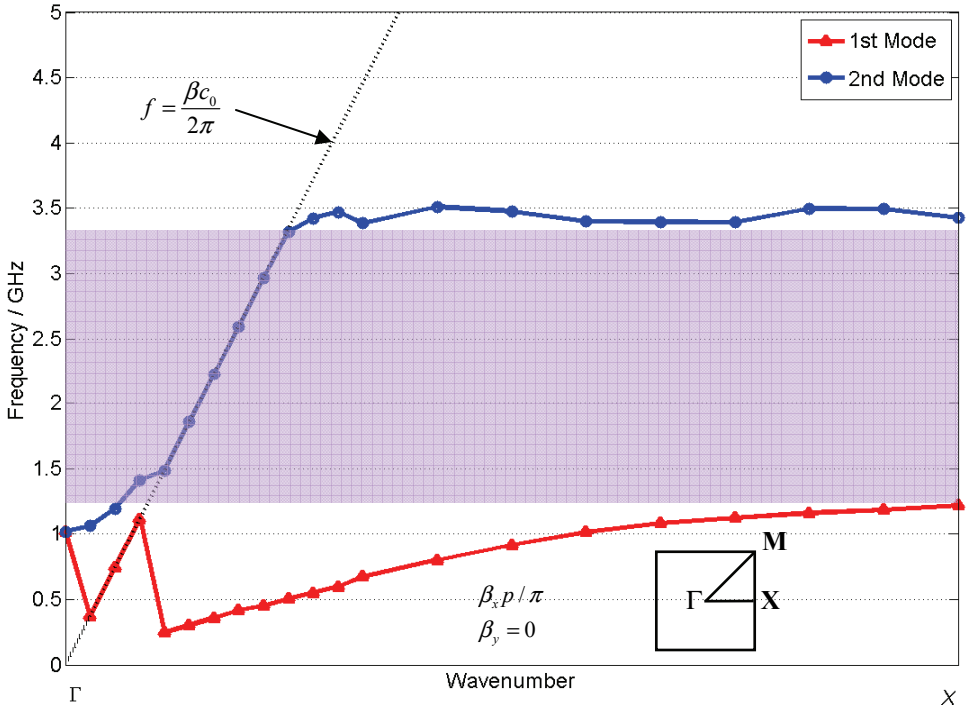

Fig. 4.16(a) Detail view of $\Gamma - X$ branch of the dispersion diagram for wideband uniplanar EBG structure using conventional method

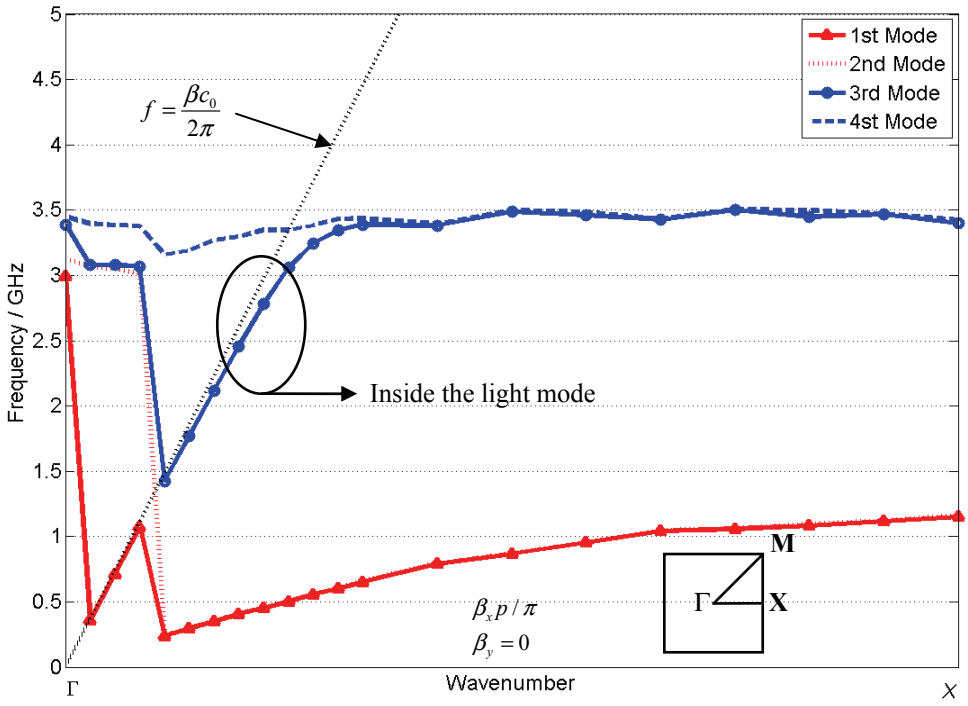

Fig. 4.16(b) Detail view of $\Gamma - X$ branch of the dispersion diagram for wideband uniplanar EBG structure using two layers method

4.5 Performance of the proposed antenna

Characteristics of the two monopoles with two different embedded EBG structures, which were analyzed by dispersion diagram of the unit-cells for different simulation setups in section 4.4, are examined using Ansoft HFSS. The effects of the different kinds of walls on the performance of the proposed antenna and comparison among them are discussed in this section.

4.5.1 Mushroom-like EBG case

The configuration of two monopoles with the mushroom-like EBG walls is illustrated in Fig. 4.17. The EBG wall consists of 3 by 6 unit-cells of the mushroom-like EBG structure. The distance between these two walls is S = 13 mm ($0.11\lambda_o$) and the dimension for the rectangular vertical substrate wall is 30 mm by 60 mm. Each via of the top metallic surface is connected to the back of the vertical ground plane.

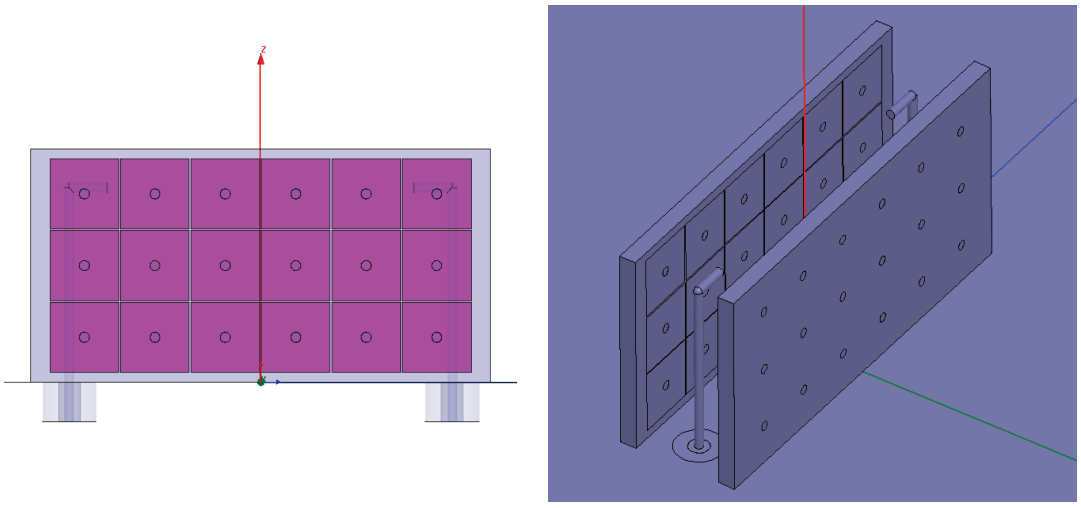

Fig. 4.17 Configuration of two monopoles with the mushroom-like EBG walls

The reflection coefficient of the proposed antenna for different values of *S* is plotted in Fig. 4.18. Due to the narrow stopband frequency of the unit-cell from 2.22 GHz to 2.38 GHz, the EBG walls don't act as PMC walls shown in Fig. 4. 18. The electric field distribution along the aperture width is depicted in Fig. 4.19. In order to compare the effect of the EBG walls, realized gain patterns are plotted instead of radiation patterns, as shown in Fig. 4. 20. The gain at broadside is improved by 8dB and the grating lobes near broadside are improved correspondingly. However the realized gain patterns deteriorate quickly when the frequencies are swept.

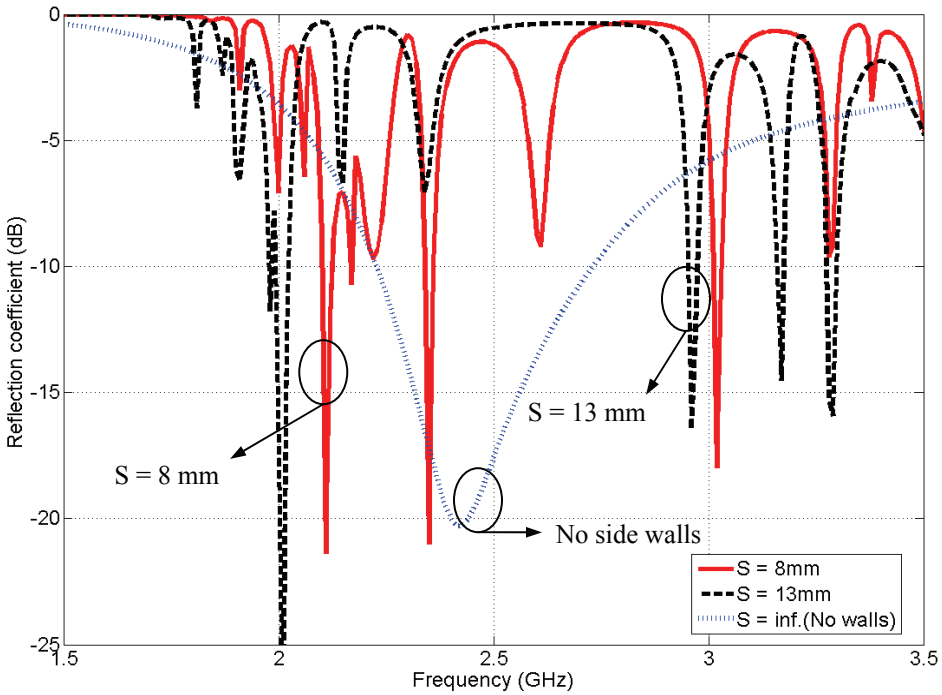

Fig. 4.18 Reflection coefficient of two monopoles with the mushroom-like EBG walls for different values of *S*

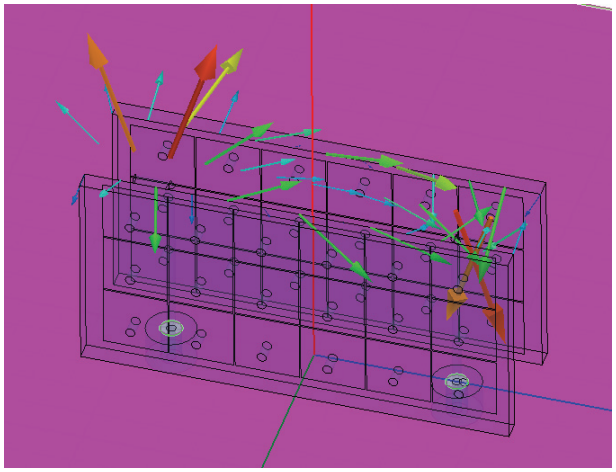

Fig. 4.19 Electric field distribution along the aperture of the proposed antenna

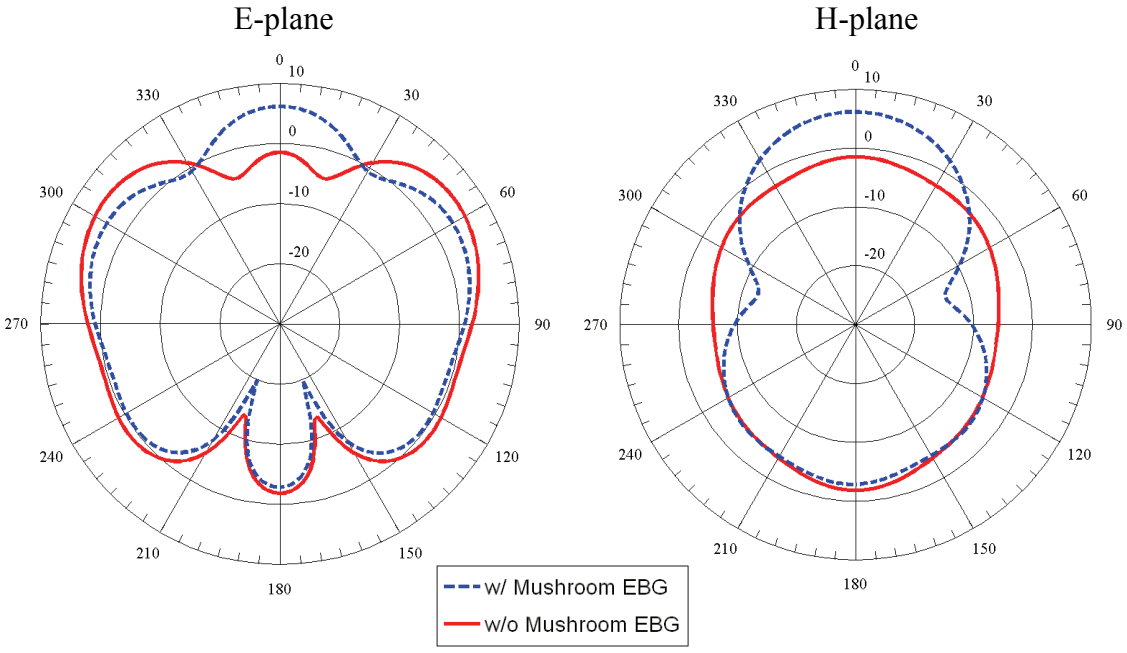

Fig. 4.20 Realized gain pattern of two monopoles with the mushroom-like EBG walls at 2.43 GHz

4.5.2 Wideband uniplanar EBG case

The configuration of two monopoles with the wideband uniplanar EBG walls is illustrated in Fig. 4.21. The EBG wall consists of 3 by 5 unit-cells of the wideband uniplanar EBG structure. The distance between these two walls is $S = 13$ mm ($0.11\lambda_o$) and the dimension for the rectangular vertical substrate wall is 35 mm by 60 mm, which is slightly larger than that of the mushroom-like EBG structure.

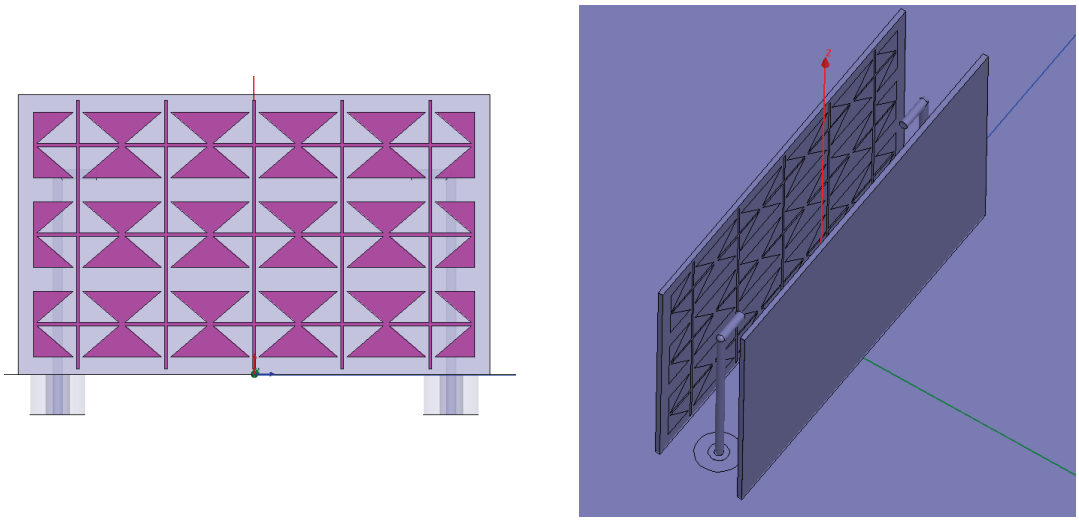

Fig. 4.21 Configuration of two monopoles with the wideband uniplanar EBG walls

The reflection coefficient of the proposed antenna for different cases is plotted in Fig. 4.22. Based on the simulation results under two layers analysis, where no stopband exists at the frequency of 2.5 GHz, the behavior of the reflection coefficient for the wideband uniplanar EBG walls is similar to that for the PEC walls. The realized gain patterns for both E- and H-planes are less than -10dB, and no radiation is observed in this case as plotted in Fig. 4.23.

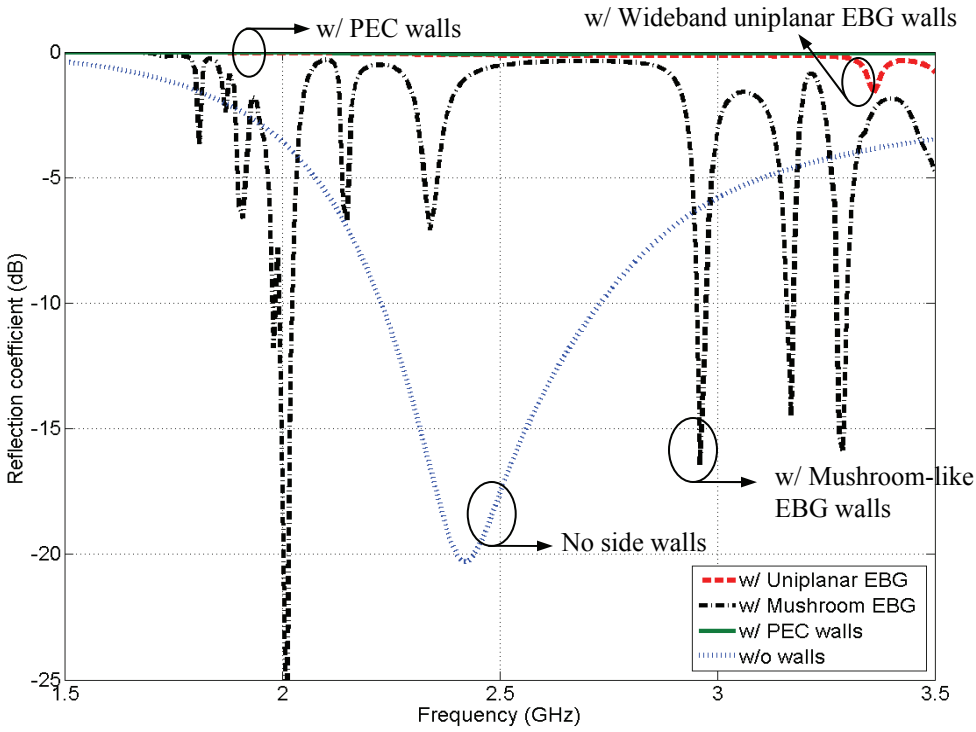

Fig. 4.22 Reflection coefficients of two monopoles with the mushroom-like and the wideband uniplanar EBG walls

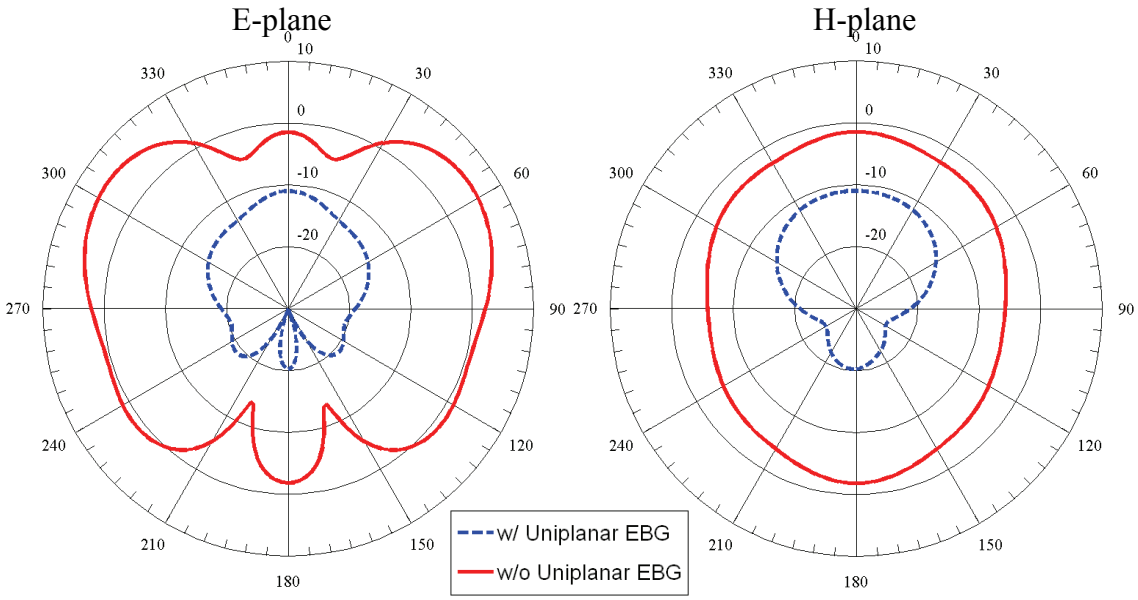

Fig. 4.23 Realized gain pattern of two monopoles with the wideband planar EBG walls at 2.43 GHz

CHAPTER V

SUMMARY AND FUTURE WORK

5.1 Summary

This study was aimed at studying of a wideband dual-polarized patch antenna, which has excellent characteristics such as symmetric E- and H-plane radiation pattern, low cross-polarization and stable gain over the operating frequency at 2.5GHz. The first part of this study dealt with the design of a wideband linearly polarized patch antenna. To increase the bandwidth of the antenna, the dielectric substrate was shielded from the radiating region and twin hook-shaped probe feeds were implemented. Intensive parametric study of the proposed antenna was discussed. The second part of this study dealt with designing a wideband dual-polarized patch antenna. Its performance was evaluated using Ansoft HFSS, a full-wave finite element method simulator. The antenna was then fabricated and its performance was measured. The last part of this study illustrated a possible candidate for a novel dual-polarized patch antenna with an embedded EBG structure. Unit-cells of the mushroom-like EBG structure and wideband uniplanar EBG structures are examined by two different simulation setups for analyzing the dispersion diagram.

5.2 Future work

In chapter III, the dual-polarized antenna is excited by twin hook-shaped probes with an in-phase feeding network on a vertical substrate. In the application where very low cross-polarization level is required, the cross-polarization level can be improved by

employing an anti-phased feeding network. In order to employ this feeding network within the proposed antenna, the feeding network should be printed on the back of the ground plane substrate, and such a configuration might improve the isolation of the antenna, especially at the lower frequencies of the operating band because the interference of the openings at bottom side of the vertical ground planes, where the microstrip line cross the orthogonal ground plane, can be minimized.

BIBLIOGRAPHY

[1] S. Dey, P. Venugopalan, K. A. Jose, C. K. Aanandan, P. Mohanan and K. G. Nair, "Bandwidth enhancement by flared microstrip dipole antenna," *IEEE Antennas Propag. Society Int. Symp.*, vol. 1, pp. 342-345, Jun. 1991.

[2] Y. D. Lin and S. N. Tsai, "Coplanar waveguide fed uniplanar bow-tie antennas", *IEEE Trans. Antennas Propag.*, vol. 45, no. 2, pp. 305-306, Feb. 1997.

[3] E. Levine, S. Shtrikman and D. Treves, "Double-sided printed arrays with large bandwidth," *IEE Proc. Microw. Antennas and Propag.*, vol. 135, pp. 54-59, Feb. 1988.

[4] K. M. Luk, C. L. Mak, Y. L. Chow and K. F. Lee, "Broadband microstrip patch antenna," *Electron. Lett.*, vol. 34, pp. 1442-1443, Jul. 1998.

[5] C. L. Mak, K. M. Luk, K. F. Lee and Y. L. Chow, "Experimental study of a microstip patch antenna with an L-shaped probe," *IEEE Trans. on Antennas and Propag.*, vol. 48, no. 5, pp. 777-783, May 2000.

[6] Y. X. Guo, C. L. Mark, K. M. Luk, and K. F. Lee, "Analysis and design of L-probe proximity fed-patch antennas," *IEEE Trans. Antennas Propag.*, vol. 49, no. 2, pp. 145-149, Feb. 2001.

[7] H. Wong, K. L. Lau and K. M. Luk, "Design of dual-polarized L-probe patch antenna arrays with high isolation," *IEEE Trans. Antennas and Propag.*, vol. 52, no.1, pp. 45-52, Jan. 2004.

[8] H. Wong and K. M. Luk, "A low-cost L-probe patch antenna array," *Microw. Opt. Technol. Lett.*, vol. 29, no. 4, pp. 280-282, May 2001.

[9] F. Crog and D. M. Pozar, "Millimeter wave design of wide-band aperture-coupled

stacked microstrip antennas," *IEEE Trans. Antennas Propag.*, vol. 39, no. 12, pp. 1770-1776, Dec. 1991.

[10] V. Rathi, G. Kumar and K. P. Ray, "Improved coupling for aperture coupled microstrip antennas," *IEEE Trans. Antennas Propag.*, vol. 44, no. 8, pp. 1196-1198, Aug. 1996.

[11] P. Sullivan and D. Schaubert, "Analysis of an aperture coupled microstrip antenna," *IEEE Trans. Antennas Propag.*, vol. 34, no. 8, pp. 977-984, Aug. 1986.

[12] R. B. Waterhouse, "Design of probe-fed stacked patches," *IEEE Trans. Antennas Propag*., vol. 47, no. 12, pp. 1780-1784, Nov. 1999.

[13] R. Q. Lee and K. F. Lee, "Experimental study of the two-layer electromagnetically coupled rectangular patch antenna," *IEEE Trans. Antennas Propag.*, vol. 38, no. 8, pp. 1298-1302, Aug. 1990.

[14] T. M. Au and K. M. Luk, "Effect of parasitic element on the characteristics of microstip antennas," *IEEE Trans. Antennas Propag.*, vol. 39, no. 8, pp. 1247-1251, Aug. 1991.

[15] H. Legay and L. Shafai, "New stacked microstrip antenna with large bandwidth and high gain," *IEE Proc. Microw. Antennas Propag.*, vol. 141, no. 3, pp. 199-204, Jun. 1994.

[16] R. B. Waterhouse, "Design and scan performance of large, probe-fed stacked microstrip patch array," *IEEE Trans. Antennas Propag.*, vol. 50, no. 6, pp. 893-895, Jun. 2002.

[17] K. F. Lee, K. M. Luk, K. F. Tong, S. M. Shum, T. Huynh and R. Q. Lee, "Experimental and simulation studies of the coaxially fed U-slot rectangular patch

antenna," *IEE Proc. Microw. Antennas Propag.*, vol. 144, no. 5, pp. 354-358, Oct. 1997.

[18] T. Huynh and K. F. Lee, "Single-layer single-patch wideband microstrip antenna," *Electron. Lett.*, vol. 31, no. 16, pp. 1310-1312, Aug. 1995.

[19] K. F. Lee, K. M. Luk, K. F. Tong, Y. L. Yung and T. Huynh, "Experimental study of a two-element array of U-slot patches," *Electron. Lett.*, vol. 32, no. 5, pp. 418-420, Feb. 1996.

[20] M. Clenet and L. Shafai, "Multiple resonances and polarization of U-slot patch antenna," *Electron. Lett.*, vol. 35, no. 2, pp. 101-103, Jan. 1999.

[21] K. F. Tong, K. M. Luk, K. F. Lee and R. Q. Lee, "A broad-band U-slot rectangular patch antenna on a microwave substrate," *IEEE Trans. Antennas Propag.*, vol. 48, no. 6, pp. 954-960, Jun. 2000.

[22] Y. X. Guo, K. M. Luk, K. F. Lee and Y. L. Chow, "Double U-slot rectangular patch antenna," *Electron. Lett.*, vol. 34, no. 19, pp. 1805-1806, Sep. 1998.

[23] A. Petosa, A. Ittipiboon and N. Gagnon, "Suppression of unwanted probe radiation in wideband probe-fed microstrip patches," *Electron. Lett.*, vol. 35, no. 5, pp. 355-357, Mar. 1999.

[24] C. L. Mak, H. Wong and K. M. Luk, "High-gain and wide-band single-layer patch antenna for wireless communications," *IEEE Trans. Veh. Technol.*, vol. 54, no. 1, pp. 33-40, Jan. 2005.

[25] H. W. Lai and K. M. Luk, "Design and study of wide-band patch antenna fed by meandering probe," *IEEE Trans. Antennas Propag.*, vol. 54, no. 2, Feb. 2006.

[26] H. W. Lai and K. M. Luk, "Wideband patch antenna with low cross-polarisation,"

Electron. Lett., vol. 40, no. 3, pp. 159-160, Feb. 2004.

[27] P. Li, H. W. Lai, K. M. Luk and K. L. Lau, "A wideband patch antenna with cross-polarization suppression," *IEEE Antennas Wireless Propag. Lett.*, vol. 3, pp. 211-214, 2004.

[28] H. W. Lai and K. M. Luk, "Wideband stacked patch antenna fed by a meandering probe," *Electron. Lett.*, vol. 41, no. 6, pp. 297-298, 2005.

[29] H. W. Lai and K. M. Luk, "Wideband patch antenna fed by a modified L-shaped probe," *Microw. Opt. Technol. Lett.*, vol. 48, no. 5, pp. 977-979, May 2006.

[30] A. Clavin, "A new antenna feed having equal E- and H-plane patterns," *IRE Trans. Antennas Propag.*, vol. 2, pp. 113-119, 1954.

[31] A. Clavin, D. Huebner and F. Kilburg, "An improved element for use in array antennas," *IEEE Trans. Antennas Propag.*, vol. 22, no. 4, pp. 521-526. Jul. 1974.

[32] R. King and G. Owyang, "The slot antenna with coupled dipoles," *IRE Trans. Antennas Propag.*, vol. 8, no. 2, pp. 136-143, Mar. 1960.

[33] W. W. Black and A. Clavin, "Dipole augmented slot radiating element," U.S. Patent 3 594 806, Jul. 20, 1971.

[34] W. F. Gabriel and L. R. Dod, "A complementary slot-dipole antenna for hemispherical coverage," NASA-Goddard Space Flight Center, Greenbelt, MD, NASA TN X-55681, Oct. 1966.

[35] E. J. Wilkinson, "Circularly polarized slot antenna," U.S. Patent 2 972 147, Feb. 14, 1961.

[36] K. M. Luk and H. Wong, "A new wideband unidirectional antenna element," *Int. J. Microw. Opt. Technol.*, vol. 1, no. 1, pp. 35-44, Jun. 2006.

[37] K. M. Luk and H. Wong, "A complementary wideband antenna," U.S. Patent 11/373 518, Mar. 10, 2006

[38] B. M. Alarjani and J. S. Dahele, "Feed reactance of rectangular microstrip patch antenna with probe feed," *Electron. Lett.*, vol. 36, no. 5, pp. 388-390, Mar. 2000.

[39] R. Munson, "Conformal microstrip antennas and microstrip phased arrays," *IEEE Trans. Antennas Propag.*, vol. 22, no. 1, pp. 74-78, Jan. 1974.

[40] J. Huang, "A parallel-series-fed microstrip array with high efficiency and low cross-polarization," *Microw. Opt. Technol. Lett.*, vol. 5, no. 5, pp. 230-233, May 1992.

[41] X. H. Yang and L. Shafai, "Characteristics of aperture coupled microstrip antennas with various radiating patches and coupling apertures," *IEEE Trans. Antennas Propag.*, vol. 46, no. 1, pp. 72-78, Jan. 1995.

[42] A. Adrian and D. H. Schaubert, "Dual-aperture-coupled microstrip antenna for dual or circular polarization," *Electron. Lett.*, vol. 23, no. 23, pp. 1226-1228, Nov. 1987.

[43] T. W. Chiou and K. L. Wong, "Broad-band dual-polarized single microstrip patch antenna with high isolation and low cross polarization," *IEEE Trans. Antennas Propag.*, vol. 50, no. 3, Mar. 2002.

[44] K. S. Ryu and A. Kishk, "Wideband dual-polarized microstrip patch excited by hook shaped probes," *IEEE Trans. Antennas Propag.*, vol. 56, no. 12, Dec. 2008.

[45] L. Siu, H. Wong and K. M. Luk, "A dual-polarized magneto-electric dipole with dielectric loading," *IEEE Trans. Antennas Propag.*, vol. 57, no. 3, Mar. 2009.

[46] W. Hang, "A novel wideband unidirectional antenna," Ph.D. dissertation, Dept. Elect., City Univ. Hong Kong, Kowloon, Hong Kong, China, 2006.

[47] Y. X. Guo, K. M. Luk and K. F. Lee, "L-probe fed thick-substrate patch antenna mounted on a finite ground plane," *IEEE Trans. Antennas Propag.*, vol. 51, pp. 1995-1963, Aug. 2003.

[48] T. P. Wong and K. M. Luk, "A wide bandwidth and wide beamwidth CDMA/GSM base station antenna array with low backlobe radiation," *IEEE Trans. Veh. Technol.*, vol. 54, no. 3, pp. 903-909, May 2005.

[49] D. Sievenpiper, L. Zhang, R. F. J. Broas, N. G. Alexopolous and E. Yablonovitch, "High-impedance electromagnetic surfaces with a forbidden frequency band," *IEEE Trans. Microw. Theory Tech.*, vol. 47, no. 11, pp. 2059-2074, Nov. 1999.

[50] D. Sievenpiper, "High-impedance electromagnetic surfaces," Ph.D. dissertation, Dept. Elect. Eng., Univ. California at Los Angeles, Los Angeles, CA, 1999.

[51] S. L. S. Yang and A. A. Kishk, "The forbidden bandgap characteristic of EBG structures," *Microw. Opt. Technol. Lett.*, vol. 50, no. 11, pp. 2965-2967, Nov. 2008.

VITA

Hyuk-Jun Seo was born in Daegu, Republic of Korea. He received his Bachelor of Engineering degree in Electrical Engineering and Computer Science from Kyungpook National University, Daegu, Republic of Korea in February, 2006. While working at his Master's degree at the University of Mississippi, he was employed as a graduate research assistant and teaching assistant at the department of Electrical Engineering from January 2006 to December 2009. Hyuk-Jun received the USNC/URSI Student Travel Fellowship Grant Award from the National Academics in 2010. He is a member of the IEEE (Antenna and Propagation Society and Microwave Theory and Techniques Society), a web administrator of the Korean Student Association at the University of Mississippi and a president of the Oxford Korean Tennis Club.

APPENDIX I

The characteristics of mushroom-like EBG structures can be explained using an effective medium model of the high-impedance surface. The surface wave bandgap corresponds roughly to the reflection phase of the EBG surface, between $+\pi/2$ and $-\pi/2$. Along with the analysis of the dispersion diagram for the unit-cell of the EBG surface in chapter IV, the reflection phase diagram is used as estimation for the bandgap of the designed structure. The derivation of the analytical model for the EBG structure using the dispersion diagram was illustrated in [52]. Therefore, this model can give approximate dimensions for designing the EBG structure at a desired frequency. The reflection phase, $\theta(f)$, of the EBG surface can be expressed as

$$\theta(f) = \mathrm{Im}\left[\ln\left(\frac{af^2 + jbf - \eta}{-af^2 + jbf + \eta}\right)\right] \tag{A.1}$$

where

f is the frequency,

η is an intrinsic impedance of free space, 120π

$$a = 4\pi^2 \eta LC \tag{A.2}$$

$$b = 2\pi L \tag{A.3}$$

and

$$L = \mu_o h \tag{A.4}$$

$$C = \frac{w(\varepsilon_r + 1)\varepsilon_0}{\pi} \cosh^{-1}\left[\frac{p}{g}\right] \tag{A.5}$$

When *p, w, g* are design parameters of the unit-cell of the mushroom-like EBG structure as

described in Fig. 4.9, then the frequency where the reflection phase is zero, f_{zero}, is

$$f_{zero} = \frac{1}{2\pi\sqrt{LC}} \tag{A.6}$$

Fig. A.1 shows the reflection diagram using the equations (A.1) to (A.6) with a substrate with dielectric constant of 10.2 and the above design parameters, p = 10.2 mm, w = 9.0 mm, g = 0.2 mm, and h = 2.54 mm.

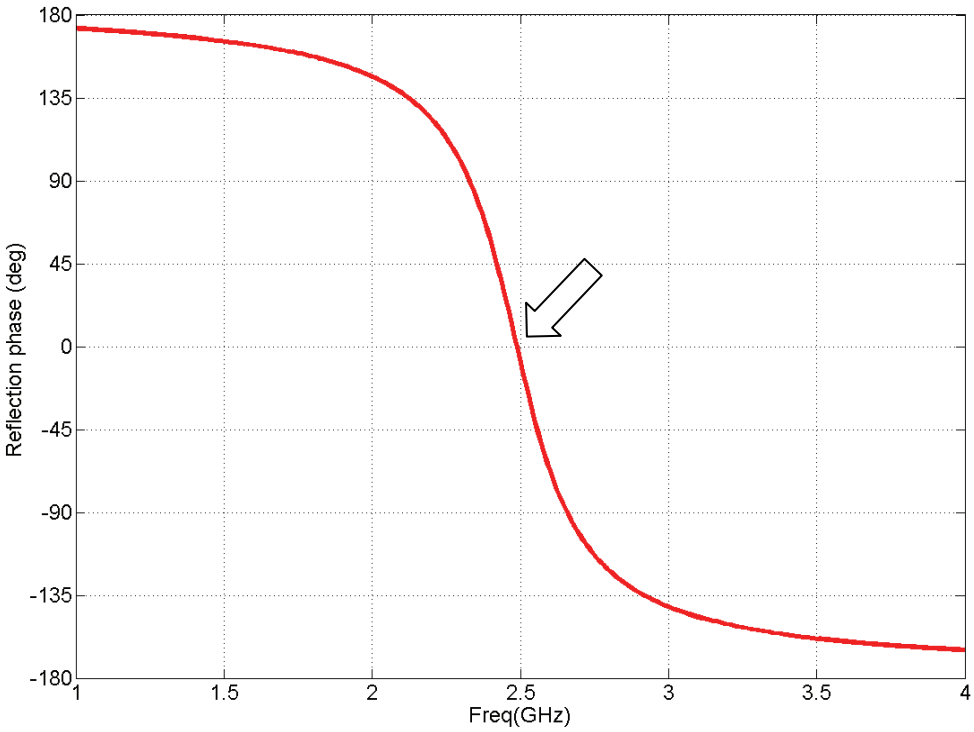

Fig. A.1 Reflection phase of the mushroom-like EBG structure